

OWIES WANI

Bioinspired Light Robots from Liquid Crystal Networks

OWIES WANI

Bioinspired Light Robots from Liquid Crystal Networks

ACADEMIC DISSERTATION

To be presented, with the permission of
the Faculty of Engineering and Natural Sciences of
Tampere University,

for public discussion in the Auditorium FA032
of the Festia building, Korkeakoulunkatu 8, Tampere,
on 17 May 2019, at 12 o'clock.

ACADEMIC DISSERTATION

Tampere University, Faculty of Engineering and Natural Sciences
Finland

<i>Responsible supervisor and Custos</i>	Professor Arri Priimägi Tampere University Finland	
<i>Co-supervisor</i>	Dr. Hao Zeng Tampere University Finland	
<i>Pre-examiners</i>	Professor Nathalie Katsonis University of Twente The Netherlands	Professor Panče Naumov New York University Abu Dhabi United Arab Emirates
<i>Opponent</i>	Professor Timothy J. White University of Colorado Boulder United States of America	

The originality of this thesis has been checked using the Turnitin Originality Check service.

Copyright ©2019 author

Cover design: Roihu Inc.

ISBN 978-952-03-1095-0 (print)
ISBN 978-952-03-1096-7 (pdf)
ISSN 2489-9860 (print)
ISSN 2490-0028 (pdf)
<http://urn.fi/URN:ISBN:978-952-03-1096-7>

PunaMusta Oy – Yliopistopaino
Tampere 2019

Dedicated to my parents.

ACKNOWLEDGEMENTS

The research presented in this thesis was mainly carried out in Hervanta Campus of Tampere University (*erstwhile Tampere University of Technology*) during the years 2016-2019. In addition to this, part of the work was also done at Eindhoven University of Technology during a 6-month (Feb-July 2018) research internship. I gratefully acknowledge the Graduate School of Tampere University for funding this research and International HR unit of Tampere University for their generous mobility grant.

Firstly, I express my sincere appreciation and gratitude to my supervisor Prof. Arri Priimägi for making it possible for me to join his research group as a PhD student and for providing me constant support, useful advices, ample resources and freedom in decision-making. He has been a great leader, good friend and inspiration for future scientific career. I would also like to thank my co-supervisor Dr. Hao Zeng. Without his guidance and collaboration, the outcome of this thesis would not have been possible. I am also thankful to colleagues and staff at Chemistry and Advanced Materials group (CAM) for providing a pleasant and friendly working atmosphere and for assisting with practical matters. My special thanks to all past and present members of the Smart Photonic Materials (SPM) team for the quality time we spent together. I would particularly like to thank Dr. Jelle Stumpel and Dr. Mikko Poutanen for guiding me during initial phase of my PhD, Dr. Zafar Ahmad and Mr. Jagadish Salunke for making me feel at home, Dr. Matti Virkki for helping with optical setups and Mr. Markus Lahikainen for providing me company in the office and in the lab.

Many thanks to all my co-authors, Prof. Albert Schenning, Dr. Piotr Wasylczyk, Dr. Radosław Kaczmarek and Mr. Rob Verpaalen, for their valuable contribution to our joint research projects.

I offer my gratitude to Prof. Albert Schenning and Prof. Dirk Broer for hosting me for a research internship in their group (SFD), at Eindhoven University of Technology and for providing me opportunity to participate in their inspiring discussions. Working in Eindhoven was a memorable and great learning experience for me. Thanks to all SFD members, especially, Mr. Rob Verpaalen, Ms. Ellen Heeswijk, Dr. Shaji Varghese, Ms. Marjolijn Voragen, Mr. Tom Bus, Ms. Marina Pilz Da Cunha, Dr. Matthew Hendriks, Ms. Yuanyuan Zhan and Dr. Monali

Moirangthem, for making my stay in Eindhoven pleasant and for assisting me with experiments and with practical matters.

I would like to thank the pre-examiners of this thesis, Prof. Nathalie Katsonis and Prof. Panče Naumov for their positive assessment of this thesis and for their good wishes regarding my future career.

I offer my deepest gratitude to my father, Mukhtar Ahmad Wani and mother, Matena Parveen - to whom this thesis is dedicated - for their guidance, support and prayers, to which I shall forever remain indebted to them. Sincere thanks to my sisters Aasiya Wani and Shanif Wani and my brother Faizan Wani for their support and wishes during my studies abroad. Thanks are due to my friends and mentors Mr. Fayaz Ahmad Dar for motivating me towards perusing my higher studies abroad, Mr. Mohsin Jahan Qazi for ensuring that I end up in 'Land of Midnight Sun' - for which I am very grateful to him - and Dr. Muhammad Safdar for his guidance since the beginning of my research career in Finland. I must also thank all the teachers, from whom I have benefited a lot throughout my life.

I would especially like to mention my friends, Syed Muzafar, Syed Mudabir, Abdul Hakeem, Arif Dar, Adil Rather, Ryhan Abdullah and Naveed Dar, for the precious and memorable time we spent together and for supporting, encouraging and helping me whenever I needed. I shall always cherish the time spent with you. I also want to thank all those whose names I couldn't mention but they have a direct or indirect influence on my thesis.

Finally, I express my love and gratitude to my wife, Uzma Wani, and my son, Hassaan Wani, for making my life special, for being always there for me through the thick and thin of our lives and for helping me to get rid of all worries and exhaustion. I shall always remain indebted towards the sacrifices you made for me during past few years.

Tampere, April 2019

Owies Wani

ABSTRACT

Bioinspired material research aims at learning from the sophisticated design principles of nature, in order to develop novel artificial materials with advanced functionalities. Some of the sophisticated capabilities of biological materials, such as their ability to self-heal or adapt to environmental changes, are challenging to realize in artificial systems. Nevertheless, many efforts have been recently devoted to develop artificial materials with adaptive functions, especially materials which can generate movement in response to external stimuli. One such effort is the field of soft robots, which aims towards fabrication of autonomous adaptive systems with flexibility, beyond the current capability of conventional robotics. However, in most cases, soft robots still need to be connected to hard electronics for powering and rely on complicated algorithms to control their deformation modes. Soft robots that can be powered remotely and are capable of self-regulating function, are of great interest across the scientific community.

In order to realize such responsive and adaptive systems, researches across the globe are making constant efforts to develop new, ever-more sophisticated stimuli-responsive materials. Among the different stimuli-responsive materials, liquid crystal networks (LCNs) are the most suited ones to design smart actuating systems as they can be controlled and powered remotely with light and thereby obviate the need for external control circuitry. They enable pre-programmable shape changes, hence equipping a single material with multiple actuation modes. In addition to light, they can also be actuated by variety of stimuli such as heat, humidity, pH, electric and magnetic fields etc., or a combination of these. Based on these advantages of LCNs, we seek inspiration from natural actuator systems present in plants and animals to devise different light controllable soft robotic systems.

In this thesis, inspired from biological systems such as octopus arm movements, iris movements in eyes, object detection and capturing ability of Venus flytraps and opening and closing of certain nocturnal flowers, we demonstrate several light robots that can be programmed to show pre-determined shape changes. By employing a proper device design, these light robots can even show the characteristics of self-regulation and object recognition, which brings new advances to the field of LCN-based light robots. For instance, octopod light robot can show bidirectional bending

owing to alignment programming using a commercial laser projector; artificial iris is a fully light controllable device that can self-regulate its aperture size based on intensity of incident light; the optical flytrap can not only autonomously close on an object coming into its “mouth” but it can also distinguish between different kinds of objects based on optical feedback, and finally, integration of light and humidity responsiveness in a single LCN actuator enables a nocturnal flower-mimicking actuator, which provides an opportunity to understand the delicate interplay between different simultaneously occurring stimuli in a monolithic actuator.

We believe that besides providing a deeper understanding on the photoactuation in liquid crystal networks, at fundamental level, our work opens new avenues by providing several pathways towards next-generation intelligent soft microrobots.

CONTENTS

1	Introduction	1
1.1	Aim and scope of this work	2
1.2	Thesis structure	4
2	Liquid crystals	5
2.1	Historical background	5
2.2	Basic properties of liquid crystals	7
2.3	Analytical tools for LC characterization	14
3	Liquid crystal networks	19
3.1	Preparation of LCNs	19
3.2	Thermomechanical actuation and programmed shape change	23
3.3	Photomechanical actuation using azobenzenes	28
4	Bioinspired liquid crystal based light robots	35
4.1	Inspiration from biological actuators	36
4.2	Review of previous studies	37
4.3	Pre-determined shape morphing	41
4.4	From self-regulation to object recognition	43
4.5	Towards humidity-gated actuation	47
5	Conclusions and Outlook	51
	Bibliography	55
	Publications	69

ABBREVIATIONS

LC	Liquid Crystals
LCN	Liquid Crystal Network
GLCN	Glassy Liquid Crystal Network
LCE	Liquid Crystal Elastomer
LCD	Liquid Crystal Display
A	Absorbance
POM	Polarized Optical Microscope
DSC	Differential Scanning Calorimetry
XRD	X-ray Diffraction
N	Nematic
Sm	Smectic
Ch	Cholesteric
I	Isotropic
Cr	Crystalline
DR1	Disperse Red 1
Azo	Azobenzene
GPa	Gigapascal
MPa	Megapascal
RH	Relative Humidity
SWCNT	Single-Walled Carbon Nanotube

ORIGINAL PUBLICATIONS

- Publication I Wani, O.M.; Zeng, H.; Wasylczyk, P.; Priimagi, A. Programming Photoresponse in Liquid Crystal Polymer Actuators with Laser Projector. *Adv. Opt. Mater.* **2018**, 6, 1700949.
- Publication II Zeng, H.; Wani, O.M.; Wasylczyk, P.; Kaczmarek, R.; Priimagi, A. Self-Regulating Iris Based on Light-Actuated Liquid Crystal Elastomer. *Adv. Mater.* **2017**, 29, 1701814.
- Publication III Wani, O.M.; Zeng, H.; Priimagi, A. A light-driven artificial flytrap. *Nat. Commun.* **2017**, 8, 15546.
- Publication IV Wani, O.M.; Verpaalen, R.; Zeng, H.; Priimagi, A.; Schenning, A.P.H.J. An Artificial Nocturnal Flower via Humidity-Gated Photoactuation in Liquid Crystal Networks. *Adv. Mater.* **2019**, 31, 1805985.

AUTHOR'S CONTRIBUTION

The work included in this thesis consists of four original articles, all published in peer-reviewed journals. The work for **Publications I-III** was done at Hervanta Campus of Tampere University (*erstwhile Tampere University of Technology*), while the work related to **Publication IV** was done at Eindhoven University of Technology, during a 6-month research internship by the author.

Publication I This publication deals with programming of shape changes in LCNs. Here, a commercial laser projector is used to program the director orientation in LCNs and several patterned deformations are visualized. The author took part in planning, performed all the experiments, fabricated the samples, analyzed the data, and wrote the first draft of the manuscript. The manuscript was finalized together with the coauthors.

Publication II This publication demonstrates an example of an artificial iris-like structure, controlled entirely by light. Similar to natural iris, the device can regulate its aperture size according to the intensity of incident light. The author took part in execution of experiments, fabrication of samples, material characterization, analysis of the actuation, and contributed to writing the manuscript.

Publication III This publication presents the fabrication and characterization of an LCN device inspired by ‘Venus Flytrap’, referred in the article as ‘artificial flytrap’. The device is autonomous, i.e., capable of sensing the environment and making simplistic ‘decisions’ based on optical feedback. It also integrates the power source (light from an optical fiber) into the same device structure. The author took part in planning and execution of all the experiments, fabricated and characterized all the samples, analyzed the data and contributed to writing the manuscript.

Publication IV This publication describes dual-responsive, light- and humidity-sensitive LCN that is used to fabricate an actuator inspired by nocturnal flowers. It highlights the interplay between different stimuli, which exists upon simultaneous exposure of the multiresponsive actuator to more than one stimulus. The author

took part in planning, executed all the experiments, fabricated and characterized the samples, analyzed the data, and wrote the first draft of the manuscript. The manuscript was finalized together with the coauthors.

1 INTRODUCTION

From simple plant hooks inspiring Velcro® to bones inspiring self-healing materials, scientists have always been intrigued by the unique features of biological materials.[1–3] As of the writing of this thesis, according to WEB OF SCIENCE more than 5000 scientific articles related to bioinspired artificial functions have been published in the last decade, gathering more than 100000 citations until now. Biological materials possess unusual properties which are generally not found in conventional artificial systems, fueling an extensive study of such materials over the past few decades.[4–9] These studies aim at elaborating the design principles behind their sophisticated and unique properties. Once the design principles are understood, it becomes viable to mimic some of the functional aspects from biology and consequently more advanced materials can be developed.[10]

At this point, it is pertinent to mention some of the important features that make natural materials so inspirational.[4] Firstly, biological materials possess hierarchical architecture from nano- to macroscale. Examples can be found in materials like bones, nacre, silk, wood etc., where the structures often consist of hierarchical soft organic and stiff inorganic components in a complex form.[11] Such hierarchical structures result in very stiff materials with much enhanced fracture toughness. Strength and toughness are generally mutually exclusive properties, but nature has managed to combine both of them through its elegant design principles, at the same time inspiring materials researchers over generations. Secondly, biological materials are functional, and often times appear with multiple functionalities. Recently, lots of attention has been given towards developing nature-inspired functional materials, which include but are not restricted to superhydrophobic and self-cleaning surfaces inspired by lotus leaf,[12] adhesive materials inspired by Gecko feet,[13] artificial structurally colored materials inspired by butterfly wings or natural opals,[14] anti-fouling coatings inspired by topography of mollusk shells or other marine species,[15] and so on. Finally, one of the most significant characteristics of biological materials, and also most challenging to mimic, is the adaptability and responsiveness. Biological materials are often not passive, but smart, dynamic and can adapt to the changes in their environment.[16] For example, biological materials

are able to self-heal,[17] can change their color,[18] switch between adhesive and non-adhesive states[19] and above all, exhibit stimuli-responsive movements.[20,21] Examples of stimuli-responsive movements are common in both animal and plant kingdoms. Fabrication of devices capable of stimuli-responsive movements, with nature-inspired “intelligence”, forms the core of this thesis.

1.1 Aim and scope of this work

This thesis seeks inspiration from nature in designing smart functional actuators that can produce motion in response to changes in their environment. Their development is essential for advancement of small-scale autonomous and adaptive soft robots.[22] To realize such systems, materials that can change shape in response to external stimuli, are the materials of choice. Among variety of stimuli-responsive shape-changing materials such as shape memory polymers, hydrogels, bilayer actuators etc., we chose liquid crystal networks (LCNs) due to the advantages they offer over the “competitors”. [23] LCNs have the ability to undergo fast and reversible shape changes triggered by a broad choice of stimuli (heat, humidity, pH, electric and magnetic field, light), and the deformation modes can be pre-programmed into material itself, thus forming a perfect platform for biomimetic research.

In the studies included in this thesis, light is the main stimulus to trigger the shape-change of the fabricated soft devices. Light is an attractive stimulus due to its abundance in nature, the ability to control it in space and time, its non-toxicity, and the possibility to remotely trigger the actuation. Many LCN-based light-deformable devices have been reported in literature.[24,25] This thesis study contributes to advancing the field by introducing novel concepts such as self-regulation and autonomous object recognition. To this end, four kinds of LCN-based light robots have been reported in the publications comprising this thesis, as graphically summarized in Figure 1.1. Using a commercial laser projector, alignment patterning in LCNs is realized and complex shape changes such as bidirectional bending of an octopod robot is demonstrated (**Publication I**). By combining the photoalignment method to optimized polymerization temperature, a self-regulating, iris-like device is demonstrated (**Publication II**). Inspired by the Venus flytrap, we integrated an LCN with an optical fiber, to yield the first example of an autonomous LCN-based gripping device with object-recognizing ability (**Publication III**). Finally, we introduced a novel dual-responsive actuation mechanism based on interplay between light and humidity, coined as humidity-gated photoactuation (**Publication IV**).

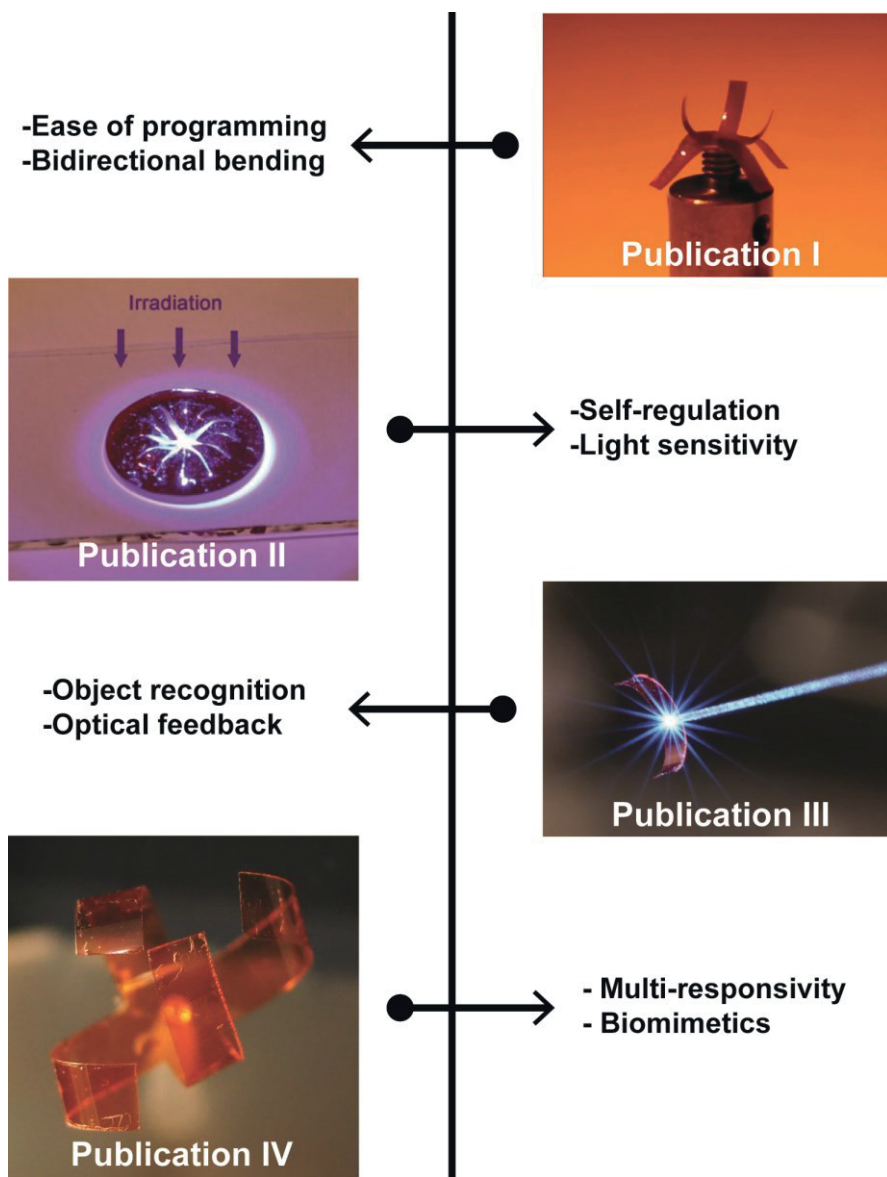


Figure 1.1 Compilation of the bioinspired liquid-crystal-based light robots demonstrated in the publications comprising this thesis work, along with important keywords to describe their overall scope.

The self-regulation and object recognizing capabilities of LCN actuators demonstrated in this thesis can potentially be integrated in smart soft-robotic devices as intelligent muscle-type actuators and at the same time also act as sensory elements. Multi-responsive LCN actuation, in turn, contributes to developing a deeper

understanding of the actuation process and also provides new insights into development of smart devices that could transduce rhythmic variation in light and humidity into mechanical work.

1.2 Thesis structure

This thesis is divided into 5 chapters. Chapter 2 introduces some of the basic concepts of liquid crystals (LCs) which are relevant to this thesis. It is divided into three sections. Section 2.1 gives a concise historical account of liquid crystals. Section 2.2 focuses on structural features of rod-like LCs and some basic properties of LCs. Section 2.3 discusses some techniques used to characterize the alignment order and phase transitions of LC molecules.

Chapter 3 introduces the field of LCNs. It also comprises of three sections. Section 3.1 begins with the discussion of common approaches used to prepare LCNs and then explains more thoroughly the method used in this thesis, based on photopolymerization. Section 3.2 describes the origin of the thermomechanical actuation of LCNs and their ability to undergo programmed shape changes. Finally, in section 3.3 photoactuation of azobenzene-containing LCNs is discussed.

Chapter 4 is the core of this thesis. It is divided into five sections. Section 4.1 highlights some of the examples from nature that can serve as an inspiration for development of smart robots. Section 4.2 reviews some of the previous work in the field of bioinspired LCN-based light robots. Finally, from section 4.3 to 4.5 the main results from the publications included in this thesis are highlighted.

Chapter 5 summarizes and concludes the overall work done in this thesis. In addition to this, future perspectives and new potential openings are proposed.

2 LIQUID CRYSTALS

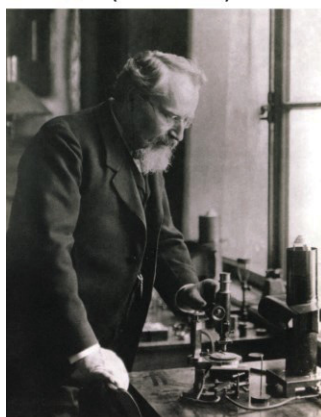
In today's world, the term 'liquid crystal' is familiar to everyone due to the invention of liquid crystal displays (LCDs), found almost in every household. LCs are special types of molecular assemblies which, under certain conditions, exist in a state of matter that lies between ordered crystalline solids and isotropic liquids. Hence, liquid crystals act as a mesophase, which can flow like liquids, while maintaining orientational and/or positional order (anisotropy) among the molecular constituents. In this chapter, we start by discussing some historical background of LCs, followed by fundamental properties of LCs that are relevant to this thesis. Finally, common analytical tools for LC characterization are introduced.

2.1 Historical background

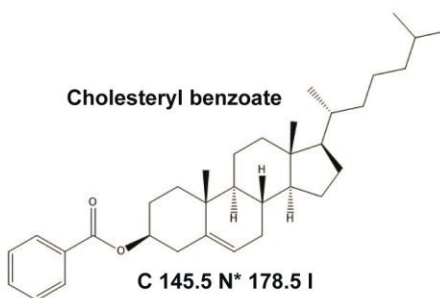
Discovery of LCs dates back to 1888, when a botanist named Friederich Reinitzer who was working in the Institute of Plant Physiology, University of Prague, observed the occurrence of two melting points in cholesteryl benzoate and an unprecedented coloured phenomenon in the melt. He observed that cholesteryl benzoate melts at 145.5 °C into a cloudy liquid, which was cleared only after heating further to 178.5 °C.[26] Reinitzer then approached a German physicist Otto Lehmann for advice related to optical properties, and Lehmann used polarized optical microscope equipped with a hot stage for characterization and eventually confirmed the existence of a previously unencountered soft crystalline phase in Reinitzer's samples. The result was published in 1889 (Figure 2.1).[27] After the discovery, LCs were not universally accepted as a new state of matter, as many scientists believed them to be simply combinations of solid and liquid phases.[28] LCs achieved universal acceptance only after appearance of a famous article written by Georges Friedel in 1922, who suggested the classification of liquid crystal phases into nematic, smectic and cholesteric, which has had a long-term and far-reaching influence in scientific community.[29]



Friedrich Reinitzer
(1857–1927)



Otto Lehmann
(1855–1922)



**Polarized optical microscope
with heating stage**

Über fließende Krystalle.

Von
O. Lehmann.

(Mit Tafel III und 8 Holzschnitten.)

First publication of Lehmann about LCs in 1889

Figure 2.1 Discovery of liquid crystals by Reinitzer and Lehmann in 1889. Adapted with permission: ref.[30]. Copyright 2015, Taylor & Francis Group.

From 1925 to 1959, interest in LCs decreased, mostly due to world wars and their aftermath. During this period, LC research was dominated by studying the influence of external fields like electric and magnetic fields on LCs (Freedericksz transitions), anisotropic properties of aligned LCs, structure/property relationships of LC molecules and development of fundamental theories of LCs.[28] Many new LC molecules were synthesized, with Daniel Vorländer - a German chemist, synthesizing most of them.[31] During 1920s, Oseen and Zocher started working on elastic theory of liquid crystals, with subsequent efforts from Frank after World War II.[32,33] This theory considered LCs as a continuum and ignored all the molecular

details. Later, this continuum theory was advanced by Ericksen, Leslie, de Gennes etc. and is now considered as one of the most fundamental theories of liquid crystals.[34] By the end of 1960s Alfred Saupe and his supervisor Wilhelm Maier studied nematic-to-isotropic phase transitions in LCs and developed the Maier-Saupe theory. This is another fundamental theory of LCs which takes into account the intermolecular anisotropic attraction and forces between dipoles of adjacent LC molecules.[35]

Period after 1960 is marked by the rapid developments of LCs, due to the fact that significant research effort was put in manufacturing electro-optical display devices. The boost in activity was launched by a publication of a review article by an American chemist Glenn Brown in 1957,[36] who subsequently brought different scientists together in the First International Liquid Crystal Conference (ILCC), held at Kent State University (Ohio) in 1965. Three years later, the first LCD device based on dynamic scattering was introduced by researchers from Radio Corporation of America, followed by two independent patents on twisted nematic LCDs by Helfrich and Schadt in Europe and Fergason in USA.[28,30] These patents intensified the research interest in LC community, and eventually in 1973 LCs based on 4-alkyl- and 4-alkoxy-4'-cyanobiphenyls with stable LC phases at room temperature were synthesized by Gray and coworkers.[37] This led to fast development of high-quality and reliable LCDs for the coming decades. In late 1980s, full-color LCDs appeared, and quickly took over the display market with ever-increasing quality and demand.

2.2 Basic properties of liquid crystals

LCs are classified into two types: thermotropics and lyotropics. Thermotropics exist in LC phase at specific temperature range, while lyotropics, in addition to temperature, requires a solution of specific concentration for the LC phase to occur. Since this thesis only deals with thermotropic LCs, lyotropics will not be discussed further, and interested readers are directed to ref. [38] for more details.

Generally, molecules exhibiting thermotropic LC phases are either rod-like (referred to as calamitic) or disc-like (discotic). All the LC molecules used in this thesis are calamitic in nature and their general structure is discussed here, based mainly on refs. [30,39,40]. Calamitic LCs form through steric repulsion and anisotropic dispersive interactions between the rod-like molecular constituents. In order to show LC phase, the molecule should possess an anisotropic conformation.

Typical calamitic LC molecules possess the characteristic structural units shown in Figure 2.2a. The two main units are the mesogenic core and the side-group(s). The mesogenic unit may be subdivided into rings (R) connected with bridge(s) (B) and similarly, side groups consist of terminal groups (T_L and T_R), lateral groups (L) and links (Y). The mesogenic unit forms the rigid core of the molecules and comprises aromatic or aliphatic rings being connected directly or via a bridging group. Typical rings and bridges used in the mesogenic units are presented in Figure 2.2b-c, respectively. The mesogenic unit is of fundamental importance as it provides rigidity and linearity to the LC molecules, key to the formation of the mesophase. The bridging group helps in increasing the length-to-breadth ratio and polarizability anisotropy in order to increase the thermal stability of the LC phase. In addition, some bridging groups, e.g. azo linkage, are used for the synthesis of photoresponsive LCs.

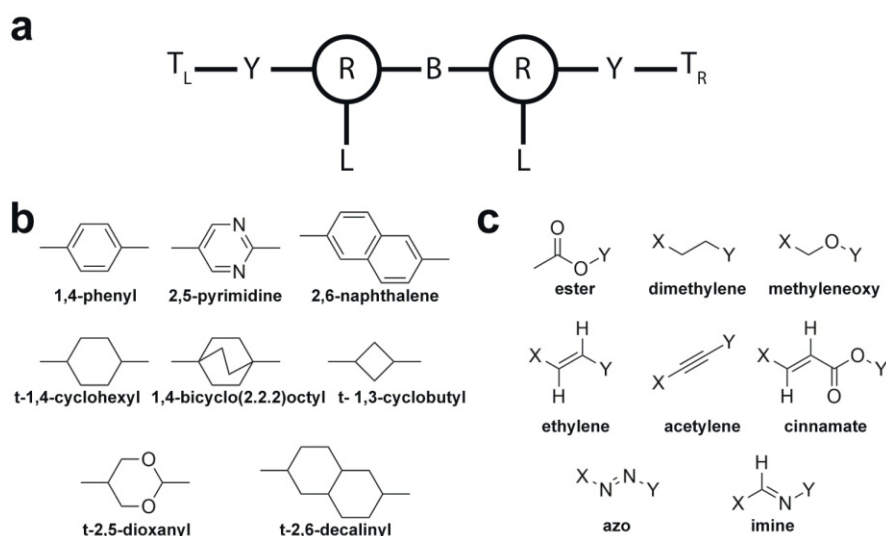


Figure 2.2 a) Characteristic structure of calamitic liquid crystals, b) common rings (R) and c) bridging groups (B) used to synthesize LC molecules.

Terminal groups, e.g. long alkyl (C_nH_{2n+1}) or alkoxy ($C_nH_{2n+1}O$) chains, increase the flexibility of the molecule, which tends to reduce the melting point. In addition, they stabilize the molecular orientation within the LC phase. Polar groups like CN, F, Cl etc., may not drastically affect the melting point, however, they increase the intermolecular attractive forces, thereby stabilizing the molecular orientation. Lateral substituents such as F, Cl, CN, NO_2 , or CH_3 can be attached off-axis to the mesogenic unit and due to disruption in molecular packing they decrease the stability

of the LC phase. Fluorine is the most commonly used lateral substituent in nematic mixtures as it enhances the physical properties, such as dielectric anisotropy, of display devices. The terminal groups are connected to the mesogenic core either directly or via some linking groups.[40]

Thermotropic LC phase exists within a certain temperature range, below and above which, molecules appear in crystalline (Cr) and isotropic (I) state, respectively. Transition from Cr to LC phase occurs at melting temperature and LC to I transition occurs at temperature referred as clearing point. Within the LC state, they show polymorphism and can exist in different sub-phases, e.g., nematic (N), smectic (Sm) and/or cholesteric (Ch), depending on the orientational and positional order of the molecules (Figure 2.3).[41] Some LCs only exhibit nematic phase and some only smectic phase, while some have both, appearing at different temperature ranges. Nematic phase is the most common phase, characterized by orientational order in an average direction denoted by a vector called director, \mathbf{n} , but lacking positional order between the molecular constituents. Smectic phase is characterized by both orientational and positional order of molecules, and the molecules are arranged in layers with center of masses being aligned. Smectic phase is sub-divided into different types labelled, e.g., A, B, C, I etc., depending on the tilt angle between director and the smectic layer normal, and also on the molecular packing. Among smectics, SmA and SmC are most common phases. In SmA director is parallel to smectic layer normal, whereas in SmC phase there is a tilt angle between director and smectic layer normal, as illustrated in Figure 2.3. Orientational order of LCs is characterized by order parameter, S ,

$$S = \frac{1}{2}(3\cos^2\theta - 1), \quad (1)$$

where θ is the average angular deviation of the LC molecules from \mathbf{n} . Typical values for S are between 0.3 and 0.8, decreasing slowly with increase in temperature, with sharp decrease around the clearing temperature. $S = 1$ refers to perfect order as would be in defect-free crystals, whereas, $S = 0$ refers to random alignment as found in isotropic liquids.

Cholesteric phase is a special LC configuration similar to nematic phase but with chirality which causes helical rotation of the molecules along the axis perpendicular to \mathbf{n} . Cholesteric LCs are also referred as chiral nematics, N^* . Length of the helix over which the director completes 360° rotation is called pitch, P . The pitch defines the periodicity of the material, acting as a Bragg reflector for selective reflection of certain wavelengths of light.[42]

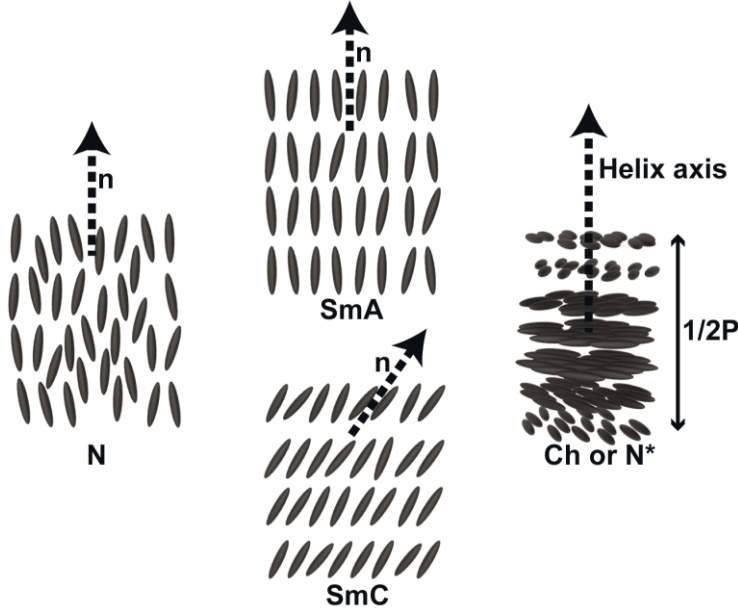


Figure 2.3 Schematic representation of common liquid crystal phases.

Nematic LCs are uniaxial anisotropic materials, possessing two inequivalent principle directions in their ordered state i.e. the director axis, \mathbf{n} , and the directions perpendicular to it. The uniaxiality leads to anisotropy in dielectric, magnetic and optical properties, i.e., different values of dielectric permittivity, magnetic susceptibility, and refractive index, in directions parallel and perpendicular to \mathbf{n} . For instance, the response to electric fields is dictated by anisotropy in permittivities, parallel (ϵ_{\parallel}) and perpendicular (ϵ_{\perp}) to \mathbf{n} . The difference between these permittivities, $\Delta\epsilon = \epsilon_{\parallel} - \epsilon_{\perp}$, referred to as dielectric anisotropy, can have positive or negative values. LCs with positive dielectric anisotropy orient themselves with their long molecular axis parallel to electric field, \mathbf{E} , whereas in case of negative value they orient perpendicular to \mathbf{E} . [30,40] Larger $\Delta\epsilon$ ensures LC devices to have shorter response time and lower voltage threshold. LC molecules are mostly diamagnetic in nature, possessing positive diamagnetic anisotropy, $\Delta\chi = \chi_{\parallel} - \chi_{\perp}$, where χ_{\parallel} and χ_{\perp} are magnetic susceptibilities parallel and perpendicular to \mathbf{n} . Hence, external magnetic field induces small magnetic dipoles in LC molecules, causing their reorientation parallel to it.

In terms of optical properties, most LC phases (N, SmA) are optically positive i.e. they exhibit higher index of refraction for light polarized parallel to optic axis (n_{\parallel}) as compared to the one polarized perpendicular to it (n_{\perp}). [43] In other words,

birefringence, $\Delta n = n_{||} - n_{\perp} > 0$, obtaining values typically in the range $0.2 - 0.3$. Light passing through the LC, therefore, gets split into two components having perpendicular polarizations and experiencing ordinary (n_o) and extraordinary (n_e) refractive indices. Due to the different refractive indices, the ordinary and extraordinary rays propagate at different velocities through the medium, imparting a phase shift, δ , which leads to change in the state of polarized light passing through LC medium. The induced phase shift at the wave-front is given by:

$$\delta = \frac{2\pi}{\lambda} (n_e - n_o) d. \quad (2)$$

Here, λ is the vacuum wavelength of light and d is the distance travelled by light within the medium (sample thickness). Ordinary, n_o , and extraordinary, n_e , refractive indices are related to principle refractive indices $n_{||}$ and n_{\perp} as per following equations:[44]

$$n_o = n_{\perp}, \quad (3)$$

$$n_e = \frac{n_{||} n_{\perp}}{\sqrt{n_{||}^2 \cos^2 \phi + n_{\perp}^2 \sin^2 \phi}}, \quad (4)$$

where ϕ refers to angle between the optic axis (the director \mathbf{n}) and the direction of light propagation. The change in the state of polarized light passing through LC medium forms the basis for working of polarized optical microscope (POM) widely used in characterization of LC phases, as discussed in section 2.3, and also for other optical components based on LCs.

Orientational order of nematic LCs is also responsible for their elastic properties. Due to their low viscosity, the order can be distorted with small external fields, but once these fields are removed, the LCs return to their initial state due to the storage of elastic free energy. This property is important for optical switching needed in, e.g., electro-optic display devices. For practical applications LCs are usually aligned uniformly in a cell comprising two treated glass substrates, with a gap of few to tens of microns. Alignment of LCs within the cell is dictated by surface anchoring/boundary conditions, conventionally achieved by mechanical or chemical treatment of the inner surface of the glass substrate.[45] Two most common boundary conditions are planar and homeotropic anchoring. In planar orientation, LC molecules lie parallel to the glass substrate either pointing randomly (Figure 2.4a) or

towards one direction (Figure 2.4b). In homeotropic orientation they prefer to align perpendicular to the glass substrate (Figure 2.4c). Planar boundary conditions are conventionally introduced by coating the substrate surface with special polymers such as thermoplastics like poly(vinyl alcohol) or polyamides, or thermosets like polyimides. Uniform alignment is achieved by rubbing with velvet cloth in a particular direction. Mechanism of aligning LCs by surface treatment is believed to be a combination of physiochemical processes such as dispersive and dipolar interactions, and topology-promoted alignment of the anisotropic LC molecules in microgrooves generated by rubbing.[46,47] Homeotropic orientation is conventionally achieved by coating the substrate with surfactants, without the need for rubbing. Homeotropic alignment arises from the steric interaction between the LC molecules and the surfactant molecules and its quality highly depends on the surface density of the surfactant molecules.[47]

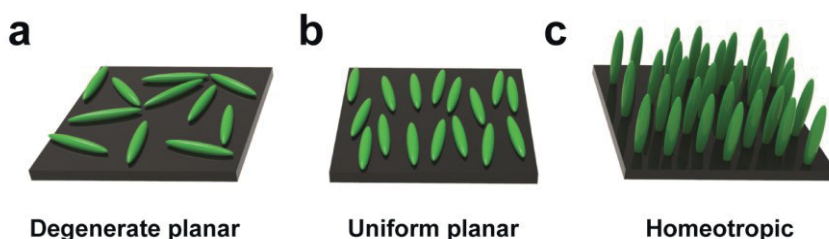


Figure 2.4 Schematic representations of a) degenerate planar, b) uniform planar and c) homeotropic alignment of LCs.

In addition to conventional methods of mechanical and chemical treatment of surfaces, other methods also exist for controlling the alignment of LCs. These methods include but are not restricted to photolithography,[48] oblique evaporation of SiO_x films,[49] electric or magnetic field-induced alignment,[50] and photoalignment.[51,52] In this thesis, in addition to the conventional methods, photoalignment has been used in **Publication I** and **Publication II**.

Photoalignment is based on illuminating a substrate coated with a thin photoresponsive alignment layer, a ‘command surface’,[52] with polarized light. Upon illumination, the photoalignment layer becomes anisotropic and dictates the boundary conditions for alignment of LC molecules. Depending on the type of photoalignment layer used, LCs align either parallel or perpendicular to the direction of light polarization.[51] Photoalignment materials used in this thesis are based on azobenzene molecules, which can undergo photoisomerization from *trans* to *cis* form

(see section 3.3 for more details). Ichimura *et. al.* first reported the use of azobenzene monolayer to switch the LC orientation from planar to homeotropic via *trans-cis* photoisomerization of azobenzenes.[53] Soon after, many research groups demonstrated the ability of this technique to align LC molecules in azimuthal plane of the substrate,[54,55] which could serve as an alternative to rubbing method. Unlike rubbing, photoalignment does not produce any dust or excess charge on the substrate, hence is advantageous.

Mechanism of photoalignment based on azobenzenes is typically explained on the basis of angular redistribution of molecules. Due to repetitive *trans-cis-trans* isomerization cycles upon light irradiation, molecules undergo a statistically random re-orientation. Polarized light thus reorients the molecules by accumulating them with their long axes perpendicular to light polarization, since the absorption of azobenzenes is minimum in that direction. By spatially modulating the polarization of light, complex photopatterning of LCs can be achieved.[56] In **Publication I**, laser projector coupled with rotatable linear polarizer is used for spatial modulation of light polarization to inscribe alignment programming in LCN (Figure 2.5a). Similarly, in **Publication II**, a laser setup equipped with polarization convertor is used to achieve the radial alignment patterning required in an artificial iris structure, which is important for centrosymmetric bending of the iris segments (Figure 2.5b).

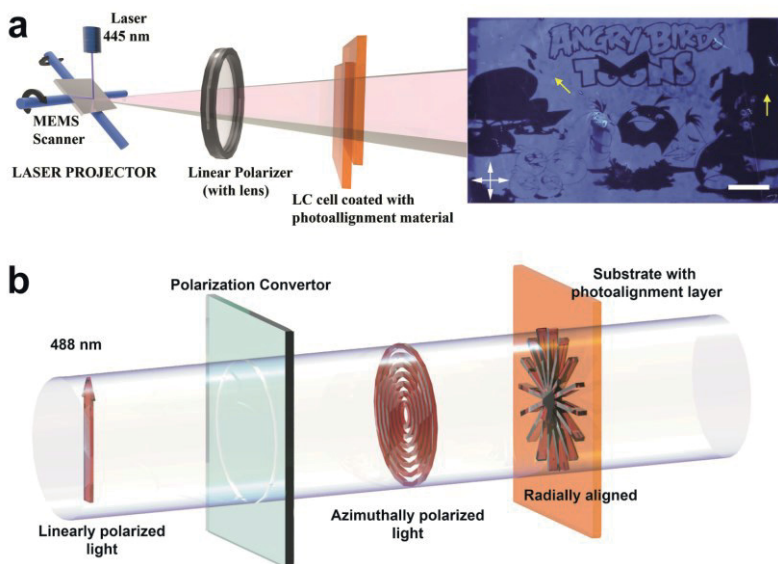


Figure 2.5 Photoalignment of LCNs is achieved through illumination a) with a commercial laser projector (**Publication 1**), and b) through a polarization convertor (**Publication 2**).

2.3 Analytical tools for LC characterization

Many analytical techniques are used for characterization of LCs such as differential scanning calorimetry (DSC), polarized optical microscopy (POM), polarized absorption spectroscopy and X-ray diffraction (XRD). These techniques probe, e.g., their phases/phase transitions and the order parameter S . In this section, wherever possible, the characterization methods will be exemplified with LC mixture used in **Publication IV** (Figure 2.6a), as this mixture shows both nematic and smectic phases.

DSC consists of two pans, one filled with sample and another empty (reference). Both these pans are heated, and the difference of heat flow needed to maintain equal temperatures in these pans is measured as a function of temperature. DSC plot gives two kinds of information. First it gives us information about phase transition temperatures i.e. a temperature window where LC behavior is observed. Secondly, the enthalpy of phase transition (\sim area under the phase transition peak) indicates how large is the change of molecular order upon transition from one phase to another. Hence, the enthalpy of transition is higher for crystal-to-LC transition and smaller for LC-LC or LC-isotropic (clearing point) transition.[30] DSC analysis of the LC mixture presented in Figure 2.6a is shown in Figure 2.6b.

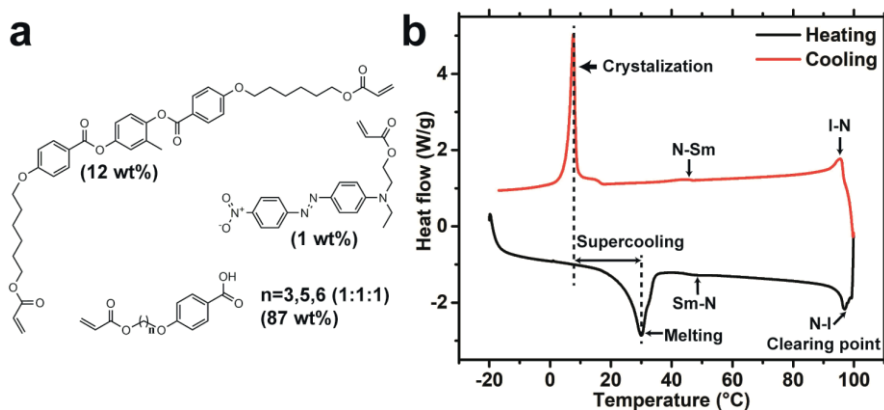


Figure 2.6 a) Composition of LC mixture used in **Publication IV** and **b)** its DSC plots labelled with different phase transitions.

Based on the cooling curve, a peak appearing around 95°C represents isotropic-to-nematic phase transition, a low-enthalpy peak around 45°C nematic-to-smectic transition, and the sharp peak around 10°C corresponds to crystallization, giving a

phase behaviour that can be written in following notation: Cr10SmX45N95I. Here X in SmX refers to subtype of smectic phase i.e. A, B, C etc. In heating cycle, the transitions are reversible, denoting enantiotropic LC behaviour. In some cases, the LC phase appears only upon cooling, referred to as monotropic. There is usually a displacement of transition temperature in heating cycle when compared to cooling cycle due to supercooling effect.[57]

POM is probably the most widely used technique for the determination of LC phases and their transition temperatures. It consists of crossed polarizers i.e. two polarizers that are rotated to 90° with respect to their polarization axes. One of the polarizers lies between the light source and the sample and the other one, also called analyzer, lies between the sample and the observer. Sample stage is also equipped with an integrated heating stage, to observe the sample at different temperatures. Normally, light does not transmit through crossed polarizers, however, when LCs are introduced between the crossed polarizers, they impart phase shift to the incoming linearly polarized light. Due to phase shift, generally, linearly polarized light is converted to elliptically polarized light and thus some components of light pass through the analyzer, causing LC sample to appear bright under POM. Intensity of the transmitted light is given by following equation:[44]

$$I = I_0 \sin^2 2\varphi \sin^2 \frac{\delta}{2}. \quad (5)$$

Hence the intensity of transmitted light in POM does not only depend on δ but also on the azimuthal angle, φ , i.e. angle between analyzer and the optic axis. In an unaligned state, nematic LCs appear as thread-like textures in POM, called Schlieren textures. This is due to the presence of defects in LCs, known as disclinations. Disclination refers to discontinuity in the inclination of molecules and is defined by defect strength, $\pm m$. [58] Defect is said to be of strength m , if, while moving around it in a closed path, director makes m multiples of 360° rotations. Defects are observed as dark brushes under POM, and the number of brushes N is related to the defect strength as $m = N/4$. [59] The brushes represent the areas where the director is either parallel ($\varphi = 0^\circ$) or perpendicular ($\varphi = 90^\circ$) to the polarizers i.e. $I = 0$. The sign of m can be determined with POM by keeping the sample fixed and rotating the crossed polarizers. If the brushes rotate to the same direction as the polarizers, the defect is denoted as $+m$, otherwise it is denoted as $-m$. Naturally occurring defects in nematic LCs are of the strength ± 1 or $\pm 1/2$ (Figure 2.7a). The appearance of beautiful colored textures in LC samples due to disclinations forms

the basis for POM analysis. When LC samples are analyzed under POM, characteristic textures are observed, which correspond to specific LC phases.[60,61] For example, nematic phase appears as thread-like Schlieren textures in planar anchoring (Figure 2.7b) while as smectic A phase appears as fan-like texture (Figure 2.7c). Similarly, chiral nematic phase in homeotropic alignment exhibits fingerprint textures (Figure 2.7d). It must be noted that appearance of textures in specific LC phase may vary with change in anchoring conditions, sample thickness, domain size etc., hence, variety of possible textures can be identified. POM images corresponding to different phases of LC mixture shown in Figure 2.6a, are depicted in Figure 2.7e, which complement the results from DSC analysis.

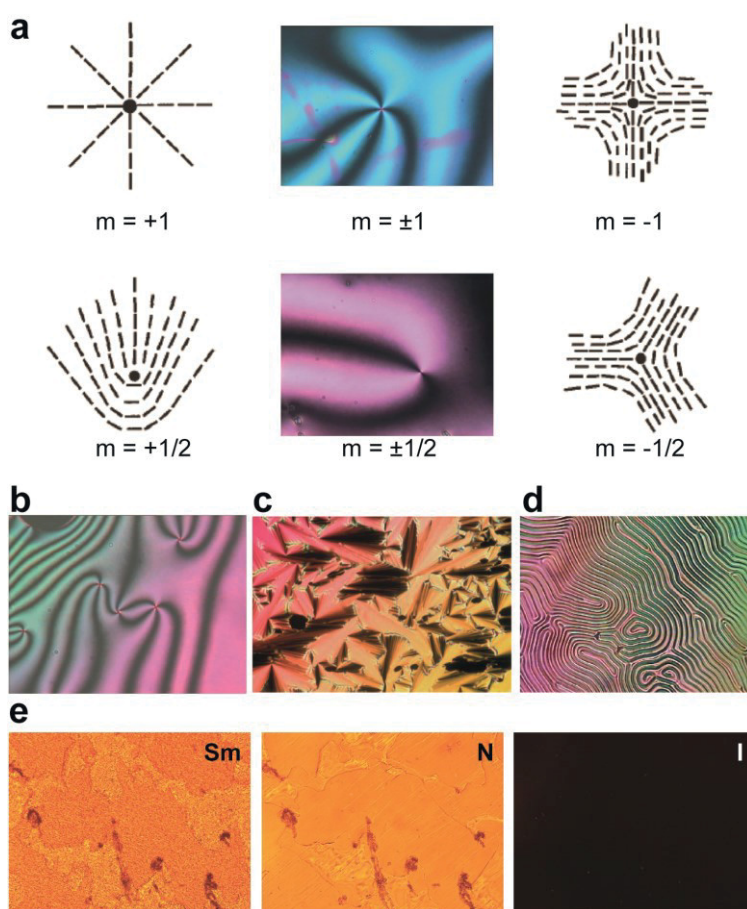


Figure 2.7 a) Naturally occurring disclinations in nematic liquid crystals and their appearance in POM, b) Thread-like texture of nematic phase with planar anchoring, c) Typical fan-shaped texture of Smectic A phase, d) fingerprint texture in cholesteric phase with homeotropic orientation and e) POM images of different phases of LC mixture used in **Publication IV**. Figures reproduced with permission: **a-d)** ref. [62]. Copyright 2004, John Wiley and Sons.

XRD is also used to differentiate between various LC phases, especially to measure the structural details about molecular packing. The technique is based on elastic scattering of X-rays by electrons in the LC sample. For nematic phase, diffuse peak is observed in both small-angle (low- q) and wide-angle (high- q) regions, which gives an estimate of molecular length (end to end) and width (intermolecular distance), respectively. Here, q is defined as a scattering vector and is related to scattering angle (2θ) by $q = (4\pi/\lambda)\sin(2\theta/2)$. [63] For smectic phases, generally one or more equally spaced sharp peaks appear in the small-angle region, while the wide-angle region is similar to that of the nematic phase. In case of unaligned LC samples, due to multiple domains, diffraction occurs in the form of rings, while, in aligned LC samples, it occurs mostly in the direction perpendicular to the alignment director, in the form of arcs (nematic) or patterns (smectic). As mentioned above, from the analysis with DSC and POM we know that LC mixture shown in Figure 2.5a possesses both nematic and smectic phase with the following phase behavior: Cr10SmX45N95I. XRD measurements of the same mixture at different temperatures are shown in Figure 2.8a, which reveals the same trend, however, sharpness of the small-angle peak at 80 °C and its pattern in the aligned state (Figure 2.8b) gives some additional information about the nematic and smectic phases. XRD pattern of aligned sample at 80 °C suggests that nematic phase is of cybotactic nature (Ncyb), since the scattering arc at small-angle appears to split into two maxima on either side of the meridian, which is common for nematic phase containing SmC-like cybotactic clusters. Hence, complete phase behavior can be put as C10SmC45Ncyb95I. [63] Cybotactic phase is defined as a nematic phase with presence of smectic-like clusters. [64] For more detailed understanding of XRD patterns of other sub-types of smectic phase, reader is directed to ref. [63].

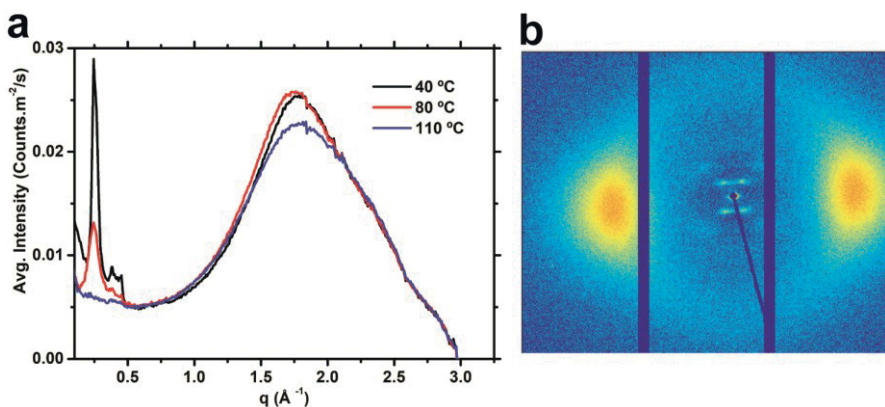


Figure 2.8 XRD analysis of LC mixture shown in Figure 2.5a in **a)** unaligned state at different temperatures and **b)** aligned state (after polymerization) at 80 °C.

Besides determination of LC phase, measurement of order parameter, S , of LCs is important as many physical properties such as dielectric anisotropy and birefringence depend on it. S can be measured by various techniques. Most conveniently, it can be monitored via polarized absorption spectroscopy, i.e., by measuring the dichroism of a chromophore possessing discrete transition moment with respect to its molecular axis (long axis). Both UV-Vis and IR absorption spectroscopies are applicable in this method. Dichroic order parameter of a planar homogenously aligned LC sample is calculated using the following formula:[65]

$$S = \frac{2(A_{\parallel} - A_{\perp})}{(A_{\parallel} + 2A_{\perp})(3\cos^2\gamma - 1)} \quad (6)$$

Here, A_{\parallel} and A_{\perp} are the polarized absorbances parallel and perpendicular to \mathbf{n} , respectively, and γ is the angle between the transition dipole moment and long axis of the dichroic chromophore. Since for the chromophores used in this thesis $\gamma \approx 0$, S can be simplified to

$$S = \frac{A_{\parallel} - A_{\perp}}{A_{\parallel} + 2A_{\perp}} \quad (7)$$

Figure 2.9 depicts the polarized UV-Vis absorption spectra of a liquid crystal network prepared from a LC mixture used in **Publication III**, which contains a same dichroic dye shown in Figure 2.6a. The order parameter was calculated using Eq. 7, yielding a value of ~ 0.6 .

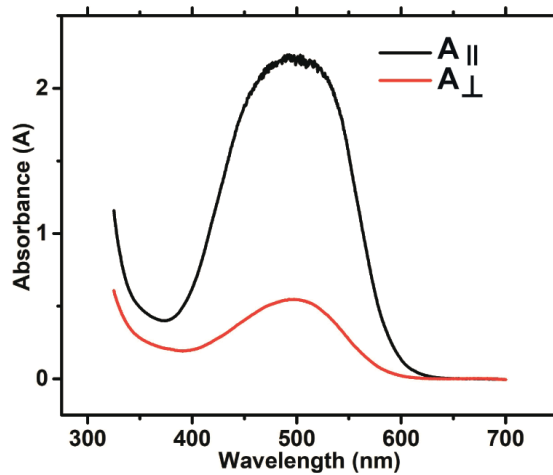


Figure 2.9 Polarized UV-vis absorption spectra of liquid crystal network doped with a dichroic dye.

3 LIQUID CRYSTAL NETWORKS

Liquid crystal networks (LCNs) refer to crosslinked synthetic polymers which combine the anisotropy of LCs with mechanical properties of polymers. Depending on the degree of crosslinking LCNs are of two types: weakly crosslinked liquid crystal elastomers, LCEs ($T_g < 20$ °C, Modulus ~ 0.1 -5 MPa) and moderate to densely crosslinked glassy liquid crystal networks, GLCNs ($T_g \sim 40$ -120 °C, Modulus ~ 0.8 -2 GPa).[66] In this thesis we use LCNs to refer to both types, unless otherwise stated. Similar to low-molecular-weight LCs, LCNs can also undergo stimuli induced decrease in the molecular order. Due to crosslinked nature of the polymeric network, such decrease in molecular order leads to a shape-change of the entire material, the degree of which depends on the crosslinking density in the network.[66,67] Weakly crosslinked LCEs possess flexible polymer backbones, thus exhibiting rubber-like elasticity and a large deformability in response to appropriate stimuli, whereas, GLCNs show much smaller stimuli-induced shape-change, due to the highly crosslinked molecular architecture. In this chapter, firstly the preparation of LCNs, with emphasis on method used in this thesis, is presented. Then, thermomechanical actuation of LCNs along with the role of molecular alignment in dictating their deformation modes is discussed. Finally, basics of photomechanical actuation in azobenzene-containing LCNs, including a brief comparison between photochemical and photothermal actuation mechanisms, is described.

3.1 Preparation of LCNs

Generally, LCNs can be prepared by using two approaches. The first approach, introduced by Finkelmann and co-workers,[68] involves a two-step crosslinking of polymer precursors, with alignment of mesogens being achieved mostly by mechanically stretching the network after or during the first crosslinking step. (Figure 3.1a) The second approach, developed at Philips Research Center,[69] involves crosslinking of low-molecular-weight reactive LC mesogens, usually in a single-step. (Figure 3.1b) The molecular alignment of thus formed LCN is controlled by surface treatment of the cells in which the polymerization is performed. Thus,

many conventional alignment techniques can be implemented, which make this method very attractive. Due to this advantage, the second approach has been used in this thesis for the preparation of LCNs, and the discussion is restricted only to this method. For more details on “the Finkelmann approach”, the readers are directed to reviews given in refs. [67,70].

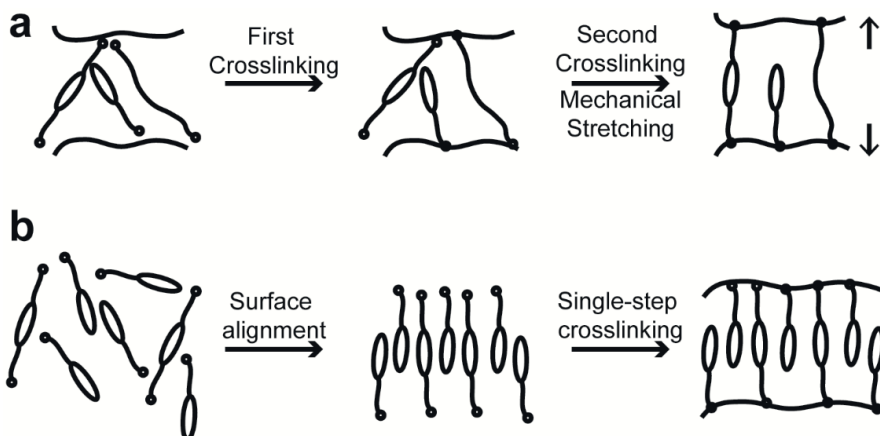


Figure 3.1 The two main approaches used for preparation of LCNs.

Due to the limitations of the Finkelmann approach, i.e., the viscous nature of polymer precursors, it is not compatible with surface alignment or photoalignment methods. One of the important advantages of surface alignment using LC monomers is the ability to program complex molecular alignment in LCNs, resulting in complex shape-morphing.[66,71] However, reliance of this method on surface treatment, restricts thus formed LCNs to thin sheets of maximum thickness around few hundreds of microns. Recently, with the use of additive manufacturing techniques such as 3D printing, this drawback has been greatly eliminated.[72,73]

Figure 3.2a shows some of the reactive mesogens, photoactive molecules, and photoinitiators used in this thesis to prepare freestanding LCNs using *in-situ* photopolymerization. The method involves mixing of the acrylate-functionalized LC monomers with photoinitiators and crosslinkers in the dark, followed by their melting into the isotropic state. Note that methacrylates can also be used to prepare LCNs, however due to their lower reactivity compared to acrylates, they were not used in this thesis study. This liquid is then filled into LC cells with desired surface treatment to yield, e.g., planar or homeotropic LC alignment on the surfaces, after which photopolymerization is performed in the LC state by slowly decreasing the temperature of the LC cell via a temperature-controlled platform (Figure 3.2b).

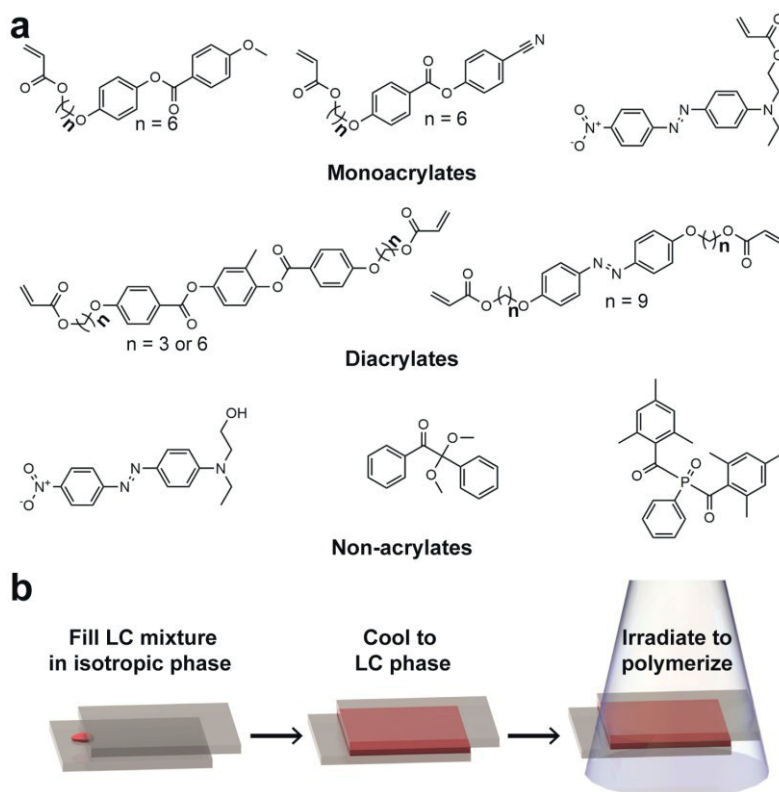


Figure 3.2 a) Common acrylate and non-acrylate molecules used in this thesis for preparation of LCNs. b) schematics showing preparation method of LCN films via photopolymerization of reactive mesogens in LC cell.

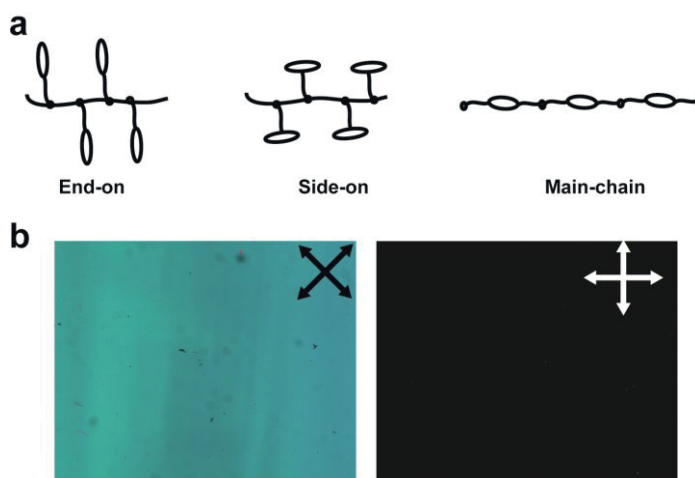


Figure 3.3 a) Different architectures of LCNs based on connectivity of mesogen to main polymer chain. b) POM images of LCN sample with uniform planar alignment. Arrows represent the direction of polarizer and analyzer.

The *in-situ* free-radical polymerization of acrylate mesogens was initially used to prepare GLCNs, utilizing diacrylate mesogens, however, modification of composition by introducing monoacrylate mesogens[74–76] or chain-extending reagents[77–79] helps to reduce the crosslink density, resulting in lower modulus and T_g . Moreover, different structural architectures exist in LCNs depending on the connectivity of mesogens with main polymer chain, resulting in end-on, side-on and main-chain LCNs (Figure 3.3a). The films prepared in LC cells can be easily aligned into monodomain, as can be seen in POM images of an LCN film with planar uniform alignment (Figure 3.3b). Ikeda and co-workers developed acrylate-functionalized azobenzene mesogens,[80] which opened the path towards photocontrollable LCNs using *in-situ* photopolymerization, as will be discussed in Section 3.3.

In **Publication IV**, by slightly modifying the molecular composition reported by Broer and co-workers,[81] a dual-responsive LCN actuator was prepared, which in addition to being light-responsive, is also sensitive to humidity. This actuator was fabricated from acrylate-based carboxylic acid monomers (Figure 3.4a), which dimerize via hydrogen bonding and thereby, exhibit LC behavior. After photopolymerization, the pristine LCN becomes sensitive to humidity only after it is treated with a basic solution, which breaks the hydrogen bonds between the dimers and converts them into hygroscopic carboxylic salt (Figure 3.4b). Light sensitivity is brought by the addition of an azobenzene molecule into LCN. Actuation of this dual-responsive LCN is further discussed in Section 4.5.

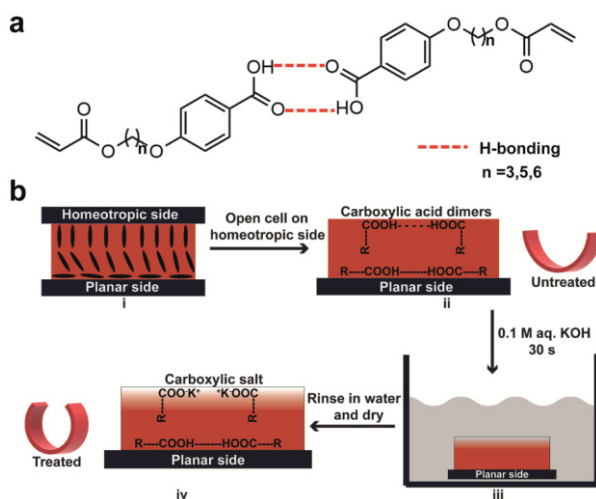


Figure 3.4 a) Acrylate-functionalized carboxylic acid monomers form dimers showing LC phase. **b)** Base treatment of LCN formed from carboxylic acid mesogens renders them humidity sensitive.

3.2 Thermomechanical actuation and programmed shape change

As mentioned before, LCNs combine the anisotropic properties of liquid crystals with the mechanical properties of polymer networks. In case of LCEs, like low molecular weight LCs, heat triggers the decrease in molecular order (S) (Figure 3.5a), which, due to anisotropic and crosslinked nature of network, results in change of polymer conformation from elongated to random-coil (spherical) state. This change in polymer conformation results in the macroscopic contraction of LCEs along the director and expansion perpendicular to it (Figure 3.5b).[66,67] Such deformation was theoretically predicted by de Gennes already in 1975,[82] and experimentally demonstrated by Finkelmann in 1991.[68] For example, length changes as large as factor 4 have been reported for some main-chain LCEs.[83] This deformation mode has triggered the study of LCEs as potential candidates for artificial muscles. In case of GLCNs, due to limited mobility of polymer chains, thermomechanical actuation mainly occurs due to anisotropic thermal expansion, i.e., the coefficient of thermal expansion (α) is positive perpendicular to director axis and negative parallel to it.[84,85] Above the T_g , a limited amount of deformation occurs also due to reversible decrease in molecular order. Thus, uniaxially aligned GLCNs do not show considerable thermomechanical strains, however, by properly engineering the alignment of GLCNs, they can show other kinds of deformation such as bending and twisting.[84] Such alignment engineering involves variation of molecular alignment across the thickness of the LCN film, further discussed later in this section. Among the different polymeric architectures adopted i.e. main-chain, end-on and side-on LCNs, main-chain LCNs display the highest strains or active forces, due to strong coupling between mesogens and the polymer chains.[67] As mentioned elsewhere, different crosslink densities affect T_g and Young's modulus of these materials, which consequently affect their thermomechanical properties.[86,87] Hence, LCEs can produce higher stimuli-responsive deformation, whereas GLCNs can generate higher stimuli-induced stresses.[88,89] In addition to anisotropic optical properties, LCNs possess anisotropy in mechanical properties as well. Modulus of uniaxial LCNs is higher along the director \mathbf{n} , in comparison to modulus perpendicular to \mathbf{n} . [90]

LCNs are capable of undergoing different kinds of stimuli-induced shape changes, which is dictated by their molecular alignment[91] or, in some cases, gradients in crosslinking density.[92] In other words, two actuators (or two parts in a monolithic sample) with exactly the same chemical composition can behave

differently if they adopt different molecular alignments. Simple uniaxially aligned LCNs are capable of undergoing reversible in-plane contraction along the orientation direction, similar as the natural muscle-like motion. For actuation in a more complicated three-dimensional form, different alignment strategies have been used based on the principle of anisotropic deformation in LCNs. Due to the fact that LCNs tend to expand in the directions perpendicular to \mathbf{n} and contract parallel to it, programming of director orientation at each pixel in a 2D array can convert a 2D LCN sheet into a complex pre-programmed actuator undergoing 3D shape changes.[71,91]

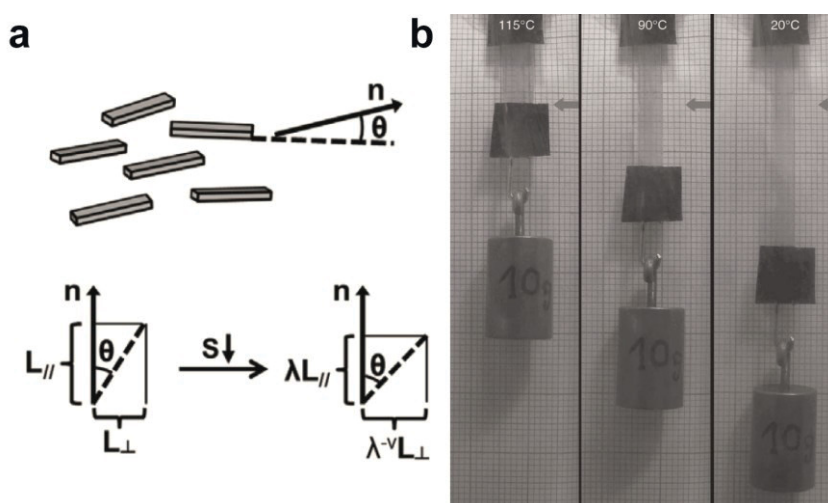


Figure 3.5 Thermomechanical actuation of LCN. **a)** decrease in molecular order causes contraction along director ($L_{||} \rightarrow \lambda L_{||}$) and expansion perpendicular to it ($L_{\perp} \rightarrow \lambda^{-\nu} L_{\perp}$), here L refers to length, λ and $\lambda^{-\nu}$ refer to contraction and expansion, respectively, and ν is Poisson's ratio. **b)** Thermal contraction of LCE sample along director, lifting a 5g load. Figures reproduced with permission: **a)** ref. [71]. Copyright 2014, Elsevier **b)** ref. [67]. Copyright 2010, John Wiley and Sons.

Bending constitutes the most studied actuation mode in LCNs. Unlike bimetallic cantilevers and their likes, LCNs do not need bilayer assembly to generate bending. A monolithic LCN strip can be designed to undergo bending by varying the alignment of the top and bottom surfaces or by implementing absorption gradient in case of photochemical actuation (discussed in section 3.3). Two common alignment configurations are used to create bending actuations: splay (Figure 3.6a), where molecules gradually tilt from planar alignment on one surface to homeotropic on the other, and twisted (Figure 3.6b), where the molecules make 90° in-plane

rotation across the thickness. Due to varying director within the sample, the two surfaces of the LCN strip experience inhomogeneous stimuli-induced strains, resulting in bending. Since contraction occurs along the director axis and expansion perpendicular to it, splay-aligned LCNs bend towards the surface having planar alignment and the twisted ones towards the surface having the director along the long axis of the bending strip.[81,84]

In splay-aligned or twisted LCN strips, the angle between the director and the long axis of the strip (denoted by ϕ) is crucial.[93,94] To obtain a pure bending deformation, ϕ should be close to zero. If ϕ deviates from zero, coiling deformation can be obtained in both splay and twisted LCNs. It is reported that in twisted LCN strips with $\phi = \pm 45^\circ$, the aspect ratio of the strip plays a role in determining the type of deformation.[93] High-aspect-ratio strips show helicoidal deformation, whereas, wider strips tend to coil. In addition to aspect ratio, the sign of ϕ determines the handedness of coiling, and deviation from $\pm 45^\circ$ leads to variation in pitch of coiling. In **Publication I**, we inscribe a gradient in ϕ along the length of splay-aligned strip, resulting in the coiling of strip with gradient in pitch.

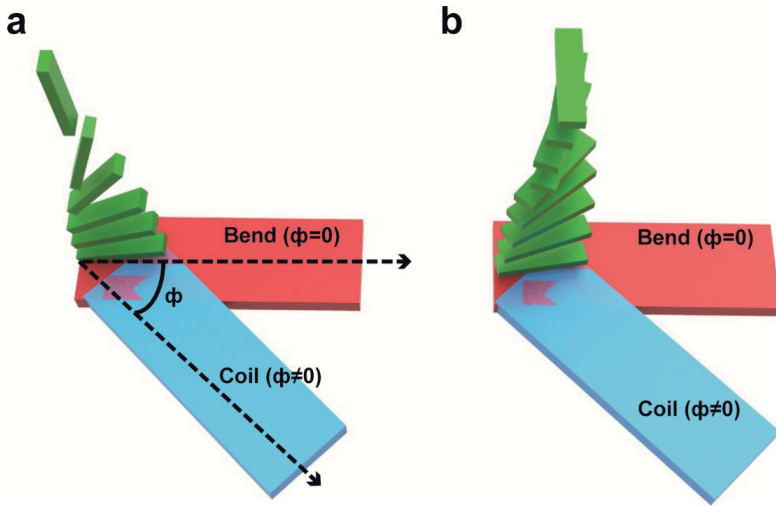


Figure 3.6 Schematics showing how deformation is dictated by molecular alignment in LCN strips having **a)** splay and **b)** twisted alignments.

In splay and twisted actuators, the director is varied along the thickness of the LCN film but remains unchanged within the plane. In-plane variation of the director can be commonly observed in unaligned polydomain LCs, with characteristic disclinations present in nematic LCs (discussed in section 2.2). Warner and co-

workers predicted theoretically that if a radially or azimuthally aligned +1 defect is adopted in LCNs, a flat sheet can be transformed into a saddle or conical shape, respectively.[95] Broer's group experimentally demonstrated this by inscribing +1 defect in an LCN using photoalignment technique (Figure 3.7).[96] This subsequently led to development of many methods for inscription of defect structures in LCNs such as laser scanning,[59] micro-channels,[97] photomasks[56] etc. In **Publication I** we used a commercial laser projector to inscribe +1 defect in LCN and in **Publication II** a laser setup consisting of polarization convertor was used to achieve radial molecular alignment.

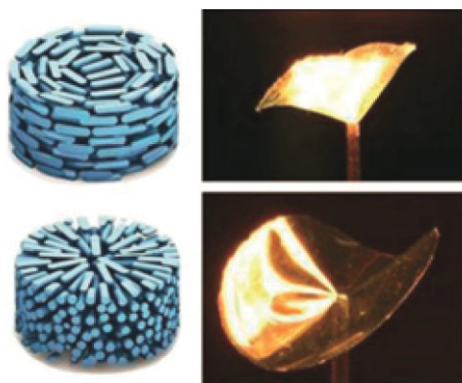


Figure 3.7 Schematics representing azimuthal (top) and radial (bottom) alignments along with their deformation in LCNs. Reproduced with permission: ref. [96]. Copyright 2012, John Wiley and Sons.

More complex shape changes have been achieved by patterning the in-plane variation of director using photoalignment and photopatterning. Schenning and co-workers patterned 90° twisted alignment in four regions of an LCN actuator, with each successive region having opposite twist directions.[98] This alignment patterning led to the bending of adjacent regions in opposite directions, resembling an accordion (Figure 3.8a). Broer and co-workers patterned a series of defects in an LCN film and carefully made some incisions along some of the defects, produces apertures into the film.[99] They were able to reversibly open and close these apertures using light irradiation. White and co-workers used raster scanning of laser beam with computer-controlled polarization to inscribe a 3-by-3 array of defects in an LCN film, which under thermal stimulus deforms reversibly into series of pyramids (Figure 3.8b).[79] In **Publication I**, a commercial laser projector was used to locally pattern the director orientation in arms of an octopus-like actuator, which

eventually is able to simultaneously bend its arms to opposite directions, under light illumination (see section 4.3).

Despite all the progress made towards programming of shape changes in LCNs, surface alignment of LCs limits the thickness of LCNs to few hundreds of micrometers. However, recent development of additive manufacturing techniques like 3D printing has provided opportunities to overcome this limitation. Ware and co-workers prepared 3D printed LCNs, where the alignment was induced by the flow of LC molecules from the nozzle.[72] Different 3D structures were demonstrated to undergo efficient heat-triggered actuation (Figure 3.8c). Sánchez-Somolinos *et al.* also fabricated LCN actuators using 3D printing and demonstrated an adaptive lens by combining a 3D printed LCN ring with polydimethylsiloxane (Figure 3.8d).[73] Lewis and coworkers, in turn, used 3D printing to prepare several 3D LCN structures, which were consequently able to lift more weight as compared to conventionally made LCNs.[99] Looking at the initial success of 3D printing in LCNs, more breakthroughs are expected in future.

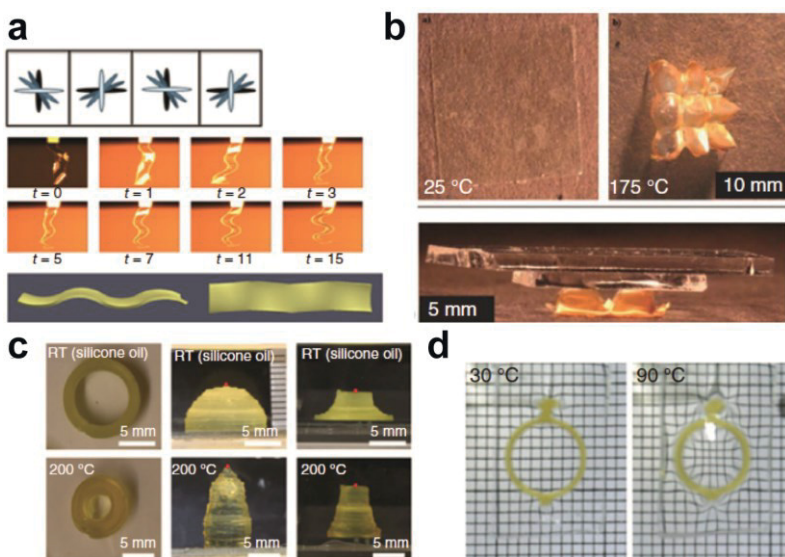


Figure 3.8 Different examples of LCN actuators having patterned molecular alignment. Figures reproduced with permission: **a)** ref. [98]. Copyright 2014, John Wiley and Sons. **b)** ref. [79]. Copyright 2015, AAAS. **c)** ref. [72]. Copyright 2017, ACS. **d)** under the terms of CC-BY-NC-ND: ref. [73]. Copyright 2018, The Authors.

In addition to molecular alignment, temperature of polymerization plays an important role in determining the initial shape of splay-aligned LCN strips. If a splay-aligned LCN film is polymerized at elevated temperature, the freestanding film is

initially bent at room temperature (RT) due to temperature-dependent anisotropic length changes occurring at the top and bottom surfaces of the LCN film,[84,85] and remains flat only at the polymerization temperature. Hence, if the temperature of polymerization is above room temperature, cooling down to RT leads to contraction at the homeotropic surface and expansion at the planar surface, causing the film to spontaneously bend towards the homeotropic side. Similarly, polymerization below room temperature would lead to initial bending (at RT) towards the planar side. Hence, by properly choosing the polymerization temperature, initial shape of LCN film can be programmed, which together with alignment patterning can lead to complex, pre-determined shapes. This concept has been used in **Publication II** and **Publication IV** to control the initial shape of the photoactuable segments in the artificial iris and nocturnal flower structures (see section 4.3).

3.3 Photomechanical actuation using azobenzenes

Photomechanical actuation of LCNs is one of the core interests in contemporary stimuli-responsive material research.[100] Light, as a stimulus, is attractive due to its abundant availability, high spatial and temporal control, clean and non-toxic nature and ability to trigger the actuation remotely. Photoactuation in LCNs can occur via two mechanisms, photochemical and photothermal actuation. In the photochemical mechanism, the actuation is triggered by conformational change of photoswitchable molecules that undergo reversible photoisomerization between two isomeric states. Photothermal actuation, in turn, is similar to thermomechanical actuation (Section 3.2), except that the heat is produced indirectly and remotely, via light irradiation. In this thesis, we used molecules based on azobenzenes, which can trigger actuation of LCNs via both these mechanisms. Before discussing the actuation of LCNs containing azobenzenes, a brief introduction to photochemistry of azobenzenes is presented.

Azobenzene is an organic molecule, which consists of -N=N- double bond substituted with two phenyl rings. Azobenzenes (referring to both unsubstituted azobenzene and its derivatives) undergo reversible photoisomerization around the -N=N- double bond by switching between E and Z isomeric states i.e. a stable *trans*-form and a metastable *cis*-form, respectively.[101] For the unsubstituted azobenzene (and the azobenzene crosslinks used in this work), *trans*-to-*cis* isomerization takes place under UV irradiation and *cis*-to-*trans* isomerization occurs either thermally or

via visible-light irradiation (c.a. > 450 nm). The mechanism of azobenzene isomerization has been studied for decades, and is believed to occur either through in-plane inversion about the $-N=N-$ bond or out-of-plane rotation around $-N=N-$ bond, depending on both the molecular structure and the environment.[102]

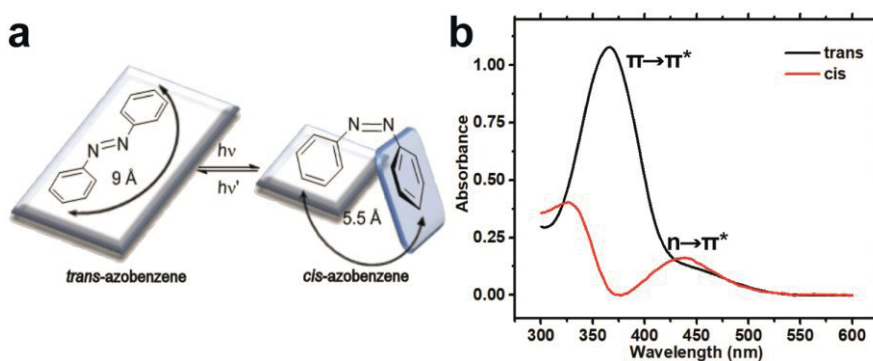


Figure 3.9 Azobenzene photoisomerization and associated changes in a) end-to-end length and b) UV-Vis absorption spectra. Figure a) reproduced with permission under the terms of CC BY 2.0: ref. [101]. Copyright 2012, The Authors.

Light-induced isomerization of azobenzenes is accompanied with changes in some of the physical properties such as molecular geometry, dipole moment and absorption spectra.[101] *Trans*-azobenzene has a planar structure with no dipole moment and the end-to-end distance between carbons at position 4 of rings is around 9.0 Å. (Figure 3.9a) The *cis*-isomer has an angular bent geometry with dipole moment of 3.0 D and the end-to-end distance decreases to around 5.5 Å. Due to steric repulsion between the π -electron clouds of aromatic rings in the *cis*-form, one of the ring rotates, resulting in a non-planar structure. UV-Vis absorption spectrum (Figure 3.9b) of *trans*-azobenzene is characterized by a strong absorption band in UV region that corresponds to $\pi \rightarrow \pi^*$ electronic transition and a weak band in visible region corresponding to symmetry-forbidden $n \rightarrow \pi^*$ transition. In *cis*-form, the $\pi \rightarrow \pi^*$ band becomes weaker and blue-shifted, while the $n \rightarrow \pi^*$ transition becomes allowed and thereby its intensity increases compared to the *trans*-form. Substitution of azobenzenes leads to the change in wavelength of absorption band corresponding to $\pi \rightarrow \pi^*$ transition. Accordingly, azobenzenes are commonly sub-divided into three types: azobenzene-type, aminoazobenzene-type and pseudostilbene-type.[103] The absorption properties of azobenzene-type molecules are similar to those of unsubstituted azobenzenes, discussed above. Aminoazobenzenes have an electron-donating substituent at *ortho* or *para* position, which leads to partial overlapping

between the $\pi \rightarrow \pi^*$ and $n \rightarrow \pi^*$ absorption bands. In pseudo-stilbenes one end of azobenzene is substituted with an electron-donating and other with an electron-withdrawing group – a push-pull strategy, which leads to red-shifting of $\pi \rightarrow \pi^*$ band, reversing the energy order of the two bands.

In **Publication I** we used two types of azobenzenes to prepare LCNs. Among them one is a diacrylated azobenzene-type reactive mesogen (**azo-1**) and the other is a pseudostilbene-type dye, Disperse Red 1 (**azo-2**). The chemical structures of these molecules, along with their UV-Vis spectra are given in Figure 3.10a-b. In addition to changes in absorption spectra, substitution has an effect on the thermal lifetimes of the *cis*-isomer. Typically, azobenzene-type molecules relax from *cis* to *trans* form in hours, aminoazobenzenes in minutes and pseudostilbenes in seconds.[104] The lifetime also depends on the molecular environment e.g. solvent or polymer matrix.[88,105]

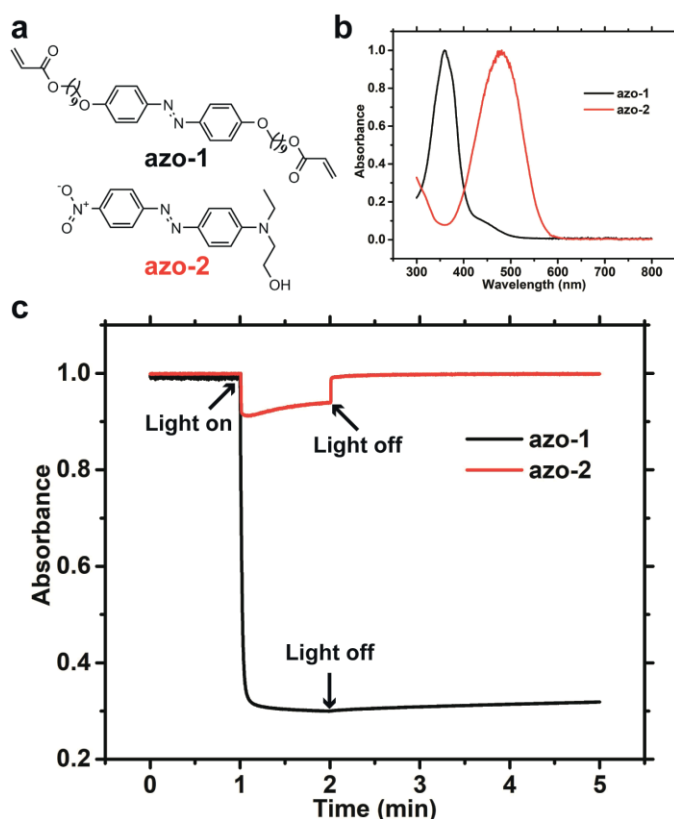


Figure 3.10 a-b) Structures of two azobenzene derivatives used for making LCNs in **Publication I**, along with their UV-Vis absorption spectra in chloroform, **c)** Absorption kinetics of LCN films containing **azo-1** (at 365nm) and **azo-2** (at 500nm) upon irradiation with 385nm and 460nm light, respectively.

As mentioned in the beginning of this section, photoactuation in azobenzene based LCNs occurs via photothermal or photochemical mechanisms. Photochemical actuation is triggered by photoisomerization of azobenzene from *trans* to *cis* isomer. Azobenzenes are known to disrupt the order of LCs upon irradiation with UV light via *trans-cis* isomerization, thereby causing photoinduced order-to-disorder transitions in LCs.[105] Due to the orientational coupling between azobenzenes and polymer network, the molecular-scale motion (photoswitching) is amplified into macroscopic shape change of LCN, resulting in photoactuation.[24] There exists an absorption gradient across the LCN film thickness, causing the surface facing light source to become more *cis*-isomer rich as compared to one away from light. Hence, photochemical actuation usually produces bending deformation. Difunctional azobenzenes, that are either crosslinked into LCN or present in main-chains, yield higher light-induced deformation compared to ones present in side-chains.[86,106] In photothermally triggered actuation, azobenzenes act as nanoscopic heat generators by converting some of the absorbed light energy into heat via non-radiative processes.[107,108] Discussions regarding the contribution of photothermal effect in azobenzene photomechanics has been ongoing since 1979.[109] Usually, it is not very straightforward to distinguish between these two mechanisms,[66] however, one of these effects may dominate the actuation process, depending on the specific type of azobenzene being used.

In **Publication I**, photoactuation of LCNs containing **azo-1** is dominated by photochemical mechanism and that of the ones containing **azo-2** by photothermal mechanism. The difference comes mainly from the fact that *cis*-isomer lifetime of **azo-1** and **azo-2** are in the order of hours and seconds, respectively, and partly due to the reason that **azo-1** was covalently crosslinked to the LCN, while **azo-2** was only doped into the network. Photochemical actuation mechanism of LCNs containing **azo-1** is quite evident as these LCNs retain their deformed state even after light is turned off and can relax back to their initial state upon *cis-trans* back isomerization of **azo-1** (either thermally or with light). On the other hand, short *cis*-lifetime of **azo-2** enables efficient transfer of photon energy to heat via repetitive *trans-cis-trans* cycles, thereby, triggering photothermal actuation. Light-induced decrease in absorption spectra of LCNs containing **azo-1** (385 nm, 100 mW cm⁻²) and **azo-2** (500 nm, 100 mW cm⁻²) are compared in Figure 3.10c. It is clear from the spectra that the photostationary state of the **azo-1** sample is more *cis*-rich, and the lifetime of the *cis*-isomer is long. For **azo-2**, the irradiation drives the isomerization reaction to both directions, and also the *cis*-lifetime is very short. Hence, fast cycling of **azo-2** between *trans* and *cis* states leads to higher photothermal heat generation,

as we have verified in many instances with thermal camera imaging. Nevertheless, both photochemical and photothermal mechanisms are important for designing light-driven devices because very different functionalities can be achieved. For example, photochemical actuators enable bistable actuation and actuation in aqueous environment, useful for biomedical applications, while photothermal actuation allows fast actuation and relaxation, important for fields like soft robotics.

Azobenzene-based LCN (azo-LCNs) actuators have received lots of attention in the last two decades. Many interesting demonstrations have been reported in literature. Ikeda and co-workers demonstrated directional bending in azo-LCNs,[80] followed by the light-driven azo-LCN motor,[110] and actuator resembling walking of an inchworm and movement of robotic arm (Figure 3.11a-b).[111] Photomechanically driven cantilever oscillators has been another interesting actuation mode in azobenzene based LCNs, initially reported by White *et. al.* (Figure 3.11c).[112] Here, the azo-LCN cantilever was exposed to a focused laser beam, triggering the bending of cantilever through the laser path, which in turn exposes the back surface of the cantilever to laser irradiation and causes bending in the opposite direction. This process gets repeated in a sequential way, causing high-frequency oscillations of the cantilever. Yu and co-workers used the combination of azo-LCNs and polyethylene films to make a bilayer robotic structure which consisted of parts resembling ‘arm’, ‘wrist’ and ‘hand’ (Figure 3.11d).[113] By exposing specific parts of this robot to visible light, they were able to grip, lift, move and drop an object remotely. LCEs with azobenzenes in main-chain were reported by White and co-workers via aza-Michael addition reaction.[114] They reported an increase of photomechanical deformation to around a factor of 5, as compared to +1 defect-based conical deformation in earlier-reported azo-GLCNs. Other efforts involved the chemical modification of azobenzene to shift their absorption in human-friendly visible range and the use of *ortho*-fluorinated azobenzenes with long *cis*-lifetime to realize truly bistable actuators, with a possibly of switching by visible light.[115–117] White and co-workers demonstrated a continuous motion of azo-LCN-based spiral ribbon over long distances, under broad-spectrum UV-vis irradiation (Figure 3.11e).[118] The motion occurs due to generation of asymmetric light-induced strains, as a result of increased twist in upper surface of the ribbon, while the bottom surface is being self-shadowed. Oscillatory behavior of azo-LCN cantilevers has recently been exploited by Broer and co-workers to demonstrate a fascinating wave-like deformation of an LCN device that is capable of autonomous walking under continuous visible-light irradiation (Figure 3.11f).[119] In addition to cantilever oscillations, Broer and co-workers have extensively used azo-LCNs to generate

dynamic, photoswitchable surface topographies based on thin-film coatings.[120–122] The coatings can even be made to oscillate, by continuously rotating the direction of polarized UV light.[123]

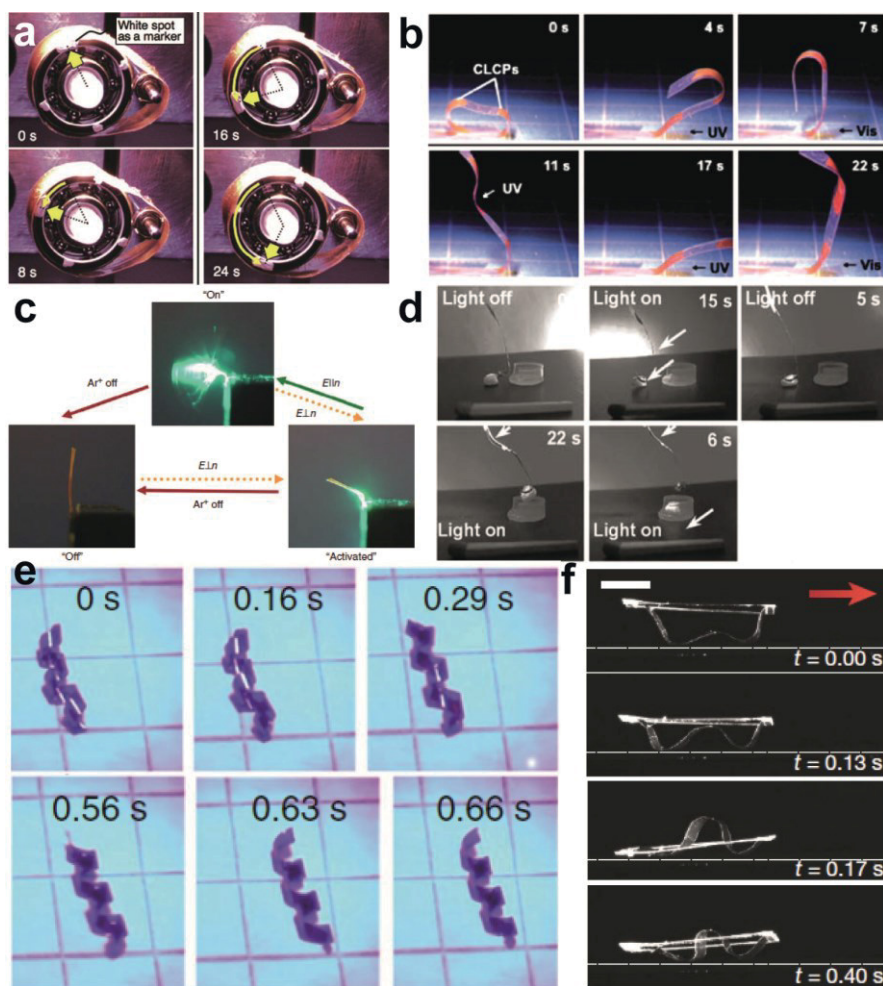


Figure 3.11 Examples of azo-LCN-based photoactuators: **a)** a light driven plastic motor, **b)** composite azo-LCN showing movement resembling robotic arm, **c)** oscillating cantilevers, **d)** light robot capable of gripping and releasing a target object, **e)** spiral azo-LCN capable of moving under continuous light irradiation and **f)** light robot showing wave-like translating deformation under continuous light irradiation. Figures reproduced with permission: **a)** ref. [110]. Copyright 2008, John Wiley and Sons. **b)** ref. [111]. Copyright 2009, RSC. **c)** ref. [112]. Copyright 2008, RSC. **d)** ref. [113]. Copyright 2010, RSC. **e)** under terms of CC BY 4.0, ref. [118]. Copyright 2016, The Authors. **f)** ref. [119]. Copyright 2017, Springer Nature.

4 BIOINSPIRED LIQUID CRYSTAL BASED LIGHT ROBOTS

Biological materials are adaptive - a feature which has been challenging to replicate in artificial systems. However, by learning from the design principles of biological materials, several sophisticated artificial responsive systems have been developed. For example, self-healing materials were inspired by bones and vascular tissues,[124] color-changing materials from butterflies, chameleons, beetles, natural opals etc.,[125] and materials with variable adhesion from Gecko feet.[19] In addition to above-mentioned systems, nature also provides us with many examples of shape-morphing in structures across different length scales.[20,126–128] These natural shape-changing materials can be useful in the design of small-scale soft robots that are programmable, able to self-regulate their action and adaptive to changes in surrounding environment. Soft robots have clear advantages as compared to conventional hard robots in terms of human-friendliness and compliance.[22,129] To realize new generation soft robots with adaptive functionalities inspired by natural systems, it is pertinent to develop smart materials that can respond to multiple stimuli, at the same time being programmed for different pre-determined shape changes.

LCNs have the ability to undergo reversible and programmed shape changes in response to variety of stimuli, hence, they are important candidates for the development of bioinspired robots. Although research in this field is still at the nascent level, significant progress has been made over the last few years. Bioinspired LCN-based light robots form the core of this thesis. Here, the word ‘light’ refers to both light-weight (i.e. small-scale) and light as a stimulus to trigger actuation.[25] In this chapter, we will first mention some examples of natural systems present in animal and plant kingdoms that serve as an inspiration for the development of actuators. After that, some of the previously demonstrated bioinspired LCN light robots will be discussed. Finally, the bioinspired LCN based light robots demonstrated in the publications of this thesis will be summarized, highlighting the advances they bring to the field of soft robots in general and to LCN actuators in particular.

4.1 Inspiration from biological actuators

In animals, one of the most important and distinguished features is their ability to move parts of the body and undergo locomotion. The body movement is driven by contraction and expansion of muscles. Animal muscles have inspired vast number of studies for development of actuators acting as artificial muscles.[130] Soft animals like worms, caterpillars and octopus, which do not possess rigid skeleton or joints, have developed unique gaiting strategies for their movement, well-controlled by neural systems.[129] They have been particularly inspirational for the study of soft robot locomotion and structural design of soft actuators.

In most animals, there exists an intriguing example of natural actuator i.e. an eye. In eyes we observe two kinds of system, i.e., lens and iris, which act as efficient actuators.[131] The lens is flexible and can change its curvature to focus on either nearby or distant objects; the iris can regulate its aperture size depending on the intensity of light and thereby control the amount of light passing through it onto the retina. Both lens and iris are a source of inspiration for smart actuators, especially in the design of smart optical components.

It is well known that aircrafts were inspired from bird flights. However, modern aircrafts lack the flexibility and adaptability as found in birds, which can help largely to reduce the drag and noise.[132] Aircrafts with flexible wings is one of the interesting topics in aeronautical research. For example, NASA is working on building aircrafts with hyperelastic rubber wings that can potentially lead to economical flights and reduction in noise during take-off and landing.[133] Similarly, aquatic swimmers such as fish have inspired design and gaiting strategy of many swimming robots, which can not only be useful for underwater expeditions but also serve as a tool to monitor environmental quality of water bodies.[134]

Plant kingdom has a rich diversity of stimuli-responsive species, which are capable of actuating their organ movements in response to multiple external stimuli. These species can respond to humidity, touch, light, etc. providing an endless source of inspiration to the design of artificial actuators.[21,135] One common example is pine cone, which responds to environmental humidity by opening its scales in dry conditions while they remain closed in humid conditions - a mechanism required for seed dispersal. Orientation of cellulose fibrils plays an important role in the bending of the pine scales, which is based on cell wall swelling and shrinkage.[136]

Some plant species such as Venus flytrap and mimosa are able to undergo rapid deformation in response to stimulus of touch, by folding their leaves. The fastest movement in a plant organ is the snap-close motion of Venus flytrap, taking place

in about 100 ms.[137] The rapid movements in species like mimosa and Venus flytrap are due to changes in turgor pressure, while, in case of Venus flytrap some other factors like elastic instability and the geometry of leaf surface is believed to increase the actuation speed. Opening and closing of flowers is also regulated by light, heat and, in some cases, humidity.[138] Likewise, plants can also regulate the pore size of stomatal opening to control the gas exchange with environment.[139] Another interesting example is presented by the dispersal of spores in a catapult mechanism by ferns, which is based on the cohesion forces of water.[140] The above-mentioned species, together with other numerous examples, have inspired the design of bioinspired actuators in general, including LCN-based light robots.

The ability of natural actuators to predetermine their shape morphing, autonomously adapt to the changing environment, self-regulate their actuation and in some cases being able to detect and distinguish their prey, has been challenging to mimic in artificial systems. By learning from the design principles of nature, smart artificial systems can be envisioned. These systems would, however, demand the development of materials that are multiresponsive, programmable, and can be controlled to a high degree. Materials based on LCNs, as described in Chapter 3, meet many of these qualities, therefore being good candidates for bioinspired robotic design.

4.2 Review of previous studies

As two pioneering examples of bioinspired light robots, Ikeda and coworkers used combination of azobenzene containing uniaxially oriented GLCNs with low-density polyethylene film to prepare photoactuators and demonstrated light-induced deformation of films resembling walking of an inchworm, as schematized in Figure 4.1a.[111] Broer and co-workers used inkjet printing to fabricate splay-oriented azobenzene-containing GLCN microactuators which were able to mimic the bending motion of natural cilia (Figure 4.1b).[141] These printed artificial cilia consisted of two regions containing different azobenzene molecules, which can be actuated by two different wavelengths of illumination. This enables artificial cilia to produce non-reciprocal motion by controlling the irradiated light wavelength, which can be potentially used in microfluidic devices. Jiang and co-workers inspired by the heliotropism in nature, prepared a solar panel device, which utilized sunlight-driven actuation of nanocomposite LCEs to follow the track of sun for increased light interception.[142] The LCE nanocomposite consisted of incorporated single-walled

carbon nanotubes (SWCNTs) for photothermal actuation and polyurethane fiber-network for reinforcement, with alignment being achieved by drawing process.

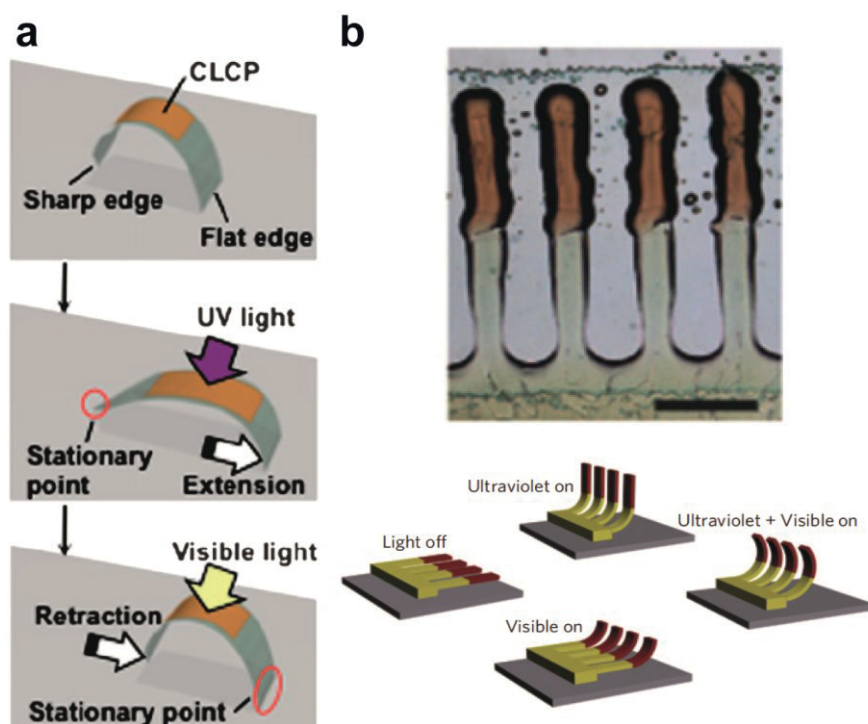


Figure 4.1 a) Light-driven inchworm-inspired walking robot prepared from composite bilayer LCN, and b) artificial light-driven cilia producing non-reciprocal motion. Figures reproduced with permission: a) ref.[111]. Copyright 2009, RSC. b) ref.[141]. Copyright 2009, Springer Nature.

White and co-workers demonstrated a snap-through motion in azobenzene-functionalized amorphous and liquid crystal polymer strips based on mechanical instabilities inspired from the snapping of Venus flytrap (Figure 4.2a).[143] The reported snapping of bi-stable arches was capable of generating enhanced actuation speed and power. Chen and coworkers demonstrated fast actuation in a bilayer actuator containing SWCNT and IR dye doped active LCN layer and silicon based passive layer.[144] By modifying the design of the actuator, they were able to show a walking device inspired by inchworm climbing. Katsonis and co-workers were inspired by the coiling motion in plant tendrils and demonstrated spring-like LCN actuators that were able to show complex light-induced helical motions such as

winding, unwinding and helix inversion (Figure 4.2b).[94] Diversity of shape changes in these LCN springs was achieved by properly choosing the cutting angle between the midplane director and the long axis of the twisted nematic LCN strip. The springs were also shown to perform work by moving a macroscopic object. Wiersma and co-workers demonstrated a light-fueled microscopic walker based on LCN actuator.[145] They used direct laser writing to fabricate the walking device, which consisted of an active LCE body and legs prepared from acrylic resin. The legs of the walker were pointed to reduce the surface contact area and tilted to induce asymmetry in adhesion, promoting directional motion at microscopic scale (Figure 4.2c). Wasylczyk and co-workers reported a caterpillar-inspired robot prepared by modifying the alignment of an LCN strip, which was able to move by travelling wave-like deformation upon non-reciprocal scanning of a laser beam (Figure 4.2d).[146]

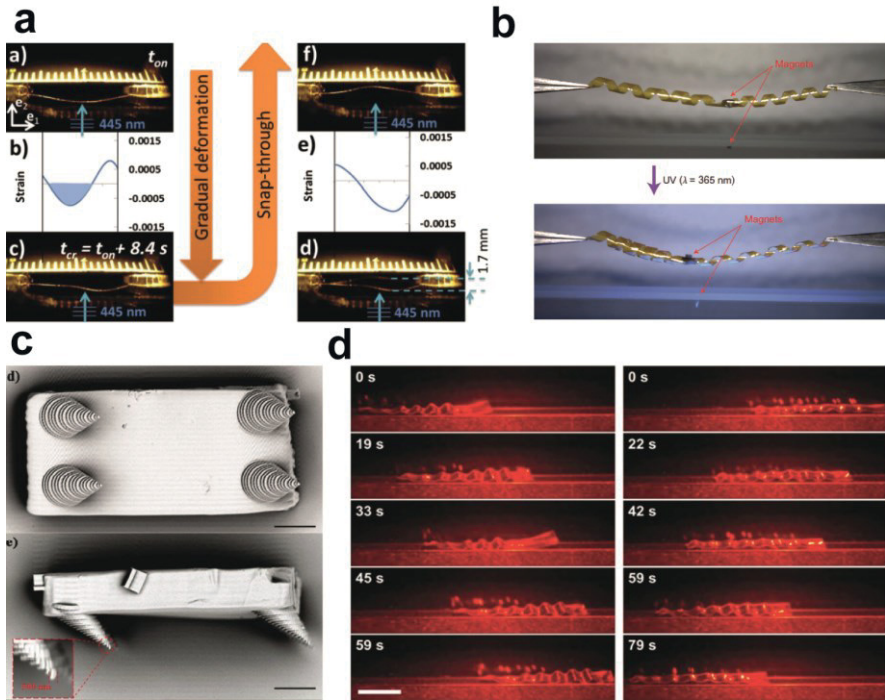


Figure 4.2 **a)** Snapping motion of azo-LCN strip based on elastic instability as found in Venus flytrap. **b)** Coiling motion of azo-LCNs inspired by plant tendrils. **c)** Light-driven microscopic walker, fabricated by direct laser writing of LCNs. **d)** Travelling-wave deformation in a caterpillar-inspired walking light robot. Figures reproduced with permission: **a)** under the terms of CC BY-NC-ND ref. [143]. Copyright 2013, The Authors. **b)** ref. [94]. Copyright 2014, Springer Nature. **c)** under the terms of CC BY-NC ref. [145]. Copyright 2015, The Authors. **d)** ref. [146]. Copyright 2016, John Wiley and Sons.

Fischer and co-workers used structured light fields to generate swimming of an LCN-based microrobot.[147] Swimming of this microrobot was inspired from the locomotion of micro-organisms, which employs the mechanism of traveling-wave body deformation such as peristaltic locomotion of worms. Inspired from the opening of chiral seed pods, Katsonis and coworkers developed azo-LCN based actuators which are able to pop-open (Figure 4.3a).[148] The actuator consists of two LCN strips with opposing twist, which under light irradiation stores some elastic energy due to the restricted motion of the strips. At some instance, the elastic energy is rapidly released, resulting in pop-opening of the pod-resembling structure. Inspired by the ability of Gecko to strongly attach to any kind of substrate and rapidly detach from them at will, Gorb and co-workers designed a composite actuator containing azo-LCN, which is able to decrease its adhesion under UV light illumination to grip and release solid objects (Figure 4.3b).[149] Priimagi and co-workers demonstrated a caterpillar-shaped walking robot by patterning molecular alignment in azobenzene-based LCN.[150] This light driven robot requires less intense visible light and shows directional movement on a blazed grating (Figure 4.3c). Inspired by butterfly proboscis, Schenning and co-workers prepared an LCN film with tapered thickness, which shows a higher degree of coiling compared to films with uniform thickness LCNs (Figure 4.3d).[151]

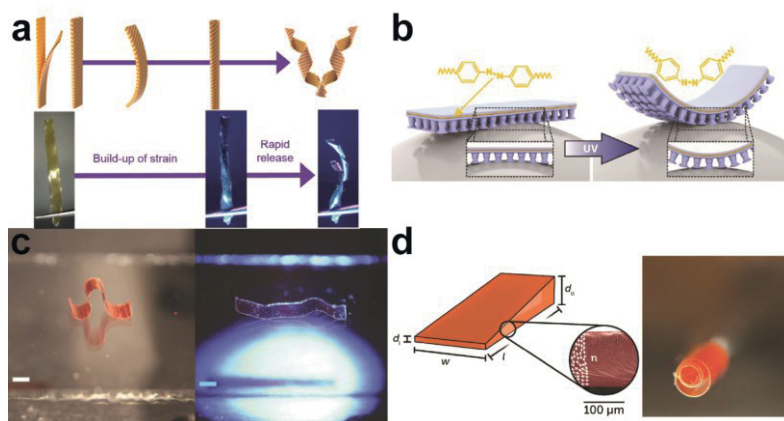


Figure 4.3 a) LCN-based seed pods capable of light-induced pop-opening. b) Composite azo-LCN capable of mimicking switchable adhesion of Gecko feet. c) Light-driven inching motion of azo-LCN fabricated via patterning of molecular alignment. d) Butterfly proboscis-inspired tight curling of tapered LCN films. Figures reproduced with permission: a) under the terms of CC BY-NC ref. [148]. Copyright 2017, The Authors. b) ref. [149]. Copyright 2017, AAAS. c) ref. [150]. Copyright 2018, John Wiley and Sons. d) ref. [151]. Copyright 2019, RSC.

4.3 Pre-determined shape morphing

Biological actuators morph into shapes that are pre-determined in their structures, with sophisticated control over the directionality of their movements.[20,127] For instance, flowers open into specific patterns, while the directionality of morphing petal is well controlled during each opening and closing cycle. Anisotropy in structural design is important for such behavior to exist.[21] LCNs have the ability to undergo programmed morphing and direction of that morphing can also be controlled by various methods (see Section 3.2) In this thesis, we achieved this feat by combination of molecular alignment patterning and choice of polymerization temperature of LCNs.

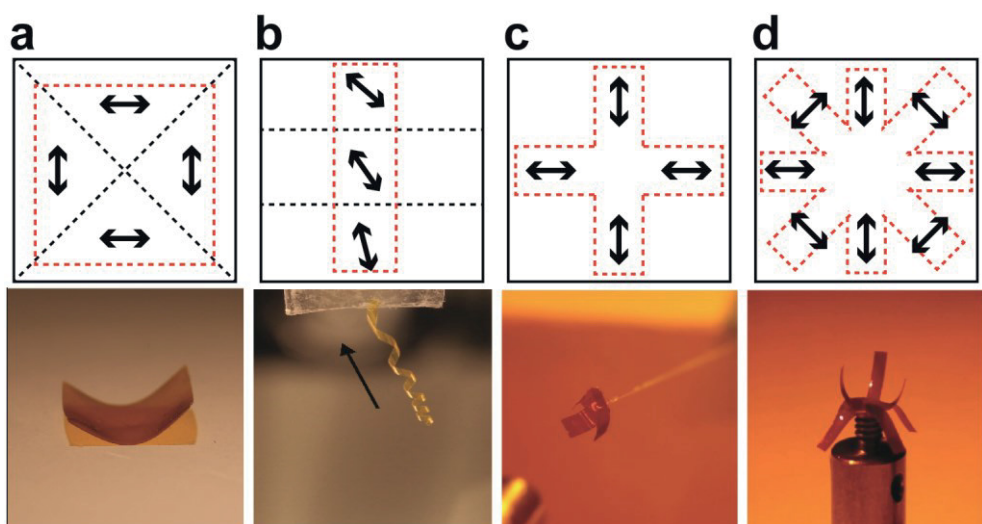


Figure 4.4 Photoalignment programming for shape morphing. **a)** +1 defect enabling conical deformation, **b)** gradient in director angle with respect to long axis of strip, giving a tapered coiling deformation, **c)** director parallel to all four arms, leading to bending towards center and **d)** opposite twisted alignment in successive arms, resulting in opposite direction bending of alternating arms.

In **Publication I**, a laser projector was used to pattern molecular alignment, which introduces a facile and cost-effective way for photoalignment in LCN actuators. Good quality alignment was obtained after exposure of photoalignment layer to projected laser pattern for around 5-10 min, with possibility of creating features with dimensions smaller than 100 μm . Using a combination of laser projector and a rotatable linear polarizer, we demonstrated different monolithic LCN actuators that show cone to anti-cone deformation, tapered coiling, 4-armed gripper and an

octopod movements (Figure 4.4). In these examples, alignment patterning and polymerization temperature determine the shape of the actuator and give control over morphing directionality. The demonstrated octopus-resembling movement in Figure 4.4d is an illustrative example of a light robot able to show bidirectional bending of its arms: upon light illumination, four arms of the monolithic LCN bend in one direction, while the other four bend in the opposite direction, simultaneously. In principle, more degrees of freedom can be realized in the movement of arms, by patterning more complex alignment patterns into the arms.

In **Publication II**, a laser setup equipped with a polarization converter was used to inscribe radial molecular alignment on one surface of the artificial iris, while the other surface has homeotropic orientation. The used polarization converter converts linearly polarized incident light into azimuthally polarized, which in turn radially reorients the molecules of the photoalignment layer, creating a radial surface anchoring condition. The overall alignment, thus achieved, is referred as splay-radial alignment (Figure 4.5a). By choosing the splay-radial alignment and polymerization temperature well above room temperature, the fabricated iris is able to remain open under no light irradiation, and after being exposed to light, each iris segment bends towards the center of the iris.

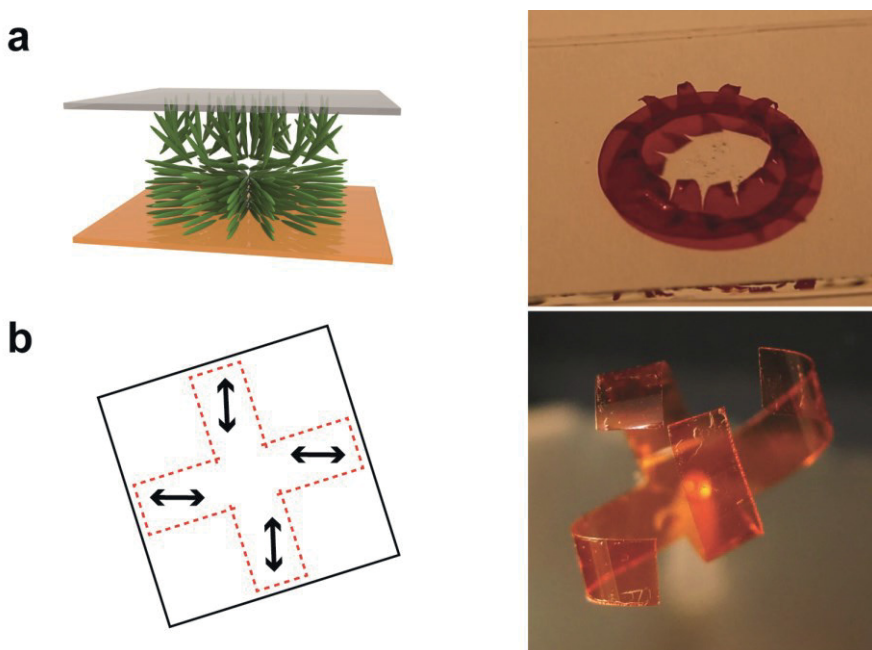


Figure 4.5 Schematic representation of alignment and the corresponding initial shape in **a)** artificial iris, and **b)** artificial nocturnal flower.

In **Publication IV**, we again used the combination of molecular alignment and choice of polymerization temperature to fabricate a flower-shaped actuator (Figure 4.5b). The curvature of petals was obtained by the combination of splay molecular organization with polymerization temperature well above room temperature. In addition to this, twist in the opening and closing of the artificial flower was imparted by offsetting the rubbing axis with respect to the long axis of petals. Furthermore, the directionality of the humidity-driven flower opening and closing was biased by selectively base treating only one of the flower surfaces.

4.4 From self-regulation to object recognition

One of the main results of this thesis is to realize self-regulation and object-recognition abilities in LCN actuators. The self-regulation, as demonstrated in **Publication II**, was inspired from iris present in eyes (see Section 4.1).[131] Here, the idea was to make a fully light-controllable artificial iris, that could tune its aperture size based on intensity of irradiated light and in turn regulate the amount of light transmitting through it. This demands a careful choice of device design (Figure 4.6), along with suitably programmed molecular alignment (see Section 4.3).

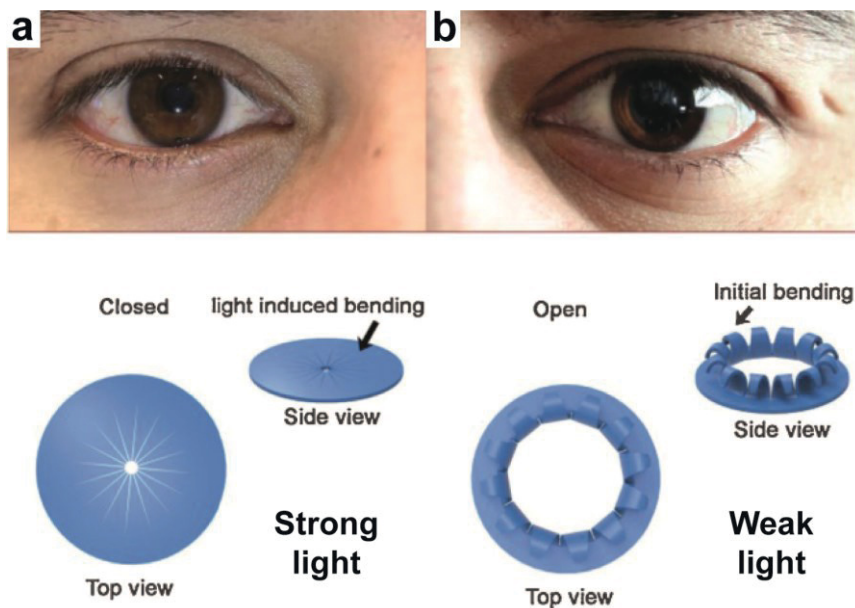


Figure 4.6 Picture of human iris (the author's eyes), along with a schematic representation of artificial iris in presence of strong (left) and weak (right) light field.

The fabricated iris consists of 12 segments cut from a freestanding LCN film, which tend to remain in a bent geometry in unactuated state i.e. under ambient light conditions (Figure 4.7a). The molecular alignment of these segments and the elevated polymerization temperature ensure the initial bent geometry, resulting in a maximum aperture size of the artificial iris under weak light. When the iris is irradiated with visible light (470nm, 250 mW cm⁻²) all the segments unbend towards the center, decreasing the aperture size (Figure 4.7b). The rate and amount of decrease in aperture size can be regulated with intensity of light, which in turn self-regulates the transmission of light across the iris itself.

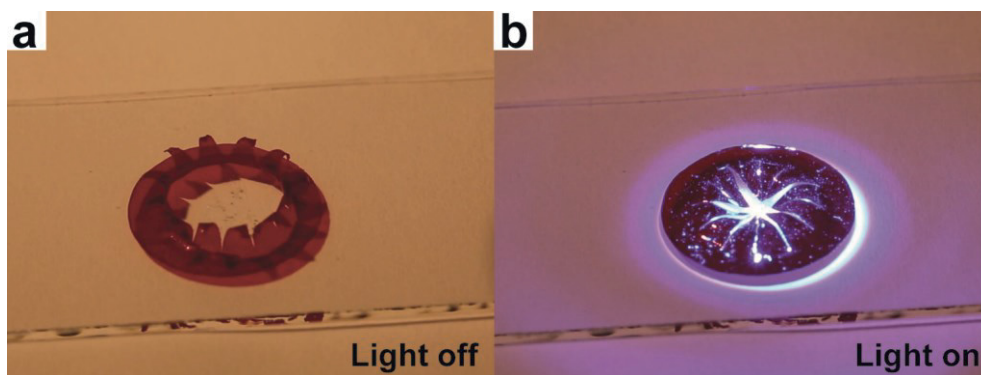


Figure 4.7 a) Iris in the open state in absence of light irradiation, and b) in the closed state upon illumination with 470 nm light.

The performance of the iris was characterized by irradiating the iris from one side with a 488 nm laser beam (diameter 12mm) and recording the transmission of light as a function of incident light power (Figure 4.8a). At low incident power (< 20 mW), 70 % of light is transmitted through the iris and by increasing the incident laser power, the segments start to deform inwards (20-120 mW). Above 120 mW, some segments unbend completely, bringing down the transmission through the device. Under 180 mW irradiation, all segments are closed, in which case only 10 % of incident light transmits through the device. To study the dynamics of the iris closure, we subjected the iris to instantaneous high-intensity irradiation of 270 mW cm⁻² and measured the time dynamics of light transmission. The transmission decreased in several steps, which is attributed to variation of closure time of the different iris segments (Figure 4.8b). Such variation is believed to be a result of fabrication imperfections such as small deviations in sample thickness, order parameter etc., leading to closure of some segments earlier than others.

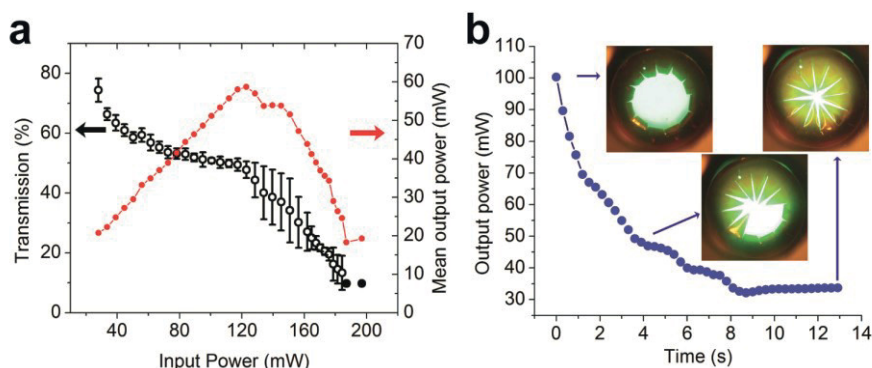


Figure 4.8 a) Decrease in light transmission through the artificial iris as a function of incident light power, and b) closure dynamics of the iris, revealing different steps corresponding to variation of closure time in iris segments.

In **Publication III** a new light robot, with “smart” actuation behavior is reported. The design and function of this actuator was inspired by the Venus flytrap,[137] which is attractive to bioinspired robotic research mainly for two reasons: firstly, the actuation in the Venus flytrap leaves is triggered automatically by the detection of prey and secondly, it is able to distinguish between real prey and a random dust or water droplet. Based on these two features, we fabricated a gripping light robot by integrating an optical fiber with a splay-aligned LCN actuator (Figure 4.9). The LCN actuator was glued to the tip of a laser-coupled optical fiber. The glued part is transparent and allows the light from the fiber to be transmitted through the actuator, without getting absorbed by the actuator. The transmitted light thus acts as a probe for sensing any objects that come into the probing area, as schematized in Figure 4.9. Depending on the optical properties of the encountered object, it may cause sufficient optical feedback via light scattering or reflection to the actuator and actuate the gripping arms.

We tested the object detection ability of the artificial flytrap by bringing an object with sufficient feedback in the probing area, with light turned on, which subsequently caused the actuation of the flytrap, resulting in gripping of the object (Figure 4.10a). The gripped object is released by turning off the light, which causes the relaxation of the gripper arms. In absence of any target, the arms of the flytrap gripper remain open. In addition to object detection, the reported artificial flytrap can also distinguish between targets with different optical feedback. To test this, three different targets were chosen, which included transparent, scattering and absorbing cubic targets. The flytrap was fixed at one place, while the targets are moved below it, using a custom-made production-line-type setup (Figure 4.10b). Each target was made to enter the field of view of the gripper, and among the three

targets, only the scattering target was selectively gripped by the flytrap, while there was no action in case of the other two targets. The gripped target could be lifted up, as the actuation causes enough friction (adhesion) to sustain the object, and ultimately released by turning off the light. In this way, the demonstrated device can detect and grip the objects with specific optical feedback, while remaining silent in case of non-reflecting targets – a skill of recognition. To the best of author’s knowledge, this is the first example of object recognition reported in LCN based light robots, and we believe it can open new avenues for adaptive, smart LCN robots.

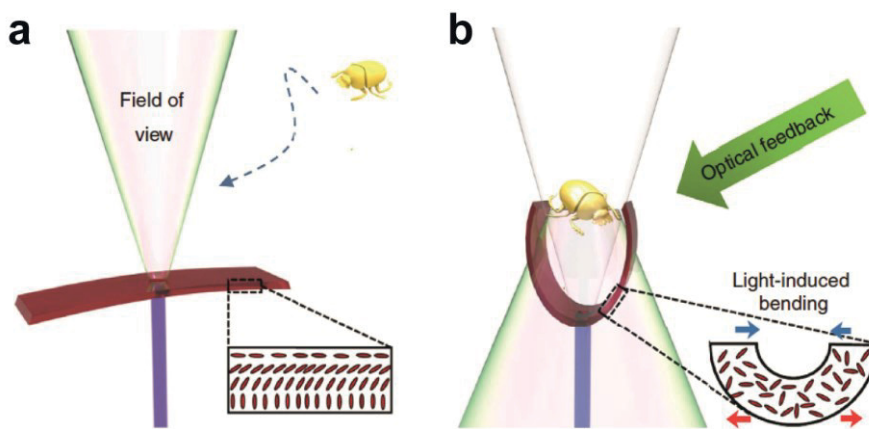


Figure 4.9 Scheme illustrating the design and working principle of the light-driven artificial flytrap.

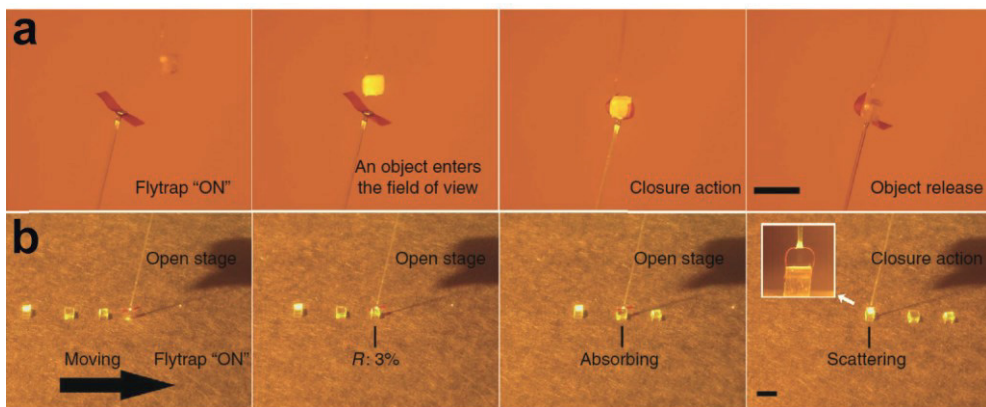


Figure 4.10 a) Autonomous object detection by artificial flytrap and b) its ability to distinguish between different objects based on optical feedback.

4.5 Towards humidity-gated actuation

In **Publication IV**, we aimed to make a multi-responsive actuator by integrating together light and humidity sensitivities. This work was inspired from certain species of nocturnal flowers whose opening/closing is regulated by light and humidity.[138] By mimicking such flowers, we aim to get a deeper understanding of actuation behaviors in dual-responsive systems under simultaneous exposure to light and humidity changes.

Humidity sensitivity was achieved in LCNs by modifying the composition of LC mixture, as already discussed in section 3.1. The as-prepared LCN is responsive to light due to the presence of **azo-2** type molecule (see Section 3.3) and the humidity sensitivity was achieved by treating the pristine LCN with basic solution (see section 3.1). Before base treatment the splay-aligned film expands on homeotropic side upon light illumination, decreasing the initial curvature (Figure 4.11a). However, after base treatment on homeotropic surface, initial curvature and the direction of light induced curvature change is humidity-dependent. At low relative humidity (RH), the film is tightly curved (closed) and when exposed to light its curvature decreases. At higher RH, the film opens up due to swelling on homeotropic surface, however, the curvature increases upon light irradiation. In other words, photoactuation leads to decrease in curvature at low RH and increase in curvature at high RH (Figure 4.11b). The light intensities needed to cause actuation at high RH were significantly smaller than those needed for actuation at low RH. Hence, the actuation of such systems is a result of delicate interplay between the stimulus of light and humidity.

The reason for such humidity-gated photoactuation was further studied and found to be a result of a competition between two different actuation mechanisms acting simultaneously. At low RH, the actuation is dominated by the general mechanism of actuation found in splay-aligned LCNs, i.e., expansion of homeotropic side due to decrease in molecular order induced by the photothermal effect, and simultaneous contraction of the planar-aligned side. This is evident from the fact that the actuation occurs at relatively higher light intensity, to generate enough temperature increase needed for decrease in molecular order. On the other hand, at high RH, the actuation occurs predominantly by light-induced desorption of water from the flower petals, taking place at lower temperatures and thus being thermodynamically favored over the decrease in molecular order.

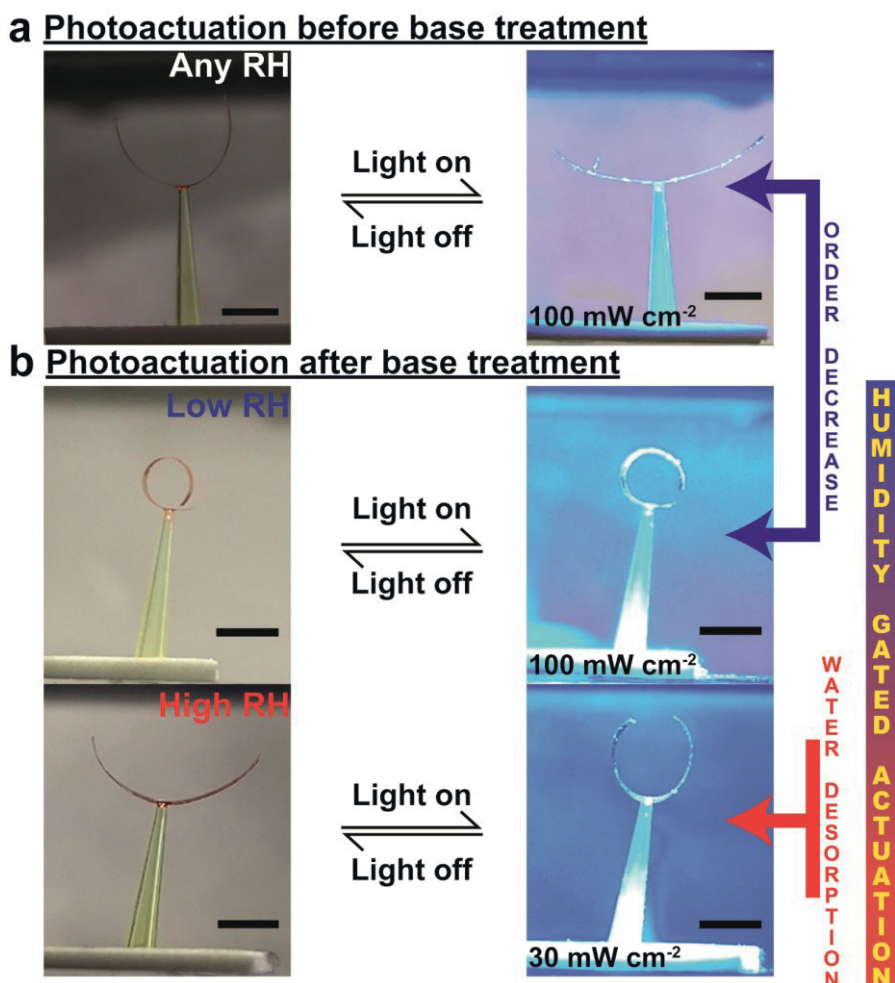


Figure 4.11 Difference in photoactuation mechanisms of LCN fabricated in **Publication IV**, a) before and b) after treatment with basic solution.

We confirmed this mechanism by comparing the temperature rise of light-exposed film (using IR camera) with the spectroscopically monitored loss of water upon heating. It was observed that most curvature change of LCN flower, kept at high RH, occurred at light intensities below 50-60 mW cm⁻², which according to thermal imaging causes a temperature rise of 7-10 °C (Figure 4.12a-b). Similarly, using infrared spectroscopy, we observed that 10 °C (from 20 to 30 °C) increase in temperature of the LCN film is enough to saturate the water loss, thereby resulting in the observed saturation of the curvature changes. This investigation thus verifies that the mechanism of actuation at high RH is indeed caused by light-induced loss

of water, which requires only small increase in temperature as compared to actuation at low humidity. Similar to certain nocturnal flowers, that open in dark assisted by high RH and close in daylight when the humidity is low, the demonstrated artificial flower-mimicking device also closes in presence of light (or low humidity condition) and opens when the light is turned off and the RH is high (Figure 4.12c).

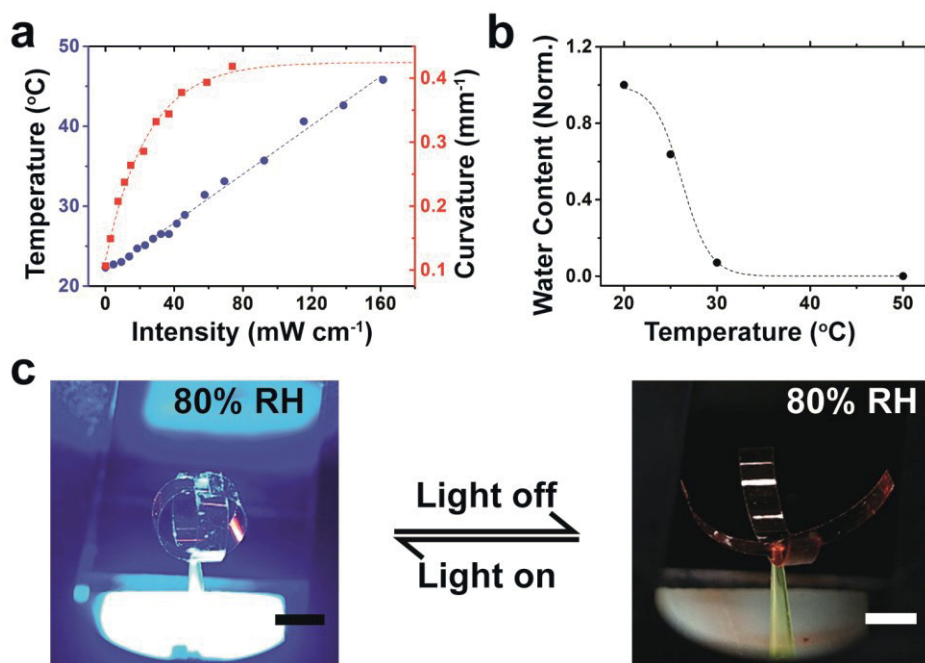


Figure 4.12 a) Plot of light-induced curvature change and temperature increase in the LCN-based artificial flower, b) loss of water content from LCN upon heating as estimated by infrared spectroscopy, c) LCN-based flower mimicking the opening and closing of certain nocturnal flowers by opening in dark and closing in presence of light, assisted by environmental humidity.

5 CONCLUSIONS AND OUTLOOK

In this thesis we used LCNs to design photoactuators with advanced functionalities, inspired from nature. We refer these photoactuators as bioinspired light robots. To make LCNs sensitive to light, azobenzene derivatives were incorporated either as dopants, or alternatively covalently bonded to the network. More precisely, a pseudostilbene-type azobenzene, Disperse Red 1, was used in all publications included in this thesis. Hence, the main mechanism of actuation in the works presented in this thesis is photothermal in nature. However, in **Publication I**, in addition to DR1, azobenzene crosslinkers were used, in order to provide photochemical actuation via photoisomerization of the azobenzene molecules. The combination of these two actuation mechanisms can itself be an important design principle for preparation of synergistic photoactuators, which are able to show complex actuation behavior, as demonstrated recently in ref. [107].

Many bioinspired light robots based on LCNs have been reported in the literature, as discussed in Section 4.2. This thesis intends to advance this intriguing field of research by implementing strategies inspired from intelligent natural actuators. We introduce novel concepts such as self-regulation and autonomous object recognition in the design of light robots, through two design principles. Firstly, we exploit alignment and shape programming of LCNs, which is a prerequisite for pre-determination of the actuation modes in the light robots. Secondly, we aim towards replicating some of the complex and intelligent actuation behavior occurring in natural systems and – in simplistic forms – bring those into LCN robots.

To this end, in **Publication I**, a commercial laser projector and the photoalignment technique are used for programmed morphing of light robots. Laser projector equipped with rotatable linear polarizer is able to pattern the molecular alignment of LCNs by spatially modulating the light polarization which, via the photoalignment layer, dictates the LC alignment prior to photopolymerization. This device provides a facile and cost-effective way of alignment patterning, without compromising the resolution. Several light robots with complex shape changes were demonstrated. In addition to alignment patterning, this study also discussed the

differences between the photochemical and photothermal modes of actuation in azobenzene containing LCNs.

In **Publication II**, inspired by the mammalian iris, we demonstrated a device which offers self-regulated (photo)control over its aperture size. Alike the natural iris, this artificial monolithic device decreases its aperture size as the intensity of incident light increases and *vice-versa*. Changes in the size of the aperture regulate, or more precisely self-regulate, the amount of light passing through the iris. Future research directions for the artificial iris are (i) fabrication of the iris from a biocompatible LCN material, (ii) reduction of light intensity and spectral range to which the iris responds to, and (iii) devising an iris-like structure that acts also in aqueous conditions. These developments could pave the way for the proposed iris-like device towards bio-related applications.

In **Publication III**, we implemented the actuation behavior which is reminiscent of a carnivorous plant known as Venus flytrap. The actuation behavior of Venus flytrap is very complicated and involves multiple collaborative effects from turgor movements, leaf geometry and elastic effects. We focus on autonomous action – an ability to detect and distinguish between targets – in single piece of polymer, via optical feedback mechanism. The fabricated LCN-based device is referred to as optical flytrap. Our light-driven flytrap relies on optical feedback (scattering or reflection of light) and thereby can detect and grip objects with strong reflection or scattering, while it remains dormant in case of objects that do not cause enough light feedback. The optical flytrap offers possibilities towards integration of (autonomous) LCN actuators in robotic systems. Further modification of the material composition can upgrade the device to react to objects based on different feedbacks, such as optical fields with varying wavelengths, polarizations, etc.

The curiosity-driven nature of this research also provided an opportunity for deeper exploration of actuation mechanisms responsible for LCN actuation. To this end, inspired by the multi-responsive actuation behavior present in certain nocturnal flowers, in **Publication IV** we devise a dual-responsive LCN actuator by combining light and humidity sensitivity in LCN actuators. The aim was to study the actuation behavior of such actuator upon simultaneous exposure to both light illumination and humidity change. The study reveals a delicate interplay between different stimuli existing in such combined actuators, i.e., a gating effect of humidity over the directionality of photoactuation, referred as humidity-gated photoactuation. More specifically, the combined actuator switches the light-induced bending direction depending on the environmental humidity.

The light robots demonstrated in this thesis represent a clear advance in the field of soft robotics in general and LCN-based robotics in particular. However, it must be noted that the field of LCN actuators is still in its infancy and its potential for applications is still being evaluated in many laboratories around the world. One of the main drawbacks has been the scaling up of these actuators due to limitations of fabrication procedure, restricting them to thin polymer strips. Nevertheless, recent developments in the field has enabled the development of 3D LCN actuators using additive manufacturing techniques like 3D printing. Another challenge is to increase the sensitivity of the LCN-based devices, so that their motion could be fueled entirely with sunlight. 3D light robots are envisioned to be potential candidates for smart medical implants. To achieve this goal, biocompatible actuating materials need to be developed. In a nutshell, LCN-based light robots can be considered as one of the future directions of adaptive systems and bioinspired design can help in imparting intelligence to them, and this thesis contributes a small step towards that goal.

BIBLIOGRAPHY

1. Chen, P.-Y.; McKittrick, J.; Meyers, M.A. Biological materials: Functional adaptations and bioinspired designs. *Prog. Mater. Sci.* **2012**, *57*, 1492–1704.
2. Srinivasan, A. V.; Haritos, G.K.; Hedberg, F.L. Biomimetics: Advancing Man-Made Materials Through Guidance From Nature. *Appl. Mech. Rev.* **1991**, *44*, 463–482.
3. Meyers, M.A.; Chen, P.-Y.; Lin, A.Y.-M.; Seki, Y. Biological materials: Structure and mechanical properties. *Prog. Mater. Sci.* **2008**, *53*, 1–206.
4. Wegst, U.G.K.; Bai, H.; Saiz, E.; Tomsia, A.P.; Ritchie, R.O. Bioinspired structural materials. *Nat. Mater.* **2014**, *14*, 23.
5. Liu, M.; Zheng, Y.; Zhai, J.; Jiang, L. Bioinspired Super-antiwetting Interfaces with Special Liquid–Solid Adhesion. *Acc. Chem. Res.* **2010**, *43*, 368–377.
6. Han, Z.W.; Wang, Z.; Feng, X.M.; Li, B.; Mu, Z.Z.; Zhang, J.Q.; Niu, S.C.; Ren, L.Q. Antireflective surface inspired from biology: A review. *Biosurface and Biotribology* **2016**, *2*, 137–150.
7. Su, B.; Tian, Y.; Jiang, L. Bioinspired Interfaces with Superwettability: From Materials to Chemistry. *J. Am. Chem. Soc.* **2016**, *138*, 1727–1748.
8. Cheng, Q.; Jiang, L.; Tang, Z. Bioinspired Layered Materials with Superior Mechanical Performance. *Acc. Chem. Res.* **2014**, *47*, 1256–1266.
9. Studart, A.R. Additive manufacturing of biologically-inspired materials. *Chem. Soc. Rev.* **2016**, *45*, 359–376.
10. Xia, F.; Jiang, L. Bio-Inspired, Smart, Multiscale Interfacial Materials. *Adv. Mater.* **2008**, *20*, 2842–2858.
11. Wang, R.; Gupta, H.S. Deformation and Fracture Mechanisms of Bone

- and Nacre. *Annu. Rev. Mater. Res.* **2011**, *41*, 41–73.
12. Cheng, Y.T.; Rodak, D.E.; Wong, C.A.; Hayden, C.A. Effects of micro- and nano-structures on the self-cleaning behaviour of lotus leaves. *Nanotechnology* **2006**, *17*, 1359–1362.
 13. Boesel, L.F.; Greiner, C.; Arzt, E.; del Campo, A. Gecko-Inspired Surfaces: A Path to Strong and Reversible Dry Adhesives. *Adv. Mater.* **2010**, *22*, 2125–2137.
 14. Srinivasarao, M. Nano-Optics in the Biological World: Beetles, Butterflies, Birds, and Moths. *Chem. Rev.* **1999**, *99*, 1935–1962.
 15. Kirschner, C.M.; Brennan, A.B. Bio-Inspired Antifouling Strategies. *Annu. Rev. Mater. Res.* **2012**, *42*, 211–229.
 16. Studart, A.R. Biologically Inspired Dynamic Material Systems. *Angew. Chemie Int. Ed.* **2015**, *54*, 3400–3416.
 17. Youngblood, J.P.; Sottos, N.R. Bioinspired Materials for Self-Cleaning and Self-Healing. *MRS Bull.* **2008**, *33*, 732–741.
 18. Isapour, G.; Lattuada, M. Bioinspired Stimuli-Responsive Color-Changing Systems. *Adv. Mater.* **2018**, *30*, 1707069.
 19. Lee, H.; Lee, B.P.; Messersmith, P.B. A reversible wet/dry adhesive inspired by mussels and geckos. *Nature* **2007**, *448*, 338.
 20. Studart, A.R.; Erb, R.M. Bioinspired materials that self-shape through programmed microstructures. *Soft Matter* **2014**, *10*, 1284–1294.
 21. Ingo, B.; Peter, F. Actuation systems in plants as prototypes for bioinspired devices. *Philos. Trans. R. Soc. A Math. Phys. Eng. Sci.* **2009**, *367*, 1541–1557.
 22. Hines, L.; Petersen, K.; Lum, G.Z.; Sitti, M. Soft Actuators for Small-Scale Robotics. *Adv. Mater.* **2017**, *29*, 1603483.
 23. Ionov, L. Hydrogel-based actuators: possibilities and limitations. *Mater. Today* **2014**, *17*, 494–503.

24. Ube, T.; Ikeda, T. Photomobile Polymer Materials with Crosslinked Liquid-Crystalline Structures: Molecular Design, Fabrication, and Functions. *Angew. Chemie Int. Ed.* **2014**, *53*, 10290–10299.
25. Zeng, H.; Wasylczyk, P.; Wiersma, D.S.; Priimagi, A. Light Robots: Bridging the Gap between Microrobotics and Photomechanics in Soft Materials. *Adv. Mater.* **2018**, *30*, 1703554.
26. Reinitzer, F. Contributions to the knowledge of cholesterol. *Liq. Cryst.* **1989**, *5*, 7–18.
27. Lehmann, O. Über fließende Krystalle. *Zeitschrift für Phys. Chemie* **1889**, *4U*, 462.
28. Gray, G.W. Introduction and Historical Development. In *Handbook of Liquid Crystals*; Wiley Online Books; **2008**; ISBN 9783527620760.
29. Friedel, G. Les états mésomorphes de la matière. *Ann. Phys.* **1922**, *9*, 273–474.
30. Yu, H. *Dancing with light: Advances in photofunctional liquid-crystalline materials*; Pan Stanford, **2015**; ISBN 978-981-4411-11-0.
31. Collings, P.J.; Fisch, M.R.; Mooney, M.A. Liquid Crystals: Nature's Delicate Phase of Matter. *Am. J. Phys.* **1992**, *60*, 958–958.
32. Oseen, C.W. The theory of liquid crystals. *Trans. Faraday Soc.* **1933**, *29*, 883–899.
33. Frank, F.C. I. Liquid crystals. On the theory of liquid crystals. *Discuss. Faraday Soc.* **1958**, *25*, 19–28.
34. Leslie, F.M. Theory of the Liquid Crystalline State: Continuum Theory for Liquid Crystals. In *Handbook of Liquid Crystals*; Wiley Online Books; **2008**; ISBN 9783527620760.
35. Osipov, M.A. Theory of the Liquid Crystalline State: Molecular Theories of Liquid Crystals. In *Handbook of Liquid Crystals*; Wiley Online Books; **2008**; ISBN 9783527620760.
36. Brown, G.H.; Shaw, W.G. The Mesomorphic State - Liquid Crystals.

- Chem. Rev.* **1957**, 57, 1049–1157.
37. Nash, J.A. New family of nematic liquid crystals for displays. *Electron. Lett.* **1973**, 9, 130–131(1).
 38. Friberg, S. Lyotropic liquid crystals. *Naturwissenschaften* **1977**, 64, 612–618.
 39. Demus, D. Chemical Structure and Mesogenic Properties. In *Handbook of Liquid Crystals*; Wiley Online Books; **2008**; ISBN 9783527620760.
 40. Collings, P.J.; Hird, M. *Introduction to Liquid Crystals*; Taylor & Francis, **1997**; ISBN 9788578110796.
 41. Demus, D. The Polymorphism of Liquid Crystals AU - Sackmann, H. *Mol. Cryst.* **1966**, 2, 81–102.
 42. Meier, G.; Saupe, A. Selective Reflection by Cholesteric Liquid Crystals AU - Dreher, R. *Mol. Cryst. Liq. Cryst.* **1971**, 13, 17–26.
 43. Dunmur, D.; Toriyama, K. Physical Properties: Optical Properties. In *Handbook of Liquid Crystals*; Wiley Online Books; **2008**; ISBN 9783527620760.
 44. Dierking, I. Polarizing Microscopy. In *Textures of Liquid Crystals*; Wiley Online Books; **2004**; ISBN 9783527602056.
 45. Dierking, I. Surface Anchoring and Elasticity. In *Textures of Liquid Crystals*; Wiley Online Books; **2004**; ISBN 9783527602056.
 46. Kahn, F.J.; Taylor, G.N.; Schonhorn, H. Surface-produced alignment of liquid crystals. *Proc. IEEE* **1973**, 61, 823–828.
 47. Takato, K.; Hasegawa, M.; Koden, M.; Itoh, N.; Hasegawa, R.; Sakamoto, M. *Alignment technologies and applications of liquid crystal devices*; Taylor & Francis, **2005**; ISBN 9780748409020.
 48. Flanders, D.C.; Shaver, D.C.; Smith, H.I. Alignment of liquid crystals using submicrometer periodicity gratings. *Appl. Phys. Lett.* **1978**, 32, 597–598.
 49. Janning, J.L. Thin film surface orientation for liquid crystals. *Appl. Phys.*

Lett. **1972**, *21*, 173–174.

50. Frisken, B.J.; Palffy-Muhoray, P. Fredericksz transitions in nematic liquid crystals: The effects of an in-plane electric field. *Phys. Rev. A* **1989**, *40*, 6099–6102.
51. Yaroshchuk, O.; Reznikov, Y. Photoalignment of liquid crystals: basics and current trends. *J. Mater. Chem.* **2012**, *22*, 286–300.
52. Priimagi, A.; Barrett, C.J.; Shishido, A. Recent twists in photoactuation and photoalignment control. *J. Mater. Chem. C* **2014**, *2*, 7155–7162.
53. Ichimura, K.; Suzuki, Y.; Seki, T.; Hosoki, A.; Aoki, K. Reversible change in alignment mode of nematic liquid crystals regulated photochemically by command surfaces modified with an azobenzene monolayer. *Langmuir* **1988**, *4*, 1214–1216.
54. Shannon, P.J.; Gibbons, W.M.; Sun, S.T. Patterned optical properties in photopolymerized surface-aligned liquid-crystal films. *Nature* **1994**, *368*, 532–533.
55. Schadt, M.; Schmitt, K.; Kozinkov, V.; Chigrinov, V. Surface-Induced Parallel Alignment of Liquid Crystals by Linearly Polymerized Photopolymers. *Jpn. J. Appl. Phys.* **1992**, *31*, 2155–2164.
56. Guo, Y.; Jiang, M.; Peng, C.; Sun, K.; Yaroshchuk, O.; Lavrentovich, O.; Wei, Q.-H. High-Resolution and High-Throughput Plasmonic Photopatterning of Complex Molecular Orientations in Liquid Crystals. *Adv. Mater.* **2016**, *28*, 2353–2358.
57. Price, F.P. Supercooling and Nucleation in Liquid Crystals AU - Armitage, D. *Mol. Cryst. Liq. Cryst.* **1978**, *44*, 33–44.
58. Brinkman, W.F.; Cladis, P.E. Defects in liquid crystals. *Phys. Today* **1982**, *35*, 48–54.
59. McConney, M.E.; Martinez, A.; Tondiglia, V.P.; Lee, K.M.; Langley, D.; Smalyukh, I.I.; White, T.J. Topography from Topology: Photoinduced Surface Features Generated in Liquid Crystal Polymer Networks. *Adv. Mater.* **2013**, *25*, 5880–5885.

60. Dierking, I. The Nematic and Cholesteric Phases. In *Textures of Liquid Crystals*; Wiley Online Books; **2004**; ISBN 9783527602056.
61. Dierking, I. The Fluid Smectic Phases. In *Textures of Liquid Crystals*; Wiley Online Books; **2004**; ISBN 9783527602056.
62. Dierking, I. Color Plates. In *Textures of Liquid Crystals*; Wiley Online Books; **2004**; ISBN 9783527602056.
63. Seddon, J.M. Characterization Methods: Structural Studies of Liquid Crystals by X-Ray Diffraction. In *Handbook of Liquid Crystals*; Wiley Online Books; **2008**; ISBN 9783527620760.
64. Nishiya, W.; Takanishi, Y.; Yamamoto, J.; Yoshizawa, A. Molecular design for a cybotactic nematic phase. *J. Mater. Chem. C* **2014**, 2, 3677–3685.
65. White, D.L.; Taylor, G.N. New absorptive mode reflective liquid-crystal display device. *J. Appl. Phys.* **1974**, 45, 4718–4723.
66. White, T.J.; Broer, D.J. Programmable and adaptive mechanics with liquid crystal polymer networks and elastomers. *Nat. Mater.* **2015**, 14, 1087.
67. Ohm, C.; Brehmer, M.; Zentel, R. Liquid Crystalline Elastomers as Actuators and Sensors. *Adv. Mater.* **2010**, 22, 3366–3387.
68. Küpfer, J.; Finkelmann, H. Nematic liquid single crystal elastomers. *Die Makromol. Chemie, Rapid Commun.* **1991**, 12, 717–726.
69. Broer, D.J.; Finkelmann, H.; Kondo, K. In-situ photopolymerization of an oriented liquid-crystalline acrylate. *Die Makromol. Chemie* **1988**, 189, 185–194.
70. Kularatne, R.S.; Kim, H.; Boothby, J.M.; Ware, T.H. Liquid crystal elastomer actuators: Synthesis, alignment, and applications. *J. Polym. Sci. Part B Polym. Phys.* **2017**, 55, 395–411.
71. de Haan, L.T.; Schenning, A.P.H.J.; Broer, D.J. Programmed morphing of liquid crystal networks. *Polymer (Guildf)*. **2014**, 55, 5885–5896.
72. Ambulo, C.P.; Burroughs, J.J.; Boothby, J.M.; Kim, H.; Shankar, M.R.; Ware, T.H. Four-dimensional Printing of Liquid Crystal Elastomers. *ACS*

73. López-Valdeolivas, M.; Liu, D.; Broer, D.J.; Sánchez-Somolinos, C. 4D Printed Actuators with Soft-Robotic Functions. *Macromol. Rapid Commun.* **2018**, *39*, 1700710.
74. Thomsen, D.L.; Keller, P.; Naciri, J.; Pink, R.; Jeon, H.; Shenoy, D.; Ratna, B.R. Liquid Crystal Elastomers with Mechanical Properties of a Muscle. *Macromolecules* **2001**, *34*, 5868–5875.
75. Fridrikh, S. V.; Terentjev, E.M. Polydomain-monodomain transition in nematic elastomers. *Phys. Rev. E* **1999**, *60*, 1847–1857.
76. Broer, D.J.; Mol, G.N.; Challa, G. In situ photopolymerization of an oriented liquid-crystalline acrylate, 2. *Die Makromol. Chemie* **1989**, *190*, 19–30.
77. Yakacki, C.M.; Saed, M.; Nair, D.P.; Gong, T.; Reed, S.M.; Bowman, C.N. Tailorable and programmable liquid-crystalline elastomers using a two-stage thiol–acrylate reaction. *RSC Adv.* **2015**, *5*, 18997–19001.
78. Ware, T.H.; Perry, Z.P.; Middleton, C.M.; Iacono, S.T.; White, T.J. Programmable Liquid Crystal Elastomers Prepared by Thiol–Ene Photopolymerization. *ACS Macro Lett.* **2015**, *4*, 942–946.
79. Ware, T.H.; McConney, M.E.; Wie, J.J.; Tondiglia, V.P.; White, T.J. Voxelated liquid crystal elastomers. *Science (80-.)*. **2015**, *347*, 982 LP-984.
80. Yu, Y.; Nakano, M.; Ikeda, T. Directed bending of a polymer film by light. *Nature* **2003**, *425*, 145.
81. Harris, K.D.; Bastiaansen, C.W.M.; Lub, J.; Broer, D.J. Self-Assembled Polymer Films for Controlled Agent-Driven Motion. *Nano Lett.* **2005**, *5*, 1857–1860.
82. de Gennes, P.G. Reflexions sur un type de polymeres nematiques. *Comptes Rendus l'Academie des Sci. - Ser. B* **1975**, *281*, 101–103.
83. Ahir, S.V.; Tajbakhsh, A.R.; Terentjev, E.M. Self-Assembled Shape-Memory Fibers of Triblock Liquid-Crystal Polymers. *Adv. Funct. Mater.* **2006**, *16*, 556–560.

84. Mol, G.N.; Harris, K.D.; Bastiaansen, C.W.M.; Broer, D.J. Thermo-Mechanical Responses of Liquid-Crystal Networks with a Splayed Molecular Organization. *Adv. Funct. Mater.* **2005**, *15*, 1155–1159.
85. Broer, D.J.; Mol, G.N. Anisotropic thermal expansion of densely cross-linked oriented polymer networks. *Polym. Eng. Sci.* **1991**, *31*, 625–631.
86. Kondo, M.; Sugimoto, M.; Yamada, M.; Naka, Y.; Mamiya, J.; Kinoshita, M.; Shishido, A.; Yu, Y.; Ikeda, T. Effect of concentration of photoactive chromophores on photomechanical properties of crosslinked azobenzene liquid-crystalline polymers. *J. Mater. Chem.* **2010**, *20*, 117–122.
87. Lee, K.M.; Koerner, H.; Vaia, R.A.; Bunning, T.J.; White, T.J. Relationship between the Photomechanical Response and the Thermomechanical Properties of Azobenzene Liquid Crystalline Polymer Networks. *Macromolecules* **2010**, *43*, 8185–8190.
88. Bushuyev, O.S.; Barrett, C.J. Photochromism in the Solid State. In *Photomechanical Materials, Composites, and Systems*; Wiley Online Books; **2017**; ISBN 9781119123279.
89. Elias, A.L.; Harris, K.D.; Bastiaansen, C.W.M.; Broer, D.J.; Brett, M.J. Photopatterned liquid crystalline polymers for microactuators. *J. Mater. Chem.* **2006**, *16*, 2903–2912.
90. Hikmet, R.A.M.; Broer, D.J. Dynamic mechanical properties of anisotropic networks formed by liquid crystalline acrylates. *Polymer (Guildf)*. **1991**, *32*, 1627–1632.
91. Kowalski, B.A.; Guin, T.C.; Auguste, A.D.; Godman, N.P.; White, T.J. Pixelated Polymers: Directed Self Assembly of Liquid Crystalline Polymer Networks. *ACS Macro Lett.* **2017**, *6*, 436–441.
92. Yang, R.; Zhao, Y. Non-Uniform Optical Inscription of Actuation Domains in a Liquid Crystal Polymer of Uniaxial Orientation: An Approach to Complex and Programmable Shape Changes. *Angew. Chemie Int. Ed.* **2017**, *56*, 14202–14206.
93. Sawa, Y.; Ye, F.; Urayama, K.; Takigawa, T.; Gimenez-Pinto, V.; Selinger, R.L.B.; Selinger, J. V Shape selection of twist-nematic-elastomer ribbons. *Proc. Natl. Acad. Sci.* **2011**, *108*, 6364 LP-6368.

94. Iamsaard, S.; Abhoff, S.J.; Matt, B.; Kudernac, T.; Cornelissen, J.J.L.M.; Fletcher, S.P.; Katsonis, N. Conversion of light into macroscopic helical motion. *Nat. Chem.* **2014**, *6*, 229.
95. D., M.C.; K., B.; M., W. Gaussian curvature from flat elastica sheets. *Proc. R. Soc. A Math. Phys. Eng. Sci.* **2011**, *467*, 1121–1140.
96. de Haan, L.T.; Sánchez-Somolinos, C.; Bastiaansen, C.M.W.; Schenning, A.P.H.J.; Broer, D.J. Engineering of Complex Order and the Macroscopic Deformation of Liquid Crystal Polymer Networks. *Angew. Chemie Int. Ed.* **2012**, *51*, 12469–12472.
97. Xia, Y.; Cedillo-Servin, G.; Kamien, R.D.; Yang, S. Guided Folding of Nematic Liquid Crystal Elastomer Sheets into 3D via Patterned 1D Microchannels. *Adv. Mater.* **2016**, *28*, 9637–9643.
98. de Haan, L.T.; Gimenez-Pinto, V.; Konya, A.; Nguyen, T.-S.; Verjans, J.M.N.; Sánchez-Somolinos, C.; Selinger, J. V; Selinger, R.L.B.; Broer, D.J.; Schenning, A.P.H.J. Accordion-like Actuators of Multiple 3D Patterned Liquid Crystal Polymer Films. *Adv. Funct. Mater.* **2014**, *24*, 1251–1258.
99. D., M.C.; M., W.; C., S.-S.; T., de H.L.; D., B. Angular deficits in flat space: remotely controllable apertures in nematic solid sheets. *Proc. R. Soc. A Math. Phys. Eng. Sci.* **2013**, *469*, 20120631.
100. White, T.J. Photomechanical effects in liquid crystalline polymer networks and elastomers. *J. Polym. Sci. Part B Polym. Phys.* **2018**, *56*, 695–705.
101. Merino, E.; Ribagorda, M. Control over molecular motion using the cis-trans photoisomerization of the azo group. *Beilstein J. Org. Chem.* **2012**, *8*, 1071–1090.
102. Bandara, H.M.D.; Burdette, S.C. Photoisomerization in different classes of azobenzene. *Chem. Soc. Rev.* **2012**, *41*, 1809–1825.
103. Mahimwalla, Z.; Yager, K.G.; Mamiya, J.; Shishido, A.; Priimagi, A.; Barrett, C.J. Azobenzene photomechanics: prospects and potential applications. *Polym. Bull.* **2012**, *69*, 967–1006.
104. Yager, K.G.; Barrett, C.J. Novel photo-switching using azobenzene functional materials. *J. Photochem. Photobiol. A Chem.* **2006**, *182*, 250–261.

105. Whitten, D.G.; Wildes, P.D.; Pacifici, J.G.; Irick, G. Solvent and substituent on the thermal isomerization of substituted azobenzenes. Flash spectroscopic study. *J. Am. Chem. Soc.* **1971**, *93*, 2004–2008.
106. Liu, D.; Broer, D.J. New insights into photoactivated volume generation boost surface morphing in liquid crystal coatings. *Nat. Commun.* **2015**, *6*, 8334.
107. Lahikainen, M.; Zeng, H.; Priimagi, A. Reconfigurable photoactuator through synergistic use of photochemical and photothermal effects. *Nat. Commun.* **2018**, *9*, 4148.
108. Gelebart, A.H.; Vantomme, G.; Meijer, E.W.; Broer, D.J. Mastering the Photothermal Effect in Liquid Crystal Networks: A General Approach for Self-Sustained Mechanical Oscillators. *Adv. Mater.* **2017**, *29*, 1606712.
109. Matějka, L.; Dušek, K.; Ilavský, M. The thermal effect in the photomechanical conversion of a photochromic polymer. *Polym. Bull.* **1979**, *1*, 659–664.
110. Yamada, M.; Kondo, M.; Mamiya, J.; Yu, Y.; Kinoshita, M.; Barrett, C.J.; Ikeda, T. Photomobile Polymer Materials: Towards Light-Driven Plastic Motors. *Angew. Chemie Int. Ed.* **2008**, *47*, 4986–4988.
111. Yamada, M.; Kondo, M.; Miyasato, R.; Naka, Y.; Mamiya, J.; Kinoshita, M.; Shishido, A.; Yu, Y.; Barrett, C.J.; Ikeda, T. Photomobile polymer materials—various three-dimensional movements. *J. Mater. Chem.* **2009**, *19*, 60–62.
112. White, T.J.; Tabiryan, N. V; Serak, S. V; Hrozhyk, U.A.; Tondiglia, V.P.; Koerner, H.; Vaia, R.A.; Bunning, T.J. A high frequency photodriven polymer oscillator. *Soft Matter* **2008**, *4*, 1796–1798.
113. Cheng, F.; Yin, R.; Zhang, Y.; Yen, C.-C.; Yu, Y. Fully plastic microrobots which manipulate objects using only visible light. *Soft Matter* **2010**, *6*, 3447–3449.
114. Ahn, S.; Ware, T.H.; Lee, K.M.; Tondiglia, V.P.; White, T.J. Photoinduced Topographical Feature Development in Blueprinted Azobenzene-Functionalized Liquid Crystalline Elastomers. *Adv. Funct. Mater.* **2016**, *26*, 5819–5826.

115. Wu, W.; Yao, L.; Yang, T.; Yin, R.; Li, F.; Yu, Y. NIR-Light-Induced Deformation of Cross-Linked Liquid-Crystal Polymers Using Upconversion Nanophosphors. *J. Am. Chem. Soc.* **2011**, *133*, 15810–15813.
116. Donovan, B.R.; Matavulj, V.M.; Ahn, S.; Guin, T.; White, T.J. All-Optical Control of Shape. *Adv. Mater.* **2019**, *31*, 1805750.
117. Iamsaard, S.; Anger, E.; Aßhoff, S.J.; Depauw, A.; Fletcher, S.P.; Katsonis, N. Fluorinated Azobenzenes for Shape-Persistent Liquid Crystal Polymer Networks. *Angew. Chemie Int. Ed.* **2016**, *55*, 9908–9912.
118. Wie, J.J.; Shankar, M.R.; White, T.J. Photomotility of polymers. *Nat. Commun.* **2016**, *7*, 13260.
119. Gelebart, A.H.; Jan Mulder, D.; Varga, M.; Konya, A.; Vantomme, G.; Meijer, E.W.; Selinger, R.L.B.; Broer, D.J. Making waves in a photoactive polymer film. *Nature* **2017**, *546*, 632.
120. Liu, D.; Liu, L.; Onck, P.R.; Broer, D.J. Reverse switching of surface roughness in a self-organized polydomain liquid crystal coating. *Proc. Natl. Acad. Sci.* **2015**, *112*, 3880 LP-3885.
121. Liu, D.; Bastiaansen, C.W.M.; den Toonder, J.M.J.; Broer, D.J. Photo-Switchable Surface Topologies in Chiral Nematic Coatings. *Angew. Chemie Int. Ed.* **2012**, *51*, 892–896.
122. Liu, D.; Bastiaansen, C.W.M.; den Toonder, J.M.J.; Broer, D.J. Light-Induced Formation of Dynamic and Permanent Surface Topologies in Chiral–Nematic Polymer Networks. *Macromolecules* **2012**, *45*, 8005–8012.
123. Hendrikx, M.; Sirma, B.; Schenning, A.P.H.J.; Liu, D.; Broer, D.J. Compliance-Mediated Topographic Oscillation of Polarized Light Triggered Liquid Crystal Coating. *Adv. Mater. Interfaces* **2018**, *5*, 1800810.
124. Blaiszik, B.J.; Kramer, S.L.B.; Olugebefola, S.C.; Moore, J.S.; Sottos, N.R.; White, S.R. Self-Healing Polymers and Composites. *Annu. Rev. Mater. Res.* **2010**, *40*, 179–211.
125. Zhao, Y.; Xie, Z.; Gu, H.; Zhu, C.; Gu, Z. Bio-inspired variable structural color materials. *Chem. Soc. Rev.* **2012**, *41*, 3297–3317.

126. Mano, J.F. Stimuli-Responsive Polymeric Systems for Biomedical Applications. *Adv. Eng. Mater.* **2008**, *10*, 515–527.
127. Mohammed, J.S.; Murphy, W.L. Bioinspired Design of Dynamic Materials. *Adv. Mater.* **2009**, *21*, 2361–2374.
128. Merindol, R.; Walther, A. Materials learning from life: concepts for active, adaptive and autonomous molecular systems. *Chem. Soc. Rev.* **2017**, *46*, 5588–5619.
129. Kim, S.; Laschi, C.; Trimmer, B. Soft robotics: a bioinspired evolution in robotics. *Trends Biotechnol.* **2013**, *31*, 287–294.
130. Klute, G.K.; Czerniecki, J.M.; Hannaford, B. Artificial Muscles: Actuators for Biorobotic Systems. *Int. J. Rob. Res.* **2002**, *21*, 295–309.
131. Snell, R.S.; Lemp, M.A. Movements of the Eyeball and the Extraocular Muscles. In *Clinical Anatomy of the Eye*; Wiley Online Books; **1997**; ISBN 9781118690987.
132. Lentink, D.; Müller, U.K.; Stamhuis, E.J.; de Kat, R.; van Gestel, W.; Veldhuis, L.L.M.; Henningsson, P.; Hedenström, A.; Videler, J.J.; van Leeuwen, J.L. How swifts control their glide performance with morphing wings. *Nature* **2007**, *446*, 1082.
133. Obringer, L. Hyperelastic Research/Lightweight Flexible Aircraft Available online: <https://www.nasa.gov/feature/hyperelastic-researchlightweight-flexible-aircraft> (accessed on Jan 30, 2019).
134. Katzschnmann, R.K.; DelPreto, J.; MacCurdy, R.; Rus, D. Exploration of underwater life with an acoustically controlled soft robotic fish. *Sci. Robot.* **2018**, *3*, eaar3449.
135. Li, S.; Wang, K.W. Plant-inspired adaptive structures and materials for morphing and actuation: a review. *Bioinspir. Biomim.* **2016**, *12*, 11001.
136. E., R.; L., M. Hygromorphs: from pine cones to biomimetic bilayers. *J. R. Soc. Interface* **2009**, *6*, 951–957.
137. Forterre, Y.; Skotheim, J.M.; Dumais, J.; Mahadevan, L. How the Venus flytrap snaps. *Nature* **2005**, *433*, 421.

138. van Meeteren, U.; van Doorn, W.G. Flower opening and closure: a review. *J. Exp. Bot.* **2003**, *54*, 1801–1812.
139. Roelfsema, M.R.G.; Hedrich, R. Studying guard cells in the intact plant: modulation of stomatal movement by apoplastic factors. *New Phytol.* **2002**, *153*, 425–431.
140. Noblin, X.; Rojas, N.O.; Westbrook, J.; Llorens, C.; Argentina, M.; Dumais, J. The Fern Sporangium: A Unique Catapult. *Science (80-.).* **2012**, *335*, 1322 LP-1322.
141. van Oosten, C.L.; Bastiaansen, C.W.M.; Broer, D.J. Printed artificial cilia from liquid-crystal network actuators modularly driven by light. *Nat. Mater.* **2009**, *8*, 677.
142. Li, C.; Liu, Y.; Huang, X.; Jiang, H. Direct Sun-Driven Artificial Heliotropism for Solar Energy Harvesting Based on a Photo-Thermomechanical Liquid-Crystal Elastomer Nanocomposite. *Adv. Funct. Mater.* **2012**, *22*, 5166–5174.
143. Shankar, M.R.; Smith, M.L.; Tondiglia, V.P.; Lee, K.M.; McConney, M.E.; Wang, D.H.; Tan, L.-S.; White, T.J. Contactless, photoinitiated snap-through in azobenzene-functionalized polymers. *Proc. Natl. Acad. Sci.* **2013**, *110*, 18792 LP-18797.
144. Kohlmeyer, R.R.; Chen, J. Wavelength-Selective, IR Light-Driven Hinges Based on Liquid Crystalline Elastomer Composites. *Angew. Chemie Int. Ed.* **2013**, *52*, 9234–9237.
145. Zeng, H.; Wasylczyk, P.; Parmeggiani, C.; Martella, D.; Burrese, M.; Wiersma, D.S. Light-Fueled Microscopic Walkers. *Adv. Mater.* **2015**, *27*, 3883–3887.
146. Rogóż, M.; Zeng, H.; Xuan, C.; Wiersma, D.S.; Wasylczyk, P. Light-Driven Soft Robot Mimics Caterpillar Locomotion in Natural Scale. *Adv. Opt. Mater.* **2016**, *4*, 1689–1694.
147. Palagi, S.; Mark, A.G.; Reigh, S.Y.; Melde, K.; Qiu, T.; Zeng, H.; Parmeggiani, C.; Martella, D.; Sanchez-Castillo, A.; Kapernaum, N.; et al. Structured light enables biomimetic swimming and versatile locomotion of photoresponsive soft microrobots. *Nat. Mater.* **2016**, *15*, 647.

148. ABhoff, S.J.; Lancia, F.; Iamsaard, S.; Matt, B.; Kudernac, T.; Fletcher, S.P.; Katsonis, N. High-Power Actuation from Molecular Photoswitches in Enantiomerically Paired Soft Springs. *Angew. Chemie Int. Ed.* **2017**, *56*, 3261–3265.
149. Kizilkan, E.; Strueben, J.; Staubitz, A.; Gorb, S.N. Bioinspired photocontrollable microstructured transport device. *Sci. Robot.* **2017**, *2*, eaak9454.
150. Zeng, H.; Wani, O.M.; Wasylczyk, P.; Priimagi, A. Light-Driven, Caterpillar-Inspired Miniature Inching Robot. *Macromol. Rapid Commun.* **2018**, *39*, 1700224.
151. Sol, J.A.H.P.; Peeketi, A.R.; Vyas, N.; Schenning, A.P.H.J.; Annabattula, R.K.; Debije, M.G. Butterfly proboscis-inspired tight rolling tapered soft actuators. *Chem. Commun.* **2019**.

PUBLICATIONS

- Publication I Wani, O.M.; Zeng, H.; Wasylczyk, P.; Priimagi, A. Programming Photoresponse in Liquid Crystal Polymer Actuators with Laser Projector. *Adv. Opt. Mater.* **2018**, 6, 1700949.
- Publication II Zeng, H.; Wani, O.M.; Wasylczyk, P.; Kaczmarek, R.; Priimagi, A. Self-Regulating Iris Based on Light-Actuated Liquid Crystal Elastomer. *Adv. Mater.* **2017**, 29, 1701814.
- Publication III Wani, O.M.; Zeng, H.; Priimagi, A. A light-driven artificial flytrap. *Nat. Commun.* **2017**, 8, 15546.
- Publication IV Wani, O.M.; Verpaalen, R.; Zeng, H.; Priimagi, A.; Schenning, A.P.H.J. An Artificial Nocturnal Flower via Humidity-Gated Photoactuation in Liquid Crystal Networks. *Adv. Mater.* **2019**, 31, 1805985.

PUBLICATION I

Programming photoresponse in liquid crystal polymer actuators with laser projector

Owies M. Wani, Hao Zeng, Piotr Wasylczyk, and Arri Priimagi

Advanced Optical Materials, vol. 6, no. 1, p. 1700949, 2017. Available:
[10.1002/adom.201700949](https://doi.org/10.1002/adom.201700949)

Publication reprinted with the permission of the copyright holders.

Programming Photoresponse in Liquid Crystal Polymer Actuators with Laser Projector

Owies M. Wani, Hao Zeng,* Piotr Wasylczyk, and Arri Priimagi*

A versatile, laser-projector-based method is demonstrated for programming alignment patterns into monolithic films of liquid crystal polymer networks. Complex images can be photopatterned into the polymer films with sub-100 μm resolution, using relatively short exposure times. The method is further used to devise both photochemically and photothermally driven actuators that can undergo distinct light-induced shape changes, dictated by the programmed alignment patterns. Deformation modes such as buckling and coiling, as well as miniature robotic devices such as a gripper and a light-responsive octopod, are demonstrated. The reported technique enables easy and cost-effective programmable actuation with relatively high throughput, thus significantly facilitating the design and realization of functional soft robotic actuators.

1. Introduction

Smart materials that can change their properties in response to external conditions are at the forefront of contemporary materials research.^[1–3] Stimuli-responsive soft actuators represent an important subclass among such materials.^[4–6] Potential applications of the soft actuators include artificial muscles,^[7] tissue engineering,^[8] biotechnologies,^[9] microrobotics,^[10] microoptics,^[11] etc. The key to building up a functional microsystem based on soft actuators is to program the material to achieve multiple desired deformations. Programming soft actuators, however, is challenging as they lack individual control circuitry (often adopted in conventional electronic actuators), restricted by their miniature sizes. Hence, programmable soft materials that can exhibit multiple deformations and thus perform a variety of tasks, are in great demand.

Liquid crystal polymer networks (LCNs; note that we use this term to describe both elastomeric and glassy polymer networks)


have emerged as promising materials for fabricating soft actuators.^[12–14] LCNs combine the anisotropy of the constituent liquid-crystal (LC) molecules and the elasticity of polymer networks, and are capable of stimuli-responsive shape change at the macroscopic scale. LCNs can be actuated by various stimuli such as light,^[15] heat,^[16] solvent,^[17] and humidity.^[18] Being a clean, remote, and precisely controllable stimulus, light is a particularly attractive energy source.^[19] The light-triggered deformation of an LCN actuator is governed by the alignment distribution of the constituent liquid-crystal molecules within the polymer network, and developing methods for precise control over the director distribution in order to obtain desired photoactuation mode is an important topic of research.^[14,20–22]

Photoalignment has proven to be a successful technique in patterning complex alignments into liquid-crystalline materials^[23–25] and in devising on-demand actuations into LCNs.^[21] The technique is based on illuminating a thin photoresponsive layer, a “command surface,”^[26] with linearly polarized light. Upon illumination, the photoalignment layer becomes anisotropic, thereby changing the boundary conditions experienced by the liquid-crystal molecules in the vicinity, and forcing them to align either perpendicular^[27] or parallel^[28] to the light polarization. Photopatterning of director orientation can be achieved by spatially modulating the light polarization,^[27] or exposure through mask(s).^[28,29] White and co-workers have used a laser setup to raster scan a focussed laser beam with controlled polarization across the sample, and thus achieved local control in the director distribution.^[30–32] Also spatial light modulators and digital micromirror devices have been used for high-throughput patterning.^[17,33–35] These demonstrations require either prepatterned masks or relatively complex optical set-ups for programming the desired director distribution.

Herein, we use a laser projector with a microelectromechanical system (MEMS)-based scanning mirror assembly (PICO, Sony) to program the liquid-crystal alignment within a monolithic LCN film. Photopatterning is achieved by projecting an arbitrary computer-generated image onto the photoalignment layer, using predefined light polarization. The projector is capable of addressing a minimum feature size of 50 μm over an area of $25 \times 14 \text{ mm}^2$. A series of complex photoactuators, such as defect buckling, coiling strip with gradient in pitch, four-arm gripper, and bidirectional bending in an octopod, are demonstrated by engineering different director orientations via photopatterning. The photoactuators are fabricated by polymerizing LC monomer mixtures inside LC cells that have been

O. M. Wani, Dr. H. Zeng, Prof. A. Priimagi
Laboratory of Chemistry and Bioengineering
Tampere University of Technology
P.O. Box 541, FI 33101 Tampere, Finland
E-mail: hao.zeng@tut.fi; arri.priimagi@tut.fi

Dr. P. Wasylczyk
Photonic Nanostructure Facility
Institute of Experimental Physics
Faculty of Physics
University of Warsaw
ul. Pasteura 5, 02-093 Warsaw, Poland

 The ORCID identification number(s) for the author(s) of this article can be found under <https://doi.org/10.1002/adom.201700949>.

DOI: 10.1002/adom.201700949

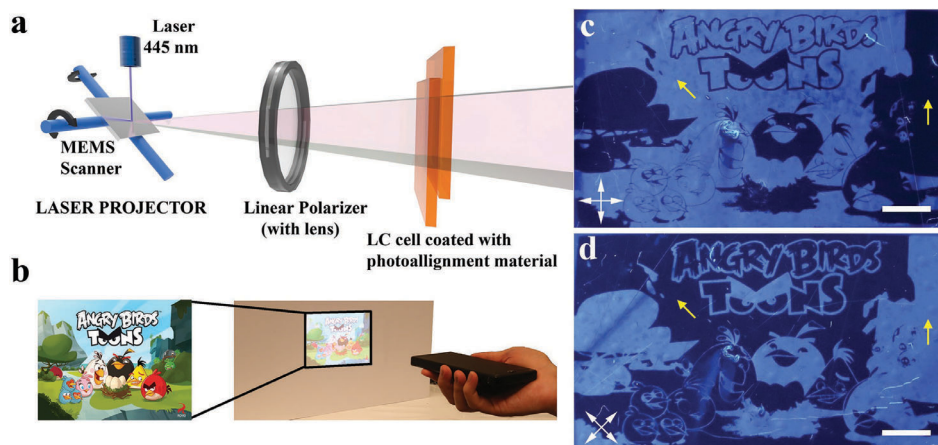


Figure 1. a) Working principle of the photoalignment set-up with the single-mirror MEMS laser projector. b) Projection of a colored image by the miniature laser projector. c,d) Polarized microscope images of photopatterned samples. Crossed double-headed arrows represent the polarizer and analyser directions, yellow arrows indicate the local LC alignment orientation. Scale bars: 3 mm. Image in (b) used with permission from Rovio Entertainment Ltd.

fabricated using the photoalignment-patterned glass substrates, opening the LC cells, and finally peeling off the polymerized films to yield free-standing actuators.

2. Results and Discussion

The working principle of the laser projector is schematically illustrated in **Figure 1a**. The device contains three time-modulated laser diodes (red 650 nm, green 550 nm, and blue 445 nm) scanned with the MEMS single micromirror. By repetitive horizontal and vertical scanning, the device is able to project images with 1799×799 pixel resolution at 60 Hz.^[36] To match the absorption band of the photoalignment material (Brilliant Yellow, **8** in **Figure 3**),^[37] we only used the blue laser diode for photopatterning. Before illuminating the alignment layer, a rotating linear polarizer was used to control the light polarization direction (and thus the molecular alignment direction, which is in the plane of the sample and perpendicular to the light polarization), and a lens ($f = 30$ mm) projected the image onto the sample plane. The image shown in **Figure 1b** (from a Finnish video game franchise the Angry Birds, by Rovio Entertainment Ltd.) was projected onto a glass slide coated with the alignment layer (details in Experimental Section), followed by projection of its inverted (negative) image with 45° difference in the polarization direction. After photopatterning, a thin layer of LC monomer mixture, consisting of 99 wt% LC diacrylate **3**, and 1 wt% of photoinitiator **7**, was spin-coated and polymerized on the slide for the alignment visualization (see **Figure 3** for chemical structures). **Figure 1c,d** shows the crosspolarized images, where the sample is placed at 0° and 45° angle with respect to the polarizers, respectively, illustrating that the image can be successfully patterned onto the LCN film.

Figure 2a shows the minimum line widths of patterned structures, which are ≈ 50 μm in the horizontal and ≈ 75 μm in

the vertical direction. The difference is due to the lateral scanning direction of the micromirror. To determine the minimum pixel size of 2D patterning, we projected checkerboard patterns of different size onto the sample and obtained a minimum period of 100×100 μm^2 (**Figure 2b**). To assess the time needed for efficient photoalignment, we measured the evolution of the dichroic ratio of molecule **6**, doped in the visualization layer (see previous paragraph), as a function of time (**Figure S1**, Supporting Information). As can be seen in **Figure 2d**, the dichroic ratio saturates after 5 min exposure, indicating that 5 min suffices to inscribe one image. The light intensity on the sample plane being 3.0 mW cm^{-2} , this corresponds to the absorbed energy below 1 J cm^{-2} .

To demonstrate the utility of the photoalignment patterns in devising macroscopic LCN photoactuators, we used two polymerizable mixtures (**A** and **B**; see **Figure 3** for the chemical structures). Mixture **A** contained 53 mol% of monomer **1**, 18 mol% of monomer **2**, 21 mol% of crosslinker **4**, 7 mol% of azobenzene crosslinker **5**, and 1 mol% of photoinitiator **7**. Mixture **B** consisted of 77 mol% of monomer **1**, 20 mol% of crosslinker **3**, 2 mol% of azobenzene dopant **6**, and 1 mol% of photoinitiator **7**. UV-vis absorption spectra of the azobenzene molecules **5** and **6** are given in **Figure S2** of the Supporting Information. Mixture **A** undergoes photoactuation via photochemical, *trans-cis* isomerization-driven, mechanism,^[38] while in mixture **B** the actuation is driven by photothermal effects.^[27] The difference in the actuation mechanisms results from (i) the fact that mixture **A** contains azobenzene crosslinks while the azobenzenes are simply doped into mixture **B**, and (ii) the different lifetimes of the *cis*-isomers of **5** and **6**, which are in the order of hours and seconds, respectively. The long *cis*-lifetime of **5** preserves the deformed structure even after turning off the light, while it can return to the original shape by absorbing another wavelength or via thermal relaxation in relatively long time.^[39] In **6**, short *cis*-lifetime/fast thermal relaxation

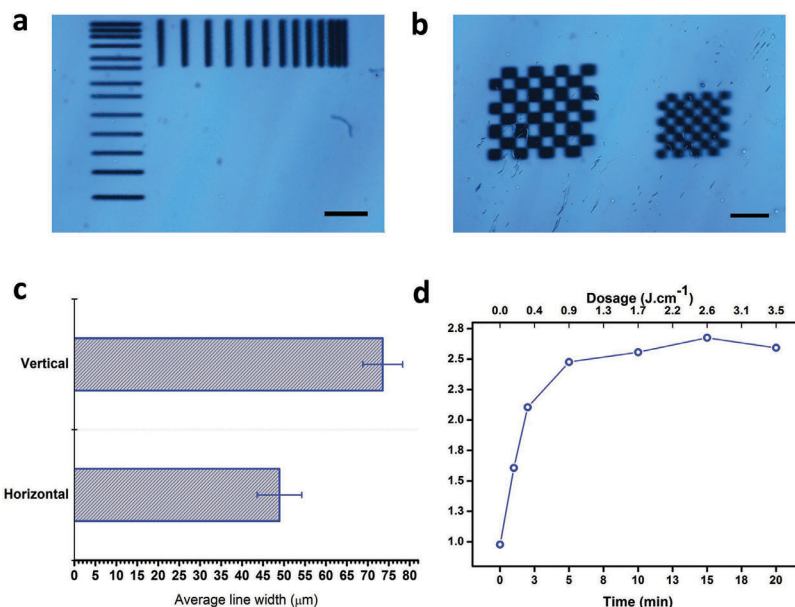


Figure 2. a) Polarized optical images of lines patterned in the horizontal and vertical directions. b) Polarized optical image of checkerboard patterns showing the minimum pixel size while maintaining high resolution and contrast. c) Minimum line widths that can be patterned in the vertical and horizontal directions (error bars indicate standard deviation for 10 independent measurements). d) Dichroic ratio versus time/light dose during incident on the sample during the patterning illumination. Scale bars in (a) and (b) correspond to 500 μm.

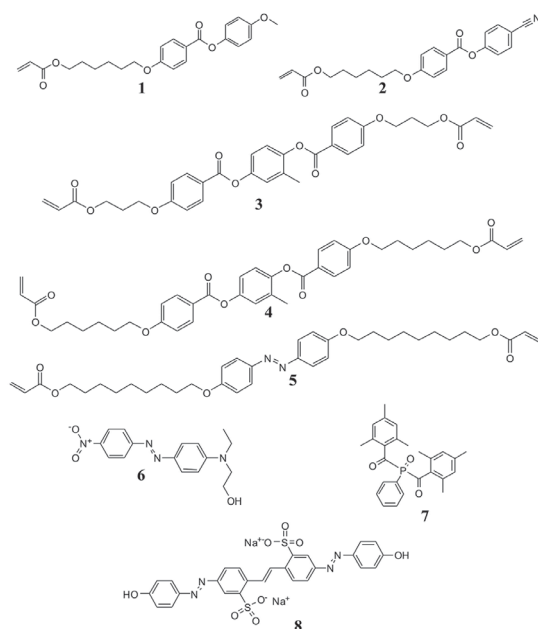


Figure 3. Chemical structures of the compounds used in this work.

enable continuous *trans*–*cis*–*trans* cycling upon illumination, thus efficiently transferring the photon energy into heat.^[40] In azobenzene-based actuators, these two mechanisms cannot be completely decoupled, yet dominance of one mechanism over the other can lead to very distinct actuation behavior. For example, shape-persistent actuators based on *trans*–*cis* isomerization of fluorinated azobenzene crosslinkers yield bistable actuators,^[41] while photothermal actuators are the preferred approach when developing high-frequency, light-driven photo-mechanical oscillators^[42] and miniature robots.^[15,40]

Both mixtures **A** and **B** are adaptable to photoalignment with the laser projector, and we applied four kinds of alignment patterns to demonstrate different actuation possibilities. All the actuators are of 50 μm thickness, unless otherwise stated. Mixture **A** was used to fabricate films with alignment patterns shown in **Figure 4a,e**. The pattern in **Figure 4a** corresponds to a +1 topological defect in the LC orientation,^[43] where molecules in the bulk of the film are aligned in the planar square geometry. Such alignment results in cone/anticone buckling deformation upon illumination with UV light (385 nm, 130 mW cm⁻², exposure time 1.5 min), while the initial shape is recovered upon exposure to visible light (460 nm, 150 mW cm⁻², 1 min), as illustrated in **Figure 4b–d** (see also Video S1 in the Supporting information). The conical initial shape of the film, seen in **Figure 4b**, can be explained by residual stress generated in the LCN film during photopolymerization.^[44–46] **Figure 4e** represents an LCN strip with end-to-end gradient in director orientation on one side of the

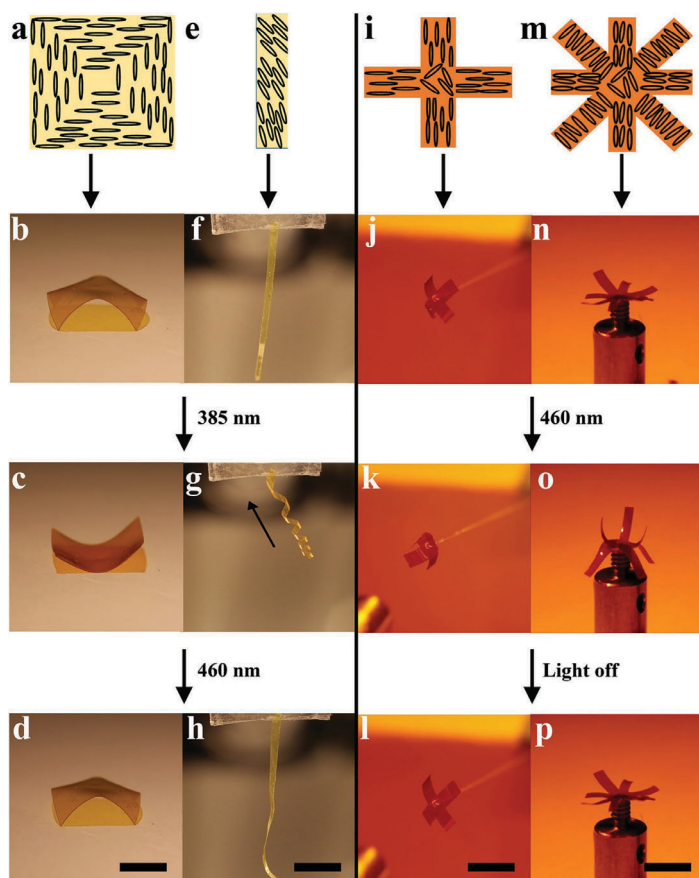


Figure 4. Molecular orientation and actuation via photochemical mechanism of a–d) a film with +1 topological defect; e–h) a film strip with modified director angles from one end to the other. Photothermally actuated i–l) 4-armed gripper and m–p) 8-legged structure. All scale bars correspond to 6 mm.

film, i.e., the director angle gradually varies from 45° on one end to 15° on the other end, with respect to the stripe direction. On the other side of the film, the molecules are aligned homeotropically. Upon actuation with UV light (385 nm, 130 mW cm^{-2} , 1 min), the strip deforms into a coil with the pitch tapered along the body length: large pitch on the 45° -orientated end and small one at the 15° end, thus showing the possibility of programming a pitch gradient into a monolithic coiling strip.^[38,46] The strip uncoils upon visible light irradiation (460 nm, 150 mW cm^{-2} , 1 min). The coiling/uncoiling is illustrated in Figure 4f–h, and Video S2 of the Supporting Information.

Mixture B was used to fabricate films with alignment patterns shown in Figure 4i,m. The pattern in Figure 4i defines a splay-aligned gripper structure, where one surface has planar boundary conditions directed along each arm, and the other surface has homeotropic anchoring. Figure 4j–l shows the photothermal actuation of thus patterned actuator upon

460 nm illumination (150 mW cm^{-2} , 1.5 s), where the four arms bend toward the center of the structure, performing a closing/gripping actuation. As soon as the light is turned off, the arms return to their initial shape (Video S3, Supporting Information). The final structure to demonstrate is an 8-legged octopod, schematically shown in Figure 4m. Each leg has a 90° twisted nematic alignment across the sample thickness, while adjacent legs have alternated director alignment orientations. Molecular orientation on the other surface is perpendicular to the one shown in Figure 4m. Upon illumination with 460 nm light (150 mW cm^{-2} , 4 s), the adjacent legs bend into opposite directions, dictated by the alternating director alignment (Figure 4n–p; Video S4, Supporting Information). Such structure acts as a starting point for the fabrication of monolithic LCN octopods, and ultimately lead to light-controlled robots capable of walking locomotion.

3. Conclusions

We have demonstrated a facile method based on a portable laser projector to program alignment patterns into monolithic films of liquid crystal polymer networks using photoalignment layers. Single mirror MEMS laser projector is capable of patterning molecular orientation into the polymer networks with the minimum feature size of $50 \mu\text{m}$ over an area of $25 \times 14 \text{ mm}^2$. Four types of alignment patterns were inscribed to yield polymeric actuators with versatile light-driven deformations using both photochemical and photo-thermal mechanisms. We believe this work to widen the scope of shape-programmable liquid crystal polymer actuators, in particular enabling efficient and easy fabrication of smart microdevices and microrobots.

4. Experimental Section

Preparation of the Angry Birds Pattern: A precleaned glass slide (sonication in acetone and isopropyl alcohol for 20 min each, UV ozone treatment for 20 min) was spin coated with 0.5 wt% solution of Brilliant yellow (Sigma) in dimethylformamide (DMF) (1500 rpm, 1 min), followed by baking at 90°C on a hot plate for 15–20 min. After that, the sample was fixed in a holder placed in front of projector (Sony MP-CL1A mobile projector) and exposed to the projected Angry Birds images (original and inverted) one after the other, 5 min each. Polarization difference of 45° was imparted between the original and inverted images. The photoalignment-patterned surface was then spin coated (2000 rpm; 500 rpm s^{-1} ; 1 min) with a LC mixture consisting of 99 wt% LC diacrylate monomer 1,4-bis-[4-(3-acryloyloxypropyloxy)benzoyloxy]-2-methylbenzene **3** (Synthon chemicals) and 1 wt% photoinitiator bis(2,4,6-trimethylbenzoyl)-phenylphosphineoxide (Sigma Aldrich) dissolved in chloroform (4 wt%

solids). The spin coated layer was liquid crystalline at room temperature and was immediately polymerized under N₂ atmosphere using UV 375 nm LED (Thorlabs, 40 mW cm⁻²). Finally, the sample was analyzed between two polarizers and optical images were recorded.

Resolution and Time Required for Patterning: For resolution studies, lines and checkerboards were projected onto a sample prepared in the same way as described above. For exposure time studies, substrates coated with the alignment layer were subjected to linearly polarized light from the projector for irradiation times of 0, 1, 2, 5, 10, 15, and 20 min. After photopatterning, the substrates were spin coated with a monomer mixture solution containing 97 wt% of the LC diacrylate **3**, 2 wt% of Disperse red 1 (Sigma Aldrich), and 1 wt% of the UV photoinitiator, dissolved in chloroform (4 wt% solids). The spin-coated layer was polymerized under N₂ atmosphere using 375 nm LED (40 mW cm⁻²). Finally, polarized UV-vis absorption spectra were measured and are shown in Figure S1 of the Supporting Information. Dichroic ratio of Disperse Red 1 molecule is calculated by using the formula

$$D = \frac{A_{\parallel}}{A_{\perp}} \quad (1)$$

where A_{\parallel} is the absorbance in the direction parallel to director axis, and A_{\perp} is the absorbance perpendicular to the director axis.

Preprogramming Actuation: The photoalignment layers were prepared in the way described above, after which two photoalignment-coated substrates were made into an LC cell for photopatterning planar LCN films using 50 µm microspheres as spacers. In case of splay-aligned films one of the glasses forming the LC cell was coated with homeotropic-aligning polyimide layer (JSR OPTMER, 3000 RPM, 1 min). The cell was then fixed on a holder placed in front of the projector, and patterning was carried out over an area of 25 × 14 mm². Computer-controlled images with different brightness distribution were projected on the sample area, while the polarization was controlled by manually rotating the linear polarizer placed in between sample and projector. A 30 mm plano-convex lens was attached to polarizer to enhance the image sharpness at the sample plane. In case of twisted alignment, two glasses were patterned separately and covered (spin-coated) with liquid crystal monomer layer (polymerized immediately after spin-coating). The glasses were then glued to form an LC cell matching those patterns on two sides. In all LC cells, 50 µm spacers were used, except the one with modified director angle (Figure 4e–h), where 10 µm spacers were used. Polymerization of both mixtures was done by first heating the mixtures above the clearing point (80 °C) and then subsequently, infiltrating them into LC cells on a hot plate, via capillary force. The cells were then brought to LC phase by cooling them to 55 °C (5 °C min⁻¹), using Linkam temperature-controlled stage. After that, mixture **A** was polymerized using 420 nm LED (70 mW cm⁻²) and mixture **B** with 375 nm LED (40 mW cm⁻²) for about 15 min each. Finally, cells were opened using a razor blade and the LCN films were cut into desired shapes. Normalized UV-vis spectra of the photoresponsive molecules present in mixtures **A** and **B** are given in Figure S2 of the Supporting Information. Actuation of the films was performed using unpolarized UV 385 nm (130 mW cm⁻²) and/or Visible 460 nm (150 mW cm⁻²) light from a multichannel LED (Prior Scientific).

Supporting Information

Supporting Information is available from the Wiley Online Library or from the author.

Acknowledgements

A.P. gratefully acknowledges the financial support of the European Research Council (Starting Grant project PHOTOTUNE; Agreement No. 679646). O.M.W. is thankful to the graduate school of Tampere

University of Technology (TUT), and H.Z. to the TUT postdoctoral fellowship program, for supporting this work.

Conflict of Interest

The authors declare no conflict of interest.

Keywords

azobenzene, laser projectors, liquid crystal, patterning, photoactuation, photoalignment

Received: September 5, 2017

Revised: September 25, 2017

Published online: December 4, 2017

- [1] M. A. C. Stuart, W. T. S. Huck, J. Genzer, M. Müller, C. Ober, M. Stamm, G. B. Sukhorukov, I. Szleifer, V. V. Tsukruk, M. Urban, F. Winnik, S. Zauscher, I. Luzinov, S. Minko, *Nat. Mater.* **2010**, 9, 101.
- [2] D. Roy, J. N. Cambre, B. S. Sumerlin, *Prog. Polym. Sci.* **2010**, 35, 278.
- [3] P. M. Mendes, A. J. Downard, A. Muscroft-Taylor, A. D. Abell, T. Takagi, M. Kameda, T. Shinbo, T. Kanamori, Y. Yoshimi, J. F. Stoddart, *Chem. Soc. Rev.* **2008**, 37, 2512.
- [4] L. Hines, K. Petersen, G. Z. Lum, M. Sitti, *Adv. Mater.* **2017**, 29, 1603483.
- [5] F. Ilievski, A. D. Mazzeo, R. F. Shepherd, X. Chen, G. M. Whitesides, *Angew. Chem., Int. Ed.* **2011**, 50, 1890.
- [6] O. M. Wani, H. Zeng, A. Priimagi, *Nat. Commun.* **2017**, 8, 15546.
- [7] T. Mirfakhrai, J. D. W. Madden, R. H. Baughman, *Mater. Today* **2007**, 10, 30.
- [8] F. Rosso, G. Marino, A. Giordano, M. Barbarisi, D. Parmeggiani, A. Barbarisi, *J. Cell. Physiol.* **2005**, 203, 465.
- [9] M. Sitti, H. Ceylan, W. Hu, J. Giltinan, M. Turan, S. Yim, E. Diller, *Proc. IEEE* **2015**, 103, 205.
- [10] M. Sitti, *Nature* **2009**, 458, 1121.
- [11] T. Hirai, T. Ogiwara, K. Fujii, T. Ueki, K. Kinoshita, M. Takasaki, *Adv. Mater.* **2009**, 21, 2886.
- [12] C. Ohm, M. Brehmer, R. Zentel, *Adv. Mater.* **2010**, 22, 3366.
- [13] G. Fernández, *Nat. Mater.* **2012**, 12, 12.
- [14] a) T. J. White, D. J. Broer, *Nat. Mater.* **2015**, 14, 1087; b) Q. Li, *Intelligent Stimuli-Responsive Materials: From Well-Defined Nanostructures to Applications*, John Wiley & Sons, Hoboken, NJ, **2013**; c) H. K. Bisoyi, Q. Li, *Chem. Rev.* **2016**, 116, 15089.
- [15] H. Zeng, O. M. Wani, P. Wasylczyk, A. Priimagi, *Macromol. Rapid Commun.* **2017**, <https://doi.org/10.1002/marc.201700224>.
- [16] G. N. Mol, K. D. Harris, C. W. M. Bastiaansen, D. J. Broer, *Adv. Funct. Mater.* **2005**, 15, 1155.
- [17] J. M. Boothby, T. H. Ware, *Soft Matter* **2017**, 13, 4349.
- [18] M. Dai, O. T. Picot, J. M. N. Verjans, L. T. de Haan, A. P. H. J. Schenning, T. Peijs, C. W. M. Bastiaansen, *ACS Appl. Mater. Interfaces* **2013**, 5, 4945.
- [19] T. J. White, *Photomechanical Materials, Composites, and Systems: Wireless Transduction of Light into Work*, John Wiley & Sons, Ltd., Chichester, UK **2017**.
- [20] L. T. De Haan, A. P. H. J. Schenning, D. J. Broer, *Polymer* **2014**, 55, 5885.
- [21] B. A. Kowalski, T. C. Guin, A. D. Augustine, N. P. Godman, T. J. White, *ACS Macro Lett.* **2017**, 6, 436.
- [22] H. Zeng, P. Wasylczyk, G. Cerretti, D. Martella, C. Parmeggiani, D. S. Wiersma, *Appl. Phys. Lett.* **2015**, 106, 1.

- [23] a) T. Seki, *Polym. J.* **2014**, 46, 751; b) A. Martinez, H. C. Mireles, I. I. Smalyukh, *Proc. Natl. Acad. Sci. USA* **2011**, 108, 20891.
- [24] O. Yaroshchuk, Y. Reznikov, T. Galstian, O. Yaroshchuk, A. Checco, V. Lazarev, S. Palto, S. Lee, K.-J. Han, S.-H. Jang, *J. Mater. Chem.* **2012**, 22, 286.
- [25] B. Wei, W. Hu, Y. Ming, F. Xu, S. Rubin, J. Wang, V. Chigrinov, Y. Lu, *Adv. Mater.* **2014**, 26, 1590.
- [26] K. Ichimura, *Chem. Rev.* **2000**, 100, 1847.
- [27] H. Zeng, O. M. Wani, P. Wasylczyk, R. Kaczmarek, A. Priimagi, *Adv. Mater.* **2017**, 29, 1701814.
- [28] L. T. De Haan, C. Sánchez-Somolinos, C. M. W. Bastiaansen, A. P. H. J. Schenning, D. J. Broer, *Angew. Chem., Int. Ed.* **2012**, 51, 12469.
- [29] L. T. De Haan, V. Gimenez-Pinto, A. Konya, T. S. Nguyen, J. M. N. Verjans, C. Sánchez-Somolinos, J. V. Selinger, R. L. B. Selinger, D. J. Broer, A. P. H. J. Schenning, *Adv. Funct. Mater.* **2014**, 24, 1251.
- [30] T. H. Ware, M. E. McConney, J. J. Wie, V. P. Tondiglia, T. J. White, *Science* **2015**, 347, 982.
- [31] M. E. McConney, A. Martinez, V. P. Tondiglia, K. M. Lee, D. Langley, I. I. Smalyukh, T. J. White, *Adv. Mater.* **2013**, 25, 5880.
- [32] S. K. Ahn, T. H. Ware, K. M. Lee, V. P. Tondiglia, T. J. White, *Adv. Funct. Mater.* **2016**, 26, 5819.
- [33] C. Culbreath, N. Glazar, H. Yokoyama, *Rev. Sci. Instrum.* **2011**, 82, 2011.
- [34] H. Wu, W. Hu, H. Hu, X. Lin, G. Zhu, J.-W. Choi, V. Chigrinov, Y. Lu, *Opt. Express* **2012**, 20, 16684.
- [35] B. A. Kowalski, V. P. Tondiglia, T. Guin, T. J. White, *Soft Matter* **2017**, 13, 4335.
- [36] M. Freeman, M. Champion, S. Madhavan, *Opt. Photonics News* **2009**, 20, 28.
- [37] O. Yaroshchuk, H. Gurumurthy, V. G. Chigrinov, H. S. Kwok, H. Hasebe, H. Takatsu, *Proc. IDW* **2007**, 7, 1665.
- [38] S. Iamsaard, S. J. Aßhoff, B. Matt, T. Kudernac, J. J. L. M. Cornelissen, S. P. Fletcher, N. Katsonis, *Nat. Chem.* **2014**, 6, 229.
- [39] M. Yamada, M. Kondo, J. Mamiya, Y. Yu, M. Kinoshita, C. Barrett, T. Ikeda, *Angew. Chem., Int. Ed.* **2008**, 47, 4986.
- [40] A. H. Gelebart, D. J. Mulder, M. Varga, A. Konya, G. Vantomme, E. W. Meijer, R. L. B. Selinger, D. J. Broer, *Nature* **2017**, 546, 632.
- [41] S. Iamsaard, E. Anger, S. J. Aßhoff, A. Depauw, S. P. Fletcher, N. Katsonis, *Angew. Chem., Int. Ed.* **2016**, 55, 9908.
- [42] T. J. White, N. V. Tabiryan, S. V. Serak, U. A. Hrozhyk, V. P. Tondiglia, H. Koerner, R. A. Vaia, T. J. Bunning, *Soft Matter* **2008**, 4, 1796.
- [43] C. D. Modes, M. Warner, *Phys. Rev. E: Stat., Nonlinear, Soft Matter Phys.* **2011**, 84, 1.
- [44] C. L. Van Oosten, D. Corbett, D. Davies, M. Warner, C. W. M. Bastiaansen, D. J. Broer, *Macromolecules* **2008**, 41, 8592.
- [45] K. Kumar, C. Knie, D. Bléger, M. A. Peletier, H. Friedrich, S. Hecht, D. J. Broer, M. G. Debije, A. P. H. J. Schenning, *Nat. Commun.* **2016**, 7, 11975.
- [46] Y. Sawa, F. Ye, K. Urayama, T. Takigawa, V. Gimenez-Pinto, R. L. B. Selinger, J. V. Selinger, *Proc. Natl. Acad. Sci. USA* **2011**, 108, 6364.

PUBLICATION II

Self-Regulating Iris Based on Light-Actuated Liquid Crystal Elastomer

Hao Zeng, Owies M. Wani, Piotr Wasylczyk, Radosław Kaczmarek and Arri
Primagi

Advanced Materials, vol. 29, no. 30, p. 1701814, 2017. Available: [10.1002/adma.201701814](https://doi.org/10.1002/adma.201701814)

Publication reprinted with the permission of the copyright holders.

Self-Regulating Iris Based on Light-Actuated Liquid Crystal Elastomer

Hao Zeng,* Owies M. Wani, Piotr Wasylczyk, Radosław Kaczmarek, and Arri Priimagi*

The iris, found in many animal species, is a biological tissue that can change the aperture (pupil) size to regulate light transmission into the eye in response to varying illumination conditions. The self-regulation of the eye lies behind its autofocusing ability and large dynamic range, rendering it the ultimate “imaging device” and a continuous source of inspiration in science. In optical imaging devices, adjustable apertures play a vital role as they control the light exposure, the depth of field, and optical aberrations of the systems. Tunable irises demonstrated to date require external control through mechanical actuation, and are not capable of autonomous action in response to changing light intensity without control circuitry. A self-regulating artificial iris would offer new opportunities for device automation and stabilization. Here, this paper reports the first iris-like, liquid crystal elastomer device that can perform automatic shape-adjustment by reacting to the incident light power density. Similar to natural iris, the device closes under increasing light intensity, and upon reaching the minimum pupil size, reduces the light transmission by a factor of seven. The light-responsive materials design, together with photoalignment-based control over the molecular orientation, provides a new approach to automatic, self-regulating optical systems based on soft smart materials.

Depending on biological species, pupils come in diverse geometries, comprising ellipses, slits, pin-holes, and crescent shapes, helping animals to adapt to the specific requirements of their living environment.^[1] In the human iris, the sphincter and dilator muscles control the pupil size in order to stabilize the light transmission into the retina.^[2] In all cases, a disturbance in the

iris functionality leads to severe visual dysfunctions. Just as in human/animal eyes, adjustable apertures are vital in technological applications, particularly in imaging systems and spectrometers. Photographic devices commonly contain a mechanical iris diaphragm consisting of several thin segments that form an adjustable polygonal aperture, which allows controlling the depth of field, optical aberrations, and other parameters that influence the image quality.^[3] Spectrometers implement tunable slits to control the resolution and to adjust the overall signal level during data collection.^[4] Recently, compact and tunable aperture devices have been made using different actuation mechanisms, e.g., electromagnetic heating,^[5] electrowetting in microfluidics^[6,7] and piezomechanics.^[8] All these iris-like devices are passive in the sense that they require external control (i.e., a separate controller apart from the iris) and ex situ light detection schemes. An iris device that can self-adjust the aperture size in response to incident light intensity would provide access to auto-

mated optical systems in environments where no controlling circuits can access, e.g., optofluidic channels. However, their technical realization remains a grand challenge.

The only way to realize an iris device that senses the light field is to fabricate it from a material that itself is photoresponsive, and devise a configuration that opens/closes in response to decreasing/increasing light levels. As we show, such actuation can be reached in light-responsive liquid crystal elastomers (LCEs), which are smart materials that can exhibit large shape deformation upon illumination.^[9–11] Light-responsive LCEs comprise a loosely crosslinked network of liquid-crystalline moieties with controlled molecular alignment, whereas the light-active units can be either part of the polymer network^[12] or simply doped into it.^[13] The elastic network can undergo reversible shape changes in response to photochemical^[9] (e.g., *trans-cis* isomerization) or photothermal^[14] stimulus. In either case, the benefit of the light-based actuation scheme relies on remote, noncontact energy supply, and the precise spatial and temporal control over light properties. Several LCE-based soft-robotic devices have been reported exploiting these features, such as microswimmers,^[15,16] walkers,^[17,18] and transportation devices.^[19] Self-regulating behavior in light-driven LCE film has been demonstrated in simple photomechanical oscillating systems,^[20] and recently

Dr. H. Zeng, O. M. Wani, Prof. A. Priimagi
Laboratory of Chemistry and Bioengineering
Tampere University of Technology
P. O. Box 541, Tampere FI 33101, Finland
E-mail: hao.zeng@tut.fi; arri.priimagi@tut.fi

Dr. P. Wasylczyk
Photonic Nanostructure Facility
Institute of Experimental Physics
Faculty of Physics
University of Warsaw
ul. Pasteura 5, Warsaw 02-093, Poland

Dr. R. Kaczmarek
Department and Clinic of Ophthalmology
Wrocław Medical University
ul. Borowska 213, Wrocław 50-556, Poland

The ORCID identification number(s) for the author(s) of this article can be found under <https://doi.org/10.1002/adma.201701814>.

DOI: 10.1002/adma.201701814

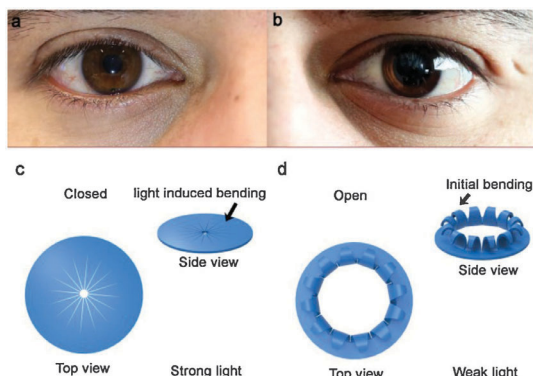


Figure 1. Human iris a) closes in a bright environment and b) opens in the dark. c) Schematic drawing of the light-driven iris at its closed state, where light illumination triggers petal segments to bend inward and to reduce the aperture size. d) The iris is open under weak/no light conditions, when the anisotropic thermal expansion induces bending in the segments, thus opening the aperture.

in an artificial flytrap device capable of autonomous action based on optical feedback.^[21]

Herein, we report an LCE iris that can autonomously open and close by responding to the incident light intensity, without any need for external control circuitry. Mimicking the properties of a natural iris (**Figure 1a,b**), the device opens/closes upon decreasing/increasing light levels. To accomplish the first goal, we use LCE-based soft actuator and light-induced bending as the mechanism responsible for the modification of the aperture size. To fulfill the second point, we implement photoalignment-based control over molecular alignment to achieve radial molecular orientation within the LCE film, and fabricate a structure with 12 radially aligned segments (**Figure 1c,d**). We employ anisotropic thermal expansion within the polymerized LCE to maintain the iris in the open state under low-light conditions, while at increased exposures, light-triggered reorientation forces the iris to close and thus to reduce the aperture size. To the best of our knowledge, this is the first demonstration of artificial iris that is both powered and controlled with light, performing transmission adjustment relying directly on external light intensity.

Bending of a thin strip is the most common way to characterize liquid-crystal polymer actuation under external stimuli.^[22–25] From the technological point of view, it is often most convenient to fabricate an LCE film in a glass cell, with thickness d ranging from a few to a few tens of μm and length l of several millimeters. In such films, bending upon light absorption is due to the strain difference $\Delta\epsilon$ occurring between the two surfaces, with a simple relationship between the bending angle α and the geometry: $\alpha \approx \Delta\epsilon \cdot l/d$ ($l \gg d$). Such bending film can be extremely sensitive: for $d = 10 \mu\text{m}$ and $l = 5 \text{ mm}$, $\Delta\epsilon$ as low as 0.16% may be sufficient to induce a bending of 90° . Due to this high sensitivity, changes in the bending angle are affected by many parameters such as environmental variations, inhomogeneities in the material composition, or imperfections in the film fabrication process. It

is widely accepted that the initial bending existing even when the film is not exposed to light, is due to residual stress in the LC network generated during photopolymerization.^[26,27] The nature of the residual stress is complex, depending delicately on the molecular system used. Apart from nonuniform shrinkage,^[28] other reasons for building up the residual stress during polymerization could be for instance opposite diffusion of monoacrylate and diacrylate monomers during photopolymerization,^[29] and *cis-to-trans* isomerization in the darkness after photopolymerization.^[26] However, the initial bending phenomenon has rarely been connected with anisotropic thermal expansion,^[30,31] and to the best of our knowledge, it has not been previously utilized in soft actuator design.

Liquid crystal elastomers are anisotropic materials, exhibiting not only optical birefringence but also anisotropic thermal expansion governed by molecular orientation.^[23,32] This is pertinent when the photopolymerization is performed at elevated temperatures in order to stabilize the LC phase. **Figure 2a** illustrates an LCE film polymerized at temperature T_p , which is higher than the room temperature T_R . When a strip is cut out from the film, it remains flat only when the environmental temperature T_e is equal to T_p . After polymerization, however, the actuation experiments are typically carried out at room temperature (in our case $T_R = 22^\circ\text{C}$), tens of $^\circ\text{C}$ below the T_p . In a splay-aligned film, different thermal expansion at different film surfaces will create the stress and thus induce spontaneous bending of the film. When the same film is polymerized at T_R ($T_p = T_R$), no stress is preserved inside the material at T_R and no spontaneous bending occurs. However, when T_e is elevated, the strip bends to the opposite direction, as illustrated in **Figure 2b**. To demonstrate the utility of the anisotropic thermal expansion, we prepared a series of $20 \mu\text{m}$ thick splay-aligned LCE strips, polymerized them at different temperatures, and monitored the bending angles α (upon no light irradiation) at different temperatures. As shown in **Figure 2c**, an LCE strip polymerized at 40°C (solid pink dot), shows gradually increasing bending deformation upon slow cooling, reaching the maximum bending at T_R . A strip polymerized at 20°C (red dots) remains flat at T_R . In **Figure 2d** we plot the α versus temperature difference ΔT between polymerization and room temperature, showing that for $\Delta T > 0$, i.e., when the polymerization temperature is higher than the operation temperature, maximum initial bending occurs when the polymerization temperature is 20–30 $^\circ\text{C}$ higher than the operation temperature. With the photopolymerizable mixture we employed, further increase in the polymerization temperature to 60°C ($\Delta T = 38^\circ\text{C}$) brings the mixture close to the LC-to-isotropic phase transition temperature, $T_c = 64^\circ\text{C}$, in which case even slight absorption from the polymerizing light can trigger partial phase transition, reduce the order parameter, and thus decrease the bending angle of the LCE strip at T_R . We note that this initial bending (for $\Delta T > 0$) is in the direction opposite to the light-induced bending. Therefore, we can make use of it in our artificial iris design (**Figure 1c,d**), making it open in the dark, and closed upon light illumination, which is opposite to “conventional,” commonly used light-induced bending in LCE films.

To realize the LCE iris, it is imperative that all the bending segments actuate symmetrically toward the same central point, requiring the LCE constituents to be radially aligned. Obtaining

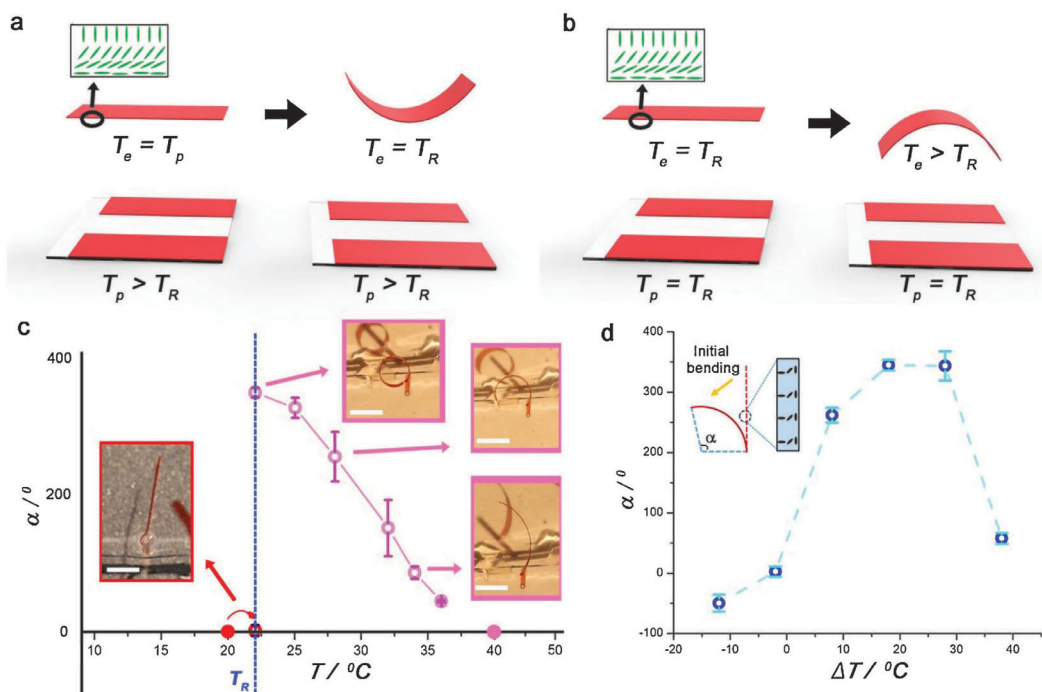


Figure 2. a) Schematic drawing of a splay-bend LCE strip polymerized at an elevated temperature ($T_p > T_R$). It remains flat when the environmental temperature $T_e = T_p$, and spontaneously bends toward the homeotropic direction due to anisotropic thermal expansion when the temperature is reduced to T_R . b) The same strip polymerized at T_R , remains flat at T_R and bends to the opposite direction at an elevated temperature ($T_e > T_R$). c) The measured bending angle α of LCE strips polymerized at different temperatures T_p . The two LCE strips remain flat at the polymerization temperature ($\alpha = 0$, solid dots on the x-axis), and bend with different angles when environmental temperature is changed (empty circles). Insets: photographs of the LCE strips ($6 \times 1 \times 0.02 \text{ mm}^3$) at different temperatures. d) Bending angle versus temperature difference ΔT between polymerization temperature and room temperature. Inset: Schematic drawing of the anisotropic thermal expansion bending direction with respect to the splayed molecular orientation within the strip. Error bars in (c) and (d) indicate standard deviation for three independent measurements.

such alignment using conventional preparation procedures such as rubbing and mask-exposure^[17,33,34] is challenging, hence we used photoalignment technique^[35–37] to achieve the desired molecular alignment. The sample preparation procedure is illustrated in **Figure 3**. The LC cell (20 μm thick) was constructed such that at the upper surface the LC molecules adopted homeotropic alignment, while the bottom surface was coated with an azobenzene-based photoalignment layer (PAAD-72, BEAM Co.), allowing us to define the LC alignment with polarization of the incident light (**Figure 3b,c**). To obtain the radial molecular alignment, we used a radial-polarization converter^[38] to transform linearly polarized light into azimuthally polarized, as illustrated in **Figure 3d**. The molecules within the photoalignment layer orient themselves in the direction perpendicular to the polarization of the incident light, hence azimuthal polarization gives rise to radial photoalignment (**Figure 3c,d**) and, consequently, radial alignment of the photopolymerizable LC mixture close to the bottom surface of the cell. To make the mixture responsive to visible light (we wanted to avoid using UV light in order to obtain “human-friendly” action) we doped it with Disperse Red 1 (DR1, 4 mol%). Upon irradiation with wavelengths in the blue–green region of the

spectrum, DR1 is known to undergo continuous *trans*–*cis*–*trans* cycling, thereby releasing a significant amount of heat. It is the photothermal heating that we employ in our actuator design. The chemical structures of the compounds used in this work are shown in **Figure 3e**. The polymerization was carried out at 45 $^\circ\text{C}$ in order to maximize the initial bending (**Figure 2**). After polymerization, the material has a Young’s modulus of 2.5 MPa at room temperature (**Figure S1**, Supporting Information), and its glass transition temperature is below room temperature, as confirmed by the differential scanning calorimetry curves shown in **Figure S2** (Supporting Information). The cross-polarized optical image of the LCE film, shown in the inset of **Figure 3f**, revealed that the radial molecular alignment was preserved after polymerization. After opening the cell, a disc with 14.0 mm diameter (approximately the size of the human iris) with 12 petal-shape segments was cut out (**Figure 3f**). After releasing the stress by annealing at 50 $^\circ\text{C}$, the device spontaneously “opened up” and adapted a flower-like shape at room temperature, with a central hole of about 10 mm in diameter (**Figure 3g**). In this geometry, each “petal” segment is able to deform in response to the local light intensity, as shown in **Movie 1**, where the LCE segments move in

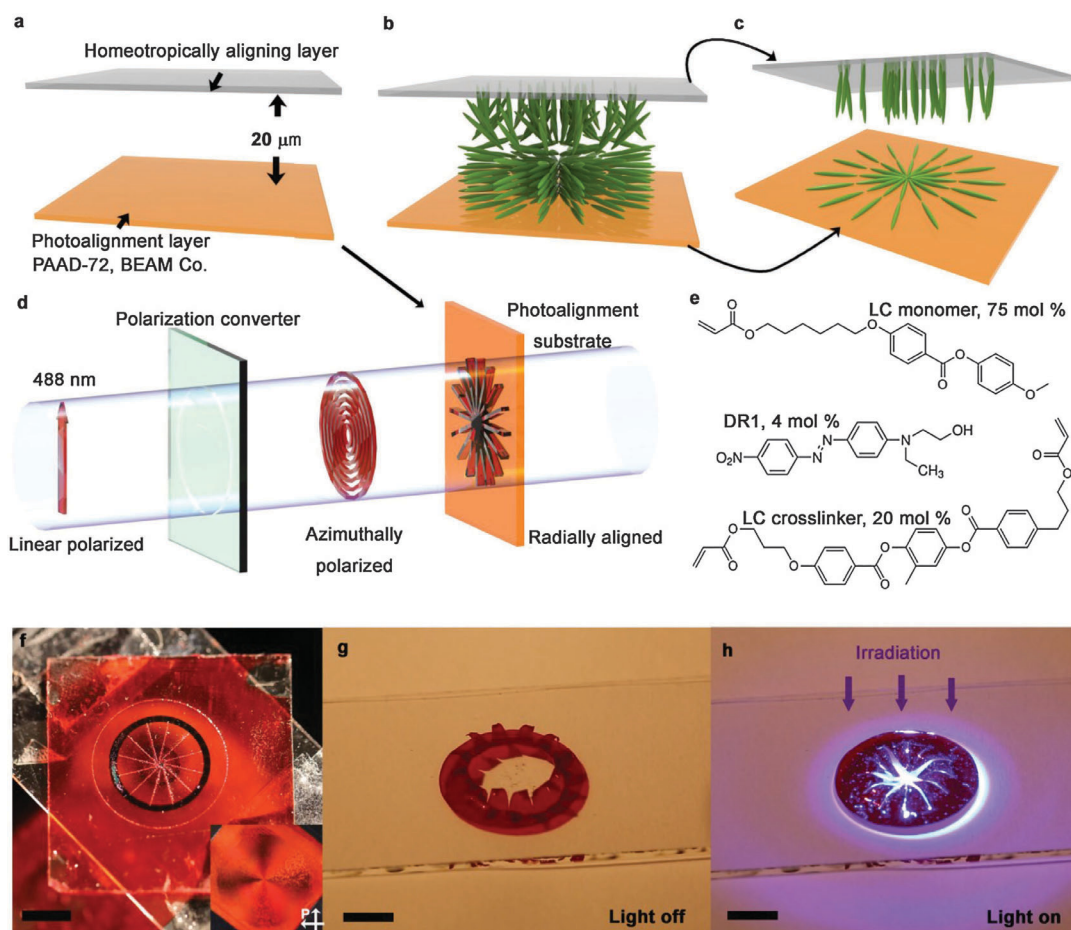


Figure 3. Schematic of the soft iris fabrication process: a) A 20 μm cell is prepared by placing together two glass slides, coated with a homeotropic alignment layer on the top and photoalignment layer at the bottom. b) LC monomer mixture is infiltrated into the cell and it adapts a centrally symmetric splayed alignment, directed by c) molecular orientation at the top and bottom interfaces. d) Schematic of the photoalignment setup. A linearly polarized 488 nm laser beam is converted into azimuthally polarized by using a polarization converter, and then projected onto the substrate coated with the photoalignment layer, due to which the azobenzene molecules within the photoalignment layer adapt radial distribution. e) Chemical composition of the LC mixture used. f) Optical image of the polymerized LCE film cut out with a circle and with 12 petal-like segments. Inset: cross-polarized image of the film before cutting. g) Soft LCE iris in the open state when no light impinges on it. h) The iris closes upon light illumination (470 nm, 250 mW cm^{-2}). Scale bars are 5 mm.

response to a scanned light beam. Upon uniform illumination with 470 nm light emitting diode (LED) light, all iris segments bend inward and the aperture closes (Figure 3h, Movie 2). For more details on the fabrication process, we direct the reader to the Supporting Information.

To characterize the performance of the device, a 488 nm laser beam with a diameter of 12 mm was projected onto the iris, and the transmitted light as a function of the incident light power was measured (Figure 4a). When the incident power was slowly increased from 20 to 120 mW, all segments deformed inward and gradually reduced the aperture size. For laser powers above 120 mW, some segments closed completely, resulting in a rapid

decrease in the iris transmission. At around 180 mW all the segments bent inward and the aperture closed, reaching transmission as low as 10%. The self-regulating iris is able to adjust the transmitted light power across a 200 mW range: ≈ 20 mW of light is transmitted for both 30 mW input (corresponding to 70% transmission) and 200 mW input (10% transmission; red line in Figure 4a). Figure 4b shows the iris response dynamics after the device is illuminated instantaneously with 270 mW cm^{-2} intensity and the output power through the iris is recorded. The decreasing curve of the output power comprises several steps, each of them corresponding to one or few iris segments closing. Differences in the closure time for different

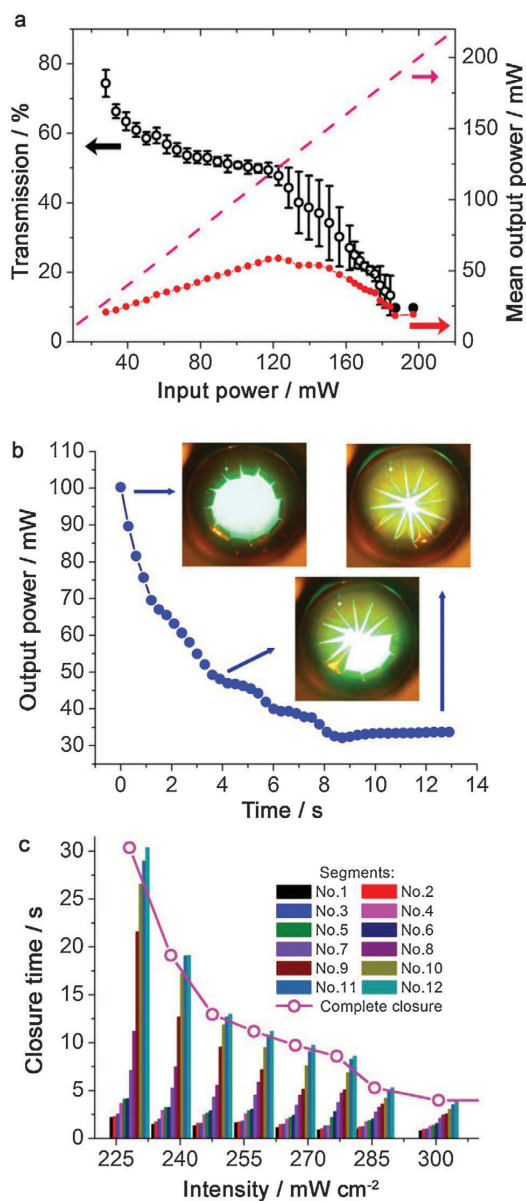


Figure 4. a) Measured transmission (black dots) and transmitted power (red dots) at different input powers. Light source: 488 nm laser with circular polarization; Beam diameter: 12 mm. Error bars indicate standard deviation for three independent measurements. Transmitted power presents the average output power from three independent measurements, and the dashed line represents the case of 100% transmission through the device. b) Measured output power at different times after switching on the light at $t = 0$ s. Intensity: 270 mW cm^{-2} . Insets: Photographs of the iris at different stages. An optical filter is used to block wavelengths below 500 nm. c) Closure time for 12 petal segments at different illumination intensities. The last closed segment defines the complete closure time.

segments are attributed to fabrication defects (e.g., slight variation of thickness and molecular alignment between segments), and high sensitivity of the bending actuation. Images of the iris at different stages of the closing action are shown in the insets of Figure 4b, revealing the separated closed segments and asymmetric shape of the aperture at the intermediate stages. The asymmetric shape of the aperture does not harm the image processing in photographic application, but it may offer novel optical functionalities. The diversity in the material design and the versatility of the photoalignment-based patterning technique^[39] also provide the opportunities to realize artificial irises with different shapes and photodeformation modes, mimicking the diverse iris geometries observed for different animal species.^[1] Real-time closing action is shown in Movie 3, where an iris is placed in front of an LED light source and responds to blocking the light beam. Figure 4c plots the closure times for the 12 individual segments under different incident light intensities. Upon low-intensity excitation, the closure time varies significantly for the different segments, whereas the variation is much smaller at high light intensities. The statistical analysis of the closure times is shown in Figure S3 of the Supporting Information. The complete closure action takes place in 30 s upon 230 mW cm^{-2} incident light intensity, and in less than 5 s upon 300 mW cm^{-2} irradiation.

We attribute the closing action of the iris mostly to photo-thermal heating of the LCE film.^[14] The heating is demonstrated in Movie 4, showing the light-induced temperature increase of the LCE film imaged with an infrared camera, revealing that the iris becomes flat (all segments closed) when the maximum temperature within the segments reaches 49°C . This value is consistent with the polymerization temperature (45°C), in which case no initial bending due to the anisotropic thermal expansion is expected (see the pink dots in Figure 2c). Different from photochemical (isomerization-induced) actuation that is strongly influenced by optical density,^[9] the light-induced temperature increase is insensitive to light penetration depth into the material. During photothermal actuation, both material surfaces experience similar temperature increase due to fast heat conduction across the relatively thin film. The temperature-dependent actuation properties allow us to also obtain an iris device with opposite action, i.e., one that is closed in the dark and opens upon light irradiation. This is demonstrated in Movie 5, showing an iris deforming on a hot plate at 50°C , closing up without light and opening again upon illumination. As an additional benefit, the system can be made sensitive to different wavelengths of light, simply by changing the dye inducing the photothermal effect, while sensitivity over broader spectral range can be obtained by doping the system with several dyes or broadband absorbers. We note that the dyes do not have to be azobenzenes,^[14] as we believe photoisomerization to play only a minor role in the performance of the iris. However, if photochemical actuation was implemented instead of light-induced heating, the iris functionality could be obtained also in liquid environment, paving way toward optofluidic applications or actuation in biologically relevant environments.

To conclude, we report what we believe to be the first artificial iris that can self-regulate the aperture size in direct response to the incident light intensity variations. We employ anisotropic thermal expansion of LCEs in order to maintain the

iris in the open state in the dark, while radial molecular alignment was used to induce circularly symmetric actuation of the iris segments, thus closing the aperture upon illumination with visible light. The diversity of material design and sophisticated form of actuation paves way toward adjustable soft optics with light-control capacity, and offers alternatives to realize micro-robotic systems with smart features, such as self-recognition, stabilization, and automatic manipulation.

Experimental Section

Materials: The LCE actuator is made by polymerization of a mixture that contains 75 mol% of LC monomer 4-methoxybenzoic acid 4-(6-acryloyloxyhexyloxy)phenyl ester, 20 mol% of LC crosslinker 1,4-Bis-[4-(3-acryloyloxypropyloxy)benzoyloxy]-2-methylbenzene (both purchased from Syntho chemicals), 4 mol% of light-responsive molecule *N*-ethyl-*N*-(2-hydroxyethyl)-4-(4-nitrophenylazo)aniline (Disperse Red 1, Sigma-Aldrich), and 1 mol% of photoinitiator (2,2-dimethoxy-2-phenylacetophenone, Sigma-Aldrich). All compounds were used as received. For sample preparation details, see the Supporting Information.

Characterization: Absorption spectra were measured with a custom-modified UV–vis spectrophotometer (Cary 60 UV–vis, Agilent Technologies) with a polarization controller. Optical images and movies were recorded by using a Canon 5D Mark III camera ($f = 100$ mm lens), and thermal images were recorded with an infrared camera (FLIR T420BX, close-up $2 \times$ lens, $50 \mu\text{m}$ resolution). Spatially filtered light from a continuous-wave laser (488 nm, Coherent Genesis CX SLM) was expanded to a diameter of 12 mm and controlled with a beam shutter before impinging on the soft iris. The light impinged onto the iris always from the side with bent segments, in order to avoid shadowing by the exterior sections of the iris. The power of incident and transmitted light were measured with a microscope-slide power sensor (Thorlabs, S170C). For the iris actuation demonstrations (Movies 1, 2, 3, 5), an LED (Prior Scientific, 470 nm) with tunable output power was used for light actuation. For temperature-dependent bending angle measurements, LCE strips were immersed in a water bath on a heating stage. An infrared camera was used to monitor the water temperature, and the images at different water temperatures were captured using the Canon camera in the top view. No sensitivity to humidity was found in the LCE. For measuring the mechanical properties, a planar-aligned LCE sample with dimensions $10 \times 2 \times 0.05 \text{ mm}^3$ was cut along the nematic director, and vertically attached to a force sensor and a linear motor stage. The stress–strain curve was measured at room temperature. Differential scanning calorimetry measurement was performed with a Mettler Toledo Star DSC821e instrument, using heating/cooling speeds of $10^\circ\text{C min}^{-1}$.

Supporting Information

Supporting Information is available from the Wiley Online Library or from the author.

Acknowledgements

A.P. gratefully acknowledges the financial support of the European Research Council (Starting Grant project PHOTOTUNE; Agreement No. 679646). O.M.W. is thankful to the graduate school of Tampere University of Technology (TUT), and H.Z. to the TUT postdoctoral fellowship program, for supporting this work. The authors are indebted to S. L. Oscuro and M. Saccone for assistance with photoalignment patterning and DSC experiments, respectively. The authors thank Dr. Nelson Tabiryan from BEAM co. (<http://www.beamco.com>) for providing the photoalignment material PAAD-72 for the use.

Conflict of Interest

The authors declare no conflict of interest.

Keywords

azobenzene, biomimetic materials, iris, liquid crystal elastomer, photoactuation

Received: April 1, 2017

Revised: April 20, 2017

Published online: June 7, 2017

- [1] J. González-Martín-Moro, F. Gómez-Sanz, A. Sales-Sanz, E. Huguet-Baudin, J. Murube-del-Castillo, *Arch. Soc. Esp. Oftalmol.* **2014**, *89*, 484.
- [2] R. S. Snell, M. A. Lemp, *Movements of the Eyeball and the Extraocular Muscles, in Clinical Anatomy of the Eye*, 2nd ed., Blackwell Science Ltd., Oxford, UK **1997**.
- [3] E. Allen, S. Triantaphillidou, *The Manual of Photography*, 10th ed., Elsevier Ltd., Oxford, UK **2012**.
- [4] J. M. Lerner, *Cytometry, Part A* **2006**, *69A*, 712.
- [5] S. Schuhladen, F. Preller, R. Rix, S. Petsch, R. Zentel, H. Zappe, *Adv. Mater.* **2014**, *26*, 7247.
- [6] P. Muller, R. Feuerstein, H. Zappe, *J. Microelectromech. Syst.* **2012**, *21*, 1156.
- [7] S. Schuhladen, K. Banerjee, M. Sturmer, P. Muller, U. Wallrabe, H. Zappe, *Light Sci. Appl.* **2016**, *5*, e16005.
- [8] J. Draheim, T. Burger, J. G. Korvink, U. Wallrabe, *Opt. Lett.* **2011**, *36*, 2032.
- [9] T. Ikeda, J.-I. Mamiya, Y. Yu, *Angew. Chem., Int. Ed.* **2007**, *46*, 506.
- [10] C. Ohm, M. Brehmer, R. Zentel, *Adv. Mater.* **2010**, *22*, 3366.
- [11] M. H. Li, P. Keller, B. Li, X. Wang, M. Brunet, *Adv. Mater.* **2003**, *15*, 569.
- [12] C. L. van Oosten, C. W. M. Bastiaansen, D. J. Broer, *Nat. Mater.* **2009**, *8*, 677.
- [13] M. Camacho-Lopez, H. Finkelmann, P. Palffy-Muhoray, M. Shelley, *Nat. Mater.* **2004**, *3*, 307.
- [14] A. H. Gelebart, G. Vantomme, B. E. W. Meijer, D. J. Broer, *Adv. Mater.* **2017**, *29*, 1606712.
- [15] C. Huang, J.-a. Lv, X. Tian, Y. Wang, Y. Yu, J. Liu, *Sci. Rep.* **2015**, *5*, 17414.
- [16] S. Palagi, A. G. Mark, S. Y. Reigh, K. Melde, T. Qiu, H. Zeng, C. Parmeggiani, D. Martella, A. Sanchez-Castillo, N. Kapernaum, F. Giesselmann, D. S. Wiersma, E. Lauga, P. Fischer, *Nat. Mater.* **2016**, *15*, 647.
- [17] M. Rogoz, H. Zeng, C. Xuan, D. S. Wiersma, P. Wasylczyk, *Adv. Opt. Mater.* **2016**, *4*, 1689.
- [18] H. Zeng, P. Wasylczyk, C. Parmeggiani, D. Martella, M. Buresi, D. S. Wiersma, *Adv. Mater.* **2015**, *27*, 3883.
- [19] E. Kizilkan, J. Strueben, A. Staubitz, S. N. Gorb, *Sci. Rob.* **2017**, *2*, eaak9454.
- [20] T. J. White, N. V. Tabiryan, S. V. Serak, U. A. Hrozhyk, V. P. Tondiglia, H. Koerner, R. A. Vaia, T. J. Bunning, *Soft Matter* **2008**, *4*, 1796.
- [21] O. M. Wani, H. Zeng, A. Priimagi, *Nat. Commun.* **2017**, DOI: 10.1038/ncomms15546.
- [22] S. Iamsaard, S. J. Aßhoff, B. Matt, T. Kudernac, J. J. L. M. Cornelissen, S. P. Fletcher, N. Katsonis, *Nat. Chem.* **2014**, *6*, 229.
- [23] G. N. Mol, K. D. Harris, C. W. M. Bastiaansen, D. J. Broer, *Adv. Funct. Mater.* **2005**, *15*, 1155.
- [24] D. Corbett, M. Warner, *Liq. Cryst.* **2009**, *36*, 1263.

- [25] C. L. van Oosten, D. Corbett, D. Davies, M. Warner, C. W. M. Bastiaansen, D. J. Broer, *Macromolecules* **2008**, *41*, 8592.
- [26] K. Kumar, C. Knie, D. Bleger, M. A. Peletier, H. Friedrich, S. Hecht, D. J. Broer, M. G. Debye, A. P. H. J. Schenning, *Nat. Commun.* **2016**, *7*, 11975.
- [27] Y. Sawa, F. Ye, K. Urayama, T. Takigawa, V. Gimenez-Pinto, R. L. B. Selinger, J. V. Selinger, *Proc. Natl. Acad. Sci. USA* **2011**, *108*, 6364.
- [28] R. A. M. Hikmet, B. H. Zwerter, D. J. Broer, *Polymer* **1992**, *33*, 89.
- [29] C. F. van Nostrum, R. J. M. Nolte, D. J. Broer, T. Fuhrman, J. H. Wendorff, *Chem. Mater.* **1998**, *10*, 135.
- [30] L. T. de Haan, V. Gimenez-Pinto, A. Konya, T.-S. Nguyen, J. M. N. Verjans, C. Sánchez-Somolinos, J. V. Selinger, R. L. B. Selinger, D. J. Broer, *Adv. Funct. Mater.* **2014**, *24*, 1251.
- [31] J. J. Wie, K. M. Lee, T. H. Ware, T. J. White, *Macromolecules* **2015**, *48*, 1087.
- [32] D. J. Broer, G. N. Mol, *Polym. Eng. Sci.* **1991**, *31*, 625.
- [33] S. Varghese, S. Narayanankutty, C. W. M. Bastiaansen, G. P. Crawford, D. J. Broer, *Adv. Mater.* **2004**, *16*, 1600.
- [34] L. T. de Haan, C. Sánchez-Somolinos, C. M. W. Bastiaansen, A. P. H. J. Schenning, D. J. Broer, *Angew. Chem., Int. Ed.* **2012**, *51*, 12469.
- [35] T. H. Ware, M. E. McConney, J. J. Wie, V. P. Tondiglia, T. J. White, *Science* **2015**, *347*, 982.
- [36] O. Yaroshchuk, Y. Reznikov, *J. Mater. Chem.* **2011**, *22*, 286.
- [37] T. Seki, S. Nagano, M. Hara, *Polymer* **2013**, *54*, 6053.
- [38] M. Stalder, M. Schadt, *Opt. Lett.* **1996**, *21*, 1948.
- [39] M. E. McConney, A. Martinez, V. P. Tondiglia, K. M. Lee, D. Langley, I. I. Smalyukh, T. J. White, *Adv. Mater.* **2013**, *25*, 5880.

PUBLICATION III

A light-driven artificial flytrap

Owies M. Wani, Hao Zeng and Arri Priimagi

Nature Communications, vol. 8, p. 15546, 2017. Available: [10.1038/ncomms15546](https://doi.org/10.1038/ncomms15546)

Publication reprinted with the permission of the copyright holders.

ARTICLE

Received 31 Jan 2017 | Accepted 7 Apr 2017 | Published 23 May 2017

DOI: 10.1038/ncomms15546

OPEN

A light-driven artificial flytrap

Owies M. Wani¹, Hao Zeng¹ & Arri Priimagi¹

The sophistication, complexity and intelligence of biological systems is a continuous source of inspiration for mankind. Mimicking the natural intelligence to devise tiny systems that are capable of self-regulated, autonomous action to, for example, distinguish different targets, remains among the grand challenges in biomimetic micro-robotics. Herein, we demonstrate an autonomous soft device, a light-driven flytrap, that uses optical feedback to trigger photomechanical actuation. The design is based on light-responsive liquid-crystal elastomer, fabricated onto the tip of an optical fibre, which acts as a power source and serves as a contactless probe that senses the environment. Mimicking natural flytraps, this artificial flytrap is capable of autonomous closure and object recognition. It enables self-regulated actuation within the fibre-sized architecture, thus opening up avenues towards soft, autonomous small-scale devices.

¹Laboratory of Chemistry and Bioengineering, Tampere University of Technology, PO Box 541, FI-33101 Tampere, Finland. Correspondence and requests for materials should be addressed to H.Z. (email: hao.zeng@tut.fi) or to A.P. (email: arri.priimagi@tut.fi).

Ranging from multiscale and functional self-assemblies to morphology control, complex locomotion strategies and autonomous feedback dynamics, nature has provided us with numerous fascinating examples for biomimetic research^{1–5}. Recently, great efforts have been made in mimicking organic species to devise micro-robotic systems with novel functionalities and accessibility to increasingly challenging spaces^{6–10}. However, mimicking the intelligence of natural species in artificial systems, that is, realization of devices that act autonomously and are capable of adapting to unexpected environmental changes, is a long-standing challenge. To date, the mainstream research on artificial intelligence is based on programming, hence relying on computer-controlled electronic actuation¹¹. However, incorporation of complex computing circuitry, power sources and electrically driven actuators into miniaturized robotic systems is challenging, and other approaches are needed to devise smart robotic actuators.

Soft-matter-based micro-robotics is a nascent field in biomimetic research, with significant progress in the past few years^{12,13}. Unlike conventional hard machines with rigid arms, soft robots provide natural safety and human-friendly contact. The flexible and miniaturized body also offers additional freedom for complex motion and adaptation to environmental confinement^{14,15}. Several powering strategies have been developed for soft robotics, such as pneumatic networks¹², light illumination^{13,15} and chemical reactions¹⁶. Automation is a particular challenge in soft devices, since the ways of powering and control need to be completely re-thought. A limited number of attempts have been made to create self-oscillating devices^{16–19} – autonomous systems that could extract energy from a constant source and transfer it to cyclic mechanical work. Most of them employ stimuli-responsive materials such as light-responsive polymers^{17,18} or chemically responsive hydrogels¹⁹, in which a non-equilibrium oscillation occurs once a positive feedback

mechanism²⁰ is established between deformed geometry and external stimulus field.

Here, we demonstrate an intelligent gripping device, a light-driven artificial flytrap. The name stems from the fact that the device is capable of mimicking the motions of natural flytrap (*Dionaea muscipula*)^{21,22}, by performing autonomous closure action (gripping) and self-recognition between different micro-objects by sensing their physical properties.

Results

System concept. Venus Flytrap²¹ (Fig. 1a,b) has fascinated scientists due to its unique features such as automatic closure of leaf upon mechanical stimulation, sub-second-scale fast actuation, and ability to distinguish insects and other prey from random particles like dust. Inspired by the flytrap, we propose a strategy to realize an artificial, fully light-fueled micro-device. We use a thin layer of light-responsive liquid-crystal elastomer (LCE) as an actuating material. LCEs are smart materials that can undergo huge shape changes in response to various external stimuli such as light, heat, or electric field^{23–26}. Among the different stimuli, light is in many ways particularly attractive. It provides a clean, contactless energy source, and its properties (wavelength, intensity, polarization) can be optimized for a specific target with high spatial and temporal resolution. Therefore, several light-powered, LCE-based robotic^{27–30} as well as tunable photonic^{31–33} systems have been proposed. In essence, the light-induced actuation is based on controlling the molecular alignment within the liquid-crystal polymer network³⁴. By choosing a splayed molecular alignment across the actuator thickness, light-induced alignment changes give rise to different strains within one monolithic layer: an expansion on one surface and contraction on the other. As a consequence, pronounced light-induced bending deformation occurs³⁵ (insets in Fig. 1c,d).

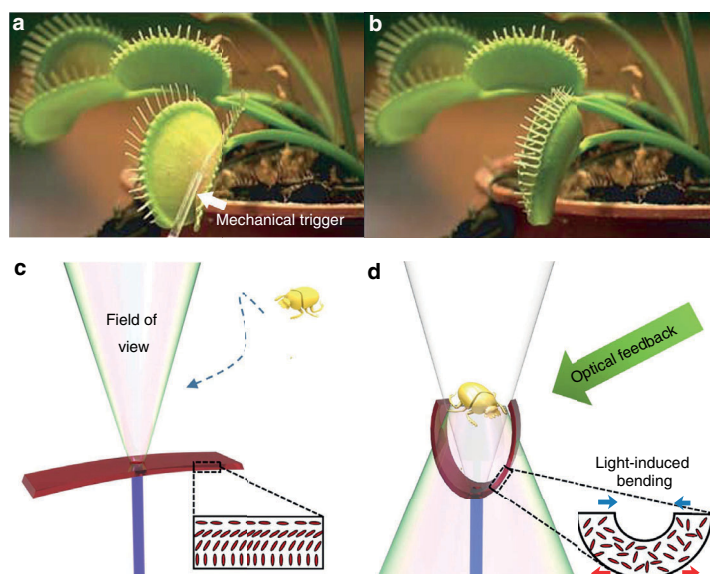


Figure 1 | Flytrap-inspired light-powered soft robot. (a) A Venus flytrap at its open stage, (b) closes upon mechanical stimulation. Reprinted with permission from ref. 21. (c) Schematic drawing of the light-triggered artificial flytrap at its open stage, when no object has entered its field of view. No light is back-reflected to the LCE actuator, which remains in the open stage. (d) The flytrap closes when an object enters its field of view and causes optical feedback to the LCE actuator. Light-induced bending of the LCE leads to closure action, thus capturing the object. The insets of c and d show the schematic molecular orientation in LCE actuator at the open and closed stages.

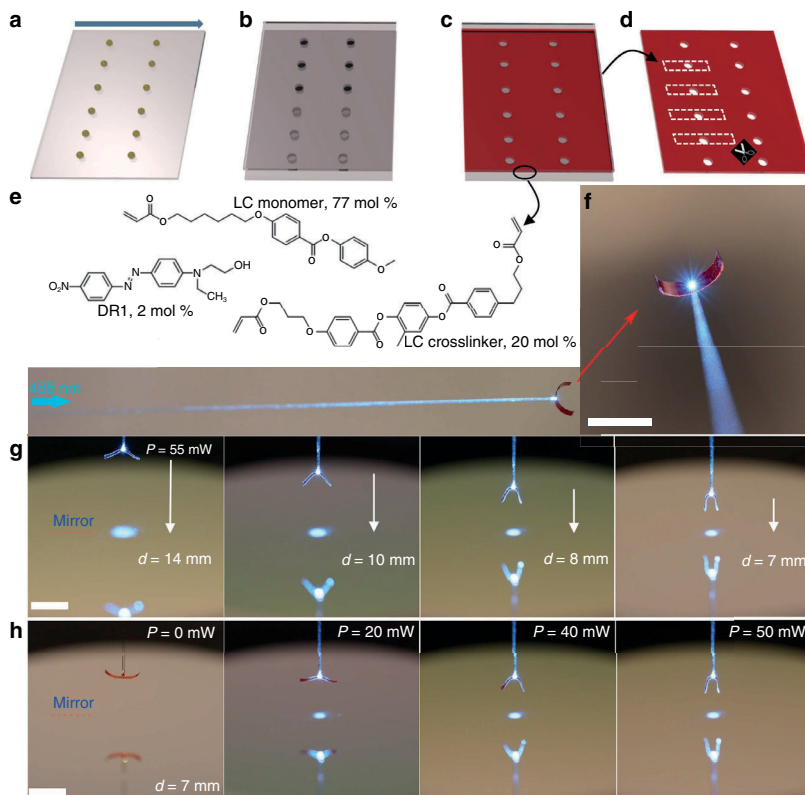


Figure 2 | Realization of the autonomous gripper. Schematic pictures of the fabrication process: (a) Arrays of UV curable resin are put on a glass substrate coated with rubbed PVA (the arrow indicates the rubbing direction). (b) A 20 μm LC cell is prepared by placing another glass slide coated with homeotropic alignment layer on the top, and subsequent curing with UV light to solidify the resin. (c) Liquid crystal monomers are infiltrated into the cell, and then UV-polymerized at 30 $^{\circ}\text{C}$. (d) The cell is opened, and strips of LCE actuator are cut out from the substrate along the rubbing direction. (e) Chemical composition of the LC monomer mixture. (f) Optical images of the fabricated gripper after connecting to the fibre tip. (g) Gripper automatically closes while approaching to the mirror surface with a constant power of 55 mW. (h) At a constant distance $d = 7$ mm, gripper can be switched between closed and open stages by manually tuning the light power (0, 20, 40, 50 mW). All scale bars correspond to 5 mm.

To make this bending deformation to sense the environment, we integrated the LCE actuator with an optical fibre. More specifically, we fabricated the splay-aligned LCE actuator onto the tip of the fibre, leaving a transparent window in the center, through which light is emitted. The emission cone determines the field of view of the device, which continuously probes the space in front (Fig. 1c). When an object enters into the field of view and produces enough optical feedback (reflected/scattered light), the LCE bends towards the object (closure action), eventually capturing it (Fig. 1d). The optical feedback is determined by the reflectance/scattering intensity of the object, and therefore, the artificial flytrap may exhibit distinct actuation behavior when meeting different targets. Compared with other flytrap-like devices reported to date^{36,37}, this is the first miniature device that mimics the intelligent features of the Venus flytrap, while the mechanical motion is triggered by light-induced bending of the LCE actuator, not elastic instability²¹ as in the case of the Venus flytrap.

System realization. A glass slide coated with polyvinyl alcohol (PVA) was firstly rubbed unidirectionally. Arrays of droplets of UV-curable resin (few nl each) were put onto the surface, separated by ~ 1 cm distance (Fig. 2a). Another glass slide coated

with homeotropic alignment layer was placed on top of the one containing the droplets, maintaining 20 μm separation between the two slides by using spacer beads. Subsequently, a UV lamp was used to cure the resin and form an LC cell (Fig. 2b). Liquid-crystal monomer mixture was then infiltrated at 70 $^{\circ}\text{C}$ and polymerized after cooling to the nematic phase at 30 $^{\circ}\text{C}$. The mixture contained commercially available acrylate-functionalized LC monomers and cross-linkers (Fig. 2e). As a light-responsive unit, we used Dispersed Red 1, added as a dopant into the LCE network, similar to previous reports^{38,39}. This system allows for more than 80% light absorption at the excitation wavelength (488 nm) within the 20 μm thick splay-aligned layer. A UV lamp was used to cure the mixture, forming a well-aligned LCE film with an array of transparent windows (Fig. 2c). The order parameter of the LCE film, as deduced from polarized absorption measurements, was *ca.* 0.6 (see Supplementary Note 1 and Supplementary Fig. 5 for further details). The cell was opened and strips with transparent windows at their central positions were cut along the rubbing direction (Fig. 2d). Finally, the optical flytrap was formed by fixing the tip of a multi-mode optical fibre to the center of the LCE strip by using another droplet of cured resin (attached to the homeotropically-aligned surface). Light from a 488 nm laser was coupled to the other end of the

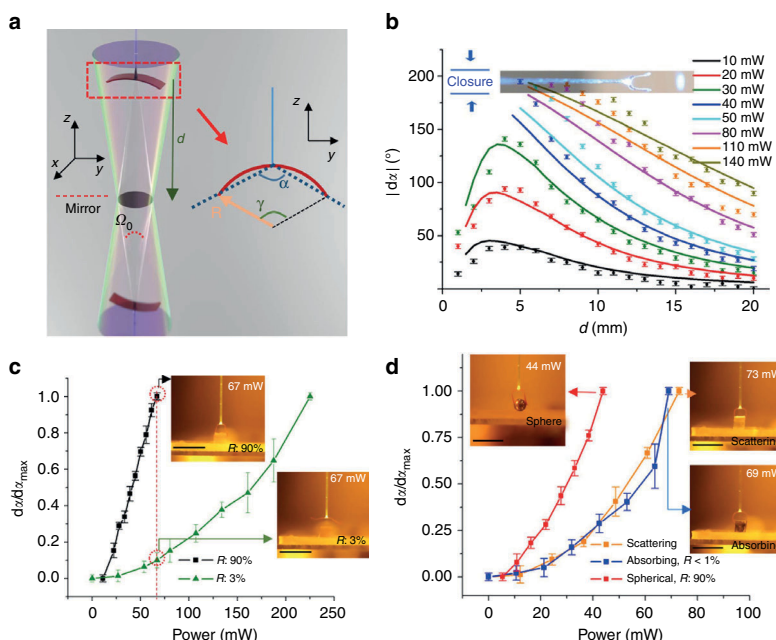


Figure 3 | Recognition between targets by using feedback-type optical actuation. (a) Schematic drawing of the geometry of the flytrap gripper. (b) Change in gripping angle $|dx|$ as a function of distance d at different output powers P (points and lines are experimental and calculated data, respectively). Inset: photograph of the closed gripper with a maximum value in $|dx|$. Error bars indicate the imaging system accuracy (4°) in every single measurement. (c) Measured bending ratio dx/dx_{\max} as a function of input power P for targets with high ($R = 90\%$) and low ($R = 3\%$) reflectivity. Insets: photographs of the gripper at its closed and open stages when meeting high-reflectivity and low-reflectivity targets, respectively (power 67 mW in both cases). (d) Measured bending ratio dx/dx_{\max} as a function of input power P for a glass micro-sphere ($R = 90\%$), a highly absorbing ($R < 1\%$) and highly scattering PDMS targets. Insets: photographs of the closed gripper meeting different targets with different threshold powers: 44 mW for the micro-sphere, 73 mW for the scattering and 69 mW for the absorbing target. The error bars in c and d indicate the imaging system accuracy (4°) plus the s.d. for $n = 3$ measurements. All scale bars correspond to 5 mm. An optical filter is used to block wavelengths below 500 nm for all the photographs.

fibre, and emitted through the center of the device, as shown in Fig. 2f. The transparent window prevents direct light absorption, while all the absorbed light responsible for LCE actuation comes from the reflection/scattering from any encountered object in the probing area. For instance, in front of a highly reflective flat mirror the open gripper (at far distance) performs a gradual closure action when approaching the surface (Fig. 2g). At a fixed distance, the gripping can be manually controlled by changing the output power from the fibre (Fig. 2h, also see Supplementary Movie 1).

Autonomous action and self-recognition based on optical feedback.

To analyse the performance of the optical flytrap, we measured the gripping angles α (Fig. 3a) as a function of distance d from a mirror at different laser powers P . The results are shown in Fig. 3b. Light emits from the fibre tip at a divergence angle β [$\beta = 13^\circ$; $NA = n \cdot \sin\beta$, where NA is the numerical aperture of the fibre (0.22) and n is the refractive index of air], which corresponds to a solid angle Ω_0 [$\Omega_0 = 2\pi(1 - \cos\beta) = 0.216$]. Upon reflection from the mirror, the light propagation preserves the same divergence angle, thus the whole illumination space can be considered as a light cone with its apex at the mirror-symmetric position of the fibre tip (Fig. 3a). By approaching the mirror, the distance between the gripper and the light source ($2d$) decreases, that is, the gripper moves towards a region with higher light intensity. Therefore, more light is absorbed by the actuator, leading to smaller α (closing action). For low laser powers ($P < 40$ mW) and at short distances ($d < 5$ mm), the light cone is

too confined to expose the whole actuator, and larger portion of light energy is absorbed in the central area of the LCE where the cured resin prevents actuation of the LCE strip. Thus, the bending deformation saturates and reaches a maximum value at $d \approx 4$ mm. For higher powers, the gripper reaches the closure stage at a certain distance d_c , depending on the power used (that is, $d_c = 5$ mm for $P = 40$ mW; $d_c = 12$ mm for $P = 140$ mW, see in Fig. 3b).

The total reflected power equals to $P \cdot R$, where R is the reflectivity of the surface. Thus, the energy distribution of the reflected light takes the form $D(\theta, \varphi)$, indicating the percentage of reflected light in $d\Omega = \sin\theta d\theta d\varphi$ solid angle in spherical coordinates $\langle r, \theta, \varphi \rangle$. $D(\theta, \varphi)$ strongly depends on the properties of the reflective surface. For a flat mirror, all energy is concentrated within a light cone with solid angle $\Omega = \Omega_0$ (or $D = 0$ for $|\theta| > \beta$). For a concave surface $\Omega < \Omega_0$, for a convex surface $\Omega > \Omega_0$, and for a scattering surface $\Omega \gg \Omega_0$. The deformed gripper can be approximated as an arc with a central angle of γ (see the inset of Fig. 3a). Thus the change of central angle $d\gamma$ of the gripper can be described as

$$d\gamma = k \cdot E = k \cdot A \cdot P \cdot R \cdot \iint_S D(\theta, \varphi) \frac{\vec{r} d\vec{S}}{r^3} \quad (1)$$

where k is the light-induced bending coefficient, A is absorption efficiency, E is the total absorbed energy per unit time in the actuated area S . The calculated results are shown as lines in Fig. 3b, revealing good consistency between the modelling and the

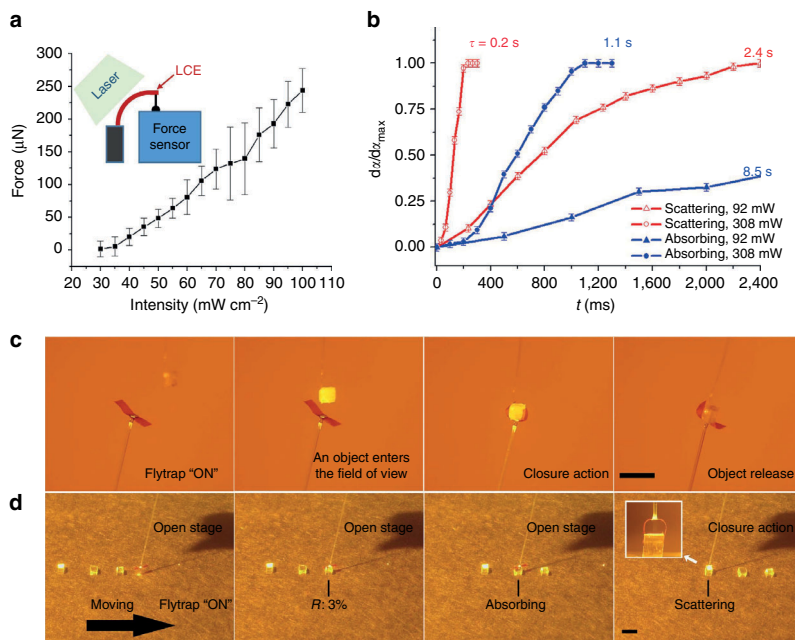


Figure 4 | Flytrap-type capture motion and applications. (a) Measured force from one LCE actuating arm as a function of illuminated laser intensity. Inset: schematic drawing of the experimental set up. Error bars indicate force sensor accuracy (10 μN) plus the s.d. for $n = 3$ measurements. (b) Response time of gripping motion for scattering and absorbing targets by using different laser powers. The error bars indicate the imaging system accuracy (4°) in single measurement. (c) The optical flytrap mimics the motion of a natural flytrap by capturing a small scattering object falling on the gripper ($P = 200 \text{ mW}$). (d) Demonstration of self-detection in a moving production line: no response to a transparent cubic (low reflectivity) or an absorbing cubic (long response time), automatic closure when meeting a highly scattering cubic, creating sufficient optical feedback. $P = 150 \text{ mW}$. Inset: zoom-in side-view optical image of gripping of the scattering cubic. All scale bars are 5 mm. An optical filter is used to block wavelengths below 500 nm for all the photographs.

experimental results. Further details on the modelling can be found in the Supplementary Note 2 and Supplementary Fig. 6.

Equation (1) reveals two working modes for the gripper. Firstly, by changing the light power P , the gripper can be manually, yet remotely, controlled. Secondly, for a constant power, the bending angle varies depending on light reflection. The second working mode is useful for developing a smart robotic system, since the power source is free of human control and the device can operate autonomously through adaptation to environmental changes. Hence, we implemented the second mode to demonstrate feedback-type actuation and autonomous action of the device. Figure 3c plots the change of gripping angle dz (normalized as dz/dz_{max}) as a function of power P for two cubic samples with high and low reflectivity (see Methods for sample fabrication details), demonstrating the distinct actuation behavior in response to different targets. Keeping the same power $P = 67 \text{ mW}$, the gripper closes when observing the highly reflective micro-cubic, while remaining open when a cubic with low reflectivity is in its field of view (insets of Fig. 3c). The same mechanism holds for other targets with arbitrary reflection/scattering patterns, resulting in differentiated power thresholds and actuation dynamics for achieving the same closure action. The actuation threshold and dynamics depend on R as well as on physical properties of the object, affecting the specific form of $D(\theta, \varphi)$. As shown in the insets of Fig. 3d, the gripper closes at 44 mW for a silver-coated micro-bead ($d = 2 \text{ mm}$; $R = 90\%$), and at around 70 mW for a highly scattering cubic and a black, absorbing one ($R < 1\%$), yet with significantly different actuation dynamics. The plots of dz/dz_{max} demonstrate a novel

functionality of LCE actuators: at a specific power the device recognizes its favorite prey and acts autonomously to trap it.

Optical flytrap. Powered by light, this tiny fibre-tip device can grip on any micro-object with arbitrary shape, from cubic to sphere (Fig. 3c,d), from a scattering particle to a piece of foil (Supplementary Movie 2). The gripping force originates from mechanical bending of the soft LCE actuator, which is proportional to the excitation light intensity (Fig. 4a). The bending force is in the hundreds of μN range and can create sufficient adhesion during the gripping process (statistic friction in the normal direction) that sustains the object weight of tens of mg, which is hundreds of times larger than the mass of the actuator itself. The flytrap gripper can serve as an automatic tool to test different objects, target the desired one, and release it rapidly once the light is turned off. The grip-and-release action is demonstrated in Supplementary Movie 3 for a highly scattering micro-cube with a mass of 10 mg. The response time of the optical flytrap depends on the light power, as shown in Fig. 4b and in Supplementary Fig. 1. By increasing the power to about 300 mW, the device closes within 200 ms. As a comparison, natural flytrap snaps in 100 ms, after about 0.7 s delay between the trigger and the snap²¹. Figure 4b also reveals the slow actuation of the black target, which is dominated by heat transfer. Hence, the scattering and absorbing targets are distinguished by the device through different dynamics, even if the actuation threshold (Fig. 3d) is similar for both. The optical flytrap can capture artificial insects (particles) that enter its field of view. Figure 4c and

Supplementary Movie 4 demonstrate this behavior, showing the optical flytrap capturing a piece of rice falling on the device. The device may also potentially be used in manufacturing units that require automatic detection of product defects. We demonstrate this potential in Fig. 4d, where a set of cubic particles are sitting on a production line (a translation stage) moving below the optical flytrap. Once a product that provides sufficient optical feedback (as demonstrated by using a strongly scattering cubic particle) reaches the flytrap, it is automatically selected (Supplementary Movie 5).

Discussion

There are two features in the actuation process that we would like to particularly point out. The first one is closure when meeting a strongly absorbing, unreflective target (Fig. 3d). For a black cubic which reflects less than 1% of light, the optical flytrap closes with a threshold much lower than for a non-absorbing one with 3% reflectance. This can be attributed to photothermal heating of the absorbing object, and subsequent heat transfer to the actuator through the air layer, leading to gripping action. This has been confirmed by imaging the thermal distribution of the system with an infrared camera, as shown in the thermal image in Supplementary Fig. 2. Compared with the conventional actuation scheme where the flytrap absorbs the energy directly from the reflected light, the heat-transfer-based actuation takes place at a much longer time scale (Supplementary Movie 6, Fig. 4b). The second phenomenon to point out is the scaling effect in the power threshold. We have recorded the bending for grippers with different sizes (length 4, 6, 8, 10 mm; width 1 mm). As shown in Supplementary Figs 3,4, the thresholds for different objects scale differently with actuator length. For the black target the threshold is significantly reduced for grippers with smaller sizes, due to enhanced heat transfer efficiency at a reduced distance. The size-dependent character of the gripper may provide an additional degree of freedom to design and optimize the performance of the autonomous actuator. We note also that it is relatively straightforward to scale up the size of the device at least to several centimeters simply by using larger liquid-crystal cells. Masked exposure⁴⁰ and direct laser writing⁴¹, in turn, should allow for fabricating miniature, microscopic-scale gripping devices. The working distance of the device can be controlled by changing the numerical aperture of the optical fibre used.

The performance of the optical flytrap is reversible, i.e., it can perform grip-and-release cycles repeatedly without decrease in efficiency. However, upon high-power illumination (for example, in Fig. 4c) needed for fast actuation, photothermal heating can soften the material, thereby enhancing adhesion between the actuator and the target. After the illumination is ceased and the temperature decreases, adhesion poses a barrier for material relaxation, leading to irreversibility in the actuation process. However, no permanent damage is caused to the material during this process, and its original shape and performance can be retained by annealing the sample at 45 °C. In some cases, the device performance may also be influenced by non-uniform scattering pattern caused by the target. This non-uniform illumination can generate asymmetric actuation between the two gripper arms. An example of this is shown in Supplementary Movie 7, where a curved surface of a micro-bead provides an asymmetric reflected light field, resulting to different LCE deformation at different positions.

More generally, robotics employing smart materials such as LCEs has seen huge progress during the past decade. However, the research focus has mainly lied in sophisticated control over the deformation by modification of the actuator material^{42,43} or in using stimulated sources and complex light patterns^{15,29}. We propose two potential trends for future research. Firstly,

feedback-type actuation allows one to use constant illumination to obtain complex deformation determined by the environment. We demonstrate this in our artificial flytrap, where the action is powered by the light reflected/scattered from nearby objects, as opposed to using the light-triggered deformation as a sensor for detecting environmental variation⁴⁴. Secondly, the actuation process can affect the absorption of light that fuels the photomechanical motion, which in return provides feedback and modulates the original actuation¹⁸. We expect such feedback-type actuators to become pertinent in intelligent micro-robotic systems, therefore bringing novel alternatives for soft-robotic technologies.

In conclusion, we have demonstrated a light-powered gripping device, an artificial flytrap, capable of mimicking the behavior of a natural flytrap. An optical fibre is used to deliver the light energy needed to deform a liquid-crystal elastomer micro-actuator, whose operation is triggered by reflected or scattered light harvested from the environment. Such reflection- or scattering-induced deformation is further applied to induce feedback-type actuation, to obtain autonomous recognition and distinction between different micro-objects. The fibre-tip gripper is a miniature system demonstrating a self-regulating, optically driven device, which may provide a pathway towards autonomous, intelligent micro-robotics.

Methods

Materials. The micro-actuator consists of nematic LCE network polymerized from a mixture containing 77 mol% of LC monomer 4-Methoxybenzoic acid 4-(6-acryloyloxyhexyloxy)phenyl ester (Synthon chemicals), 20 mol% of LC crosslinker 1,4-Bis-[4-(3-acryloyloxypropyloxy)benzoyloxy]-2-methylbenzene (Synthon chemicals), 2 mol% of light-responsive molecule N-Ethyl-N-(2-hydroxyethyl)-4-(4-nitrophenylazo)aniline (Disperse Red 1, Sigma Aldrich), and 1 mol% of photo-initiator (2,2-Dimethoxy-2-phenylacetophenone, Sigma Aldrich). All molecules were used as received. Drops of UV glue (UVS 91, Norland Products INC., Cranbury, NJ) were used as transparent windows in the center of LCE strips and as mechanical connectors between the LCE and the multimode optical fibre (0.22 NA, 200 µm core, Thorlabs).

Sample preparation. For LC cell fabrication, two glass slides were firstly spin coated with 1 wt% water solution of polyvinyl alcohol (PVA Sigma Aldrich; 4,000 r.p.m., 1 min) and homeotropic alignment layer (JSR OPTMER, 6,000 r.p.m., 1 min), respectively. The PVA-coated glass slide was rubbed unidirectionally by using a satin cloth, and subsequently blowed with high-pressure nitrogen to remove any dust particles from the surfaces. Tiny drops of UV glue (few nl each) were picked up by a sharp needle and placed onto the PVA-coated glass, after which the slide with the homeotropic alignment layer was glued on top of the PVA-coated one using 20 µm spacers (Thermo scientific) for defining the cell thickness. A UV LED (Thorlabs; 20 mW cm⁻², 375 nm, 1 min) was used to cure the glue. The monomer mixture was prepared by magnetically stirring the LC mixture at 70 °C (100 r.p.m.) for 1 hour. Then the mixture was infiltrated into the cell on a heating stage at 70 °C and cooled down to 30 °C with a rate of 5 °C min⁻¹, to reach splayed nematic alignment. Another UV LED (Prior Scientific; 150 mW cm⁻², 385 nm, 1 min) was used to polymerize the LC mixture. The cell was opened, and LCE strips were cut out from the sample film by using a blade.

For attaching the optical fibre, firstly the cladding layer was removed, after which the fibre was cut by using a scribe. Then the fibre tip was dipped into a drop of UV glue, lifted up, and placed perpendicularly above the LCE strip. Approaching the fibre tip towards the LCE strip was done using a vertical translation stage until the glue became in contact with the LCE center (connected with the transparent window). A UV LED (375 nm, > 200 mW cm⁻², 10 s) was used to stabilize the connection.

Elastomeric micro-cubes (PDMS) were fabricated by mixing SYLGARD(R) 184 silicone elastomer base with 10 wt% of its curing agent and solidified at 80 °C for 5 h in a cell geometry with 2-mm-gap. 2 × 2 × 2 mm cubes were cut out from the PDMS after opening the cell. Reflective layer on PDMS cubes and micro-spheres (Fig. 3) was made by deposition of 100 nm silver in a metal evaporator (Edwards Auto 306), yielding reflectivity of ~90%. Scattering and absorbing layers were obtained by placing 2 × 2 mm-sized pieces of white paper and black foil, respectively, on top of the PDMS cubes.

Characterization. Absorption spectra were measured with a UV-Vis spectrophotometer (Cary 60 UV-Vis, Agilent Technologies) equipped with a custom-made polarization controller. Optical images and movies were recorded by using a Canon 5D Mark III camera with a 100 mm lens, and thermal images were recorded

with an Infrared camera (FLIR T420BX) equipped with a close-up $2\times$ lens. Light from a continuous-wave linearly polarized laser (488 nm, Coherent Genesis CX SLM) was coupled into the fibre from one end, and output power from the LCE center at the other end was measured and reported as the excitation power for all the experiments. Light emitted from the fibre is de-polarized with polarization ratio of ~ 1.7 . No visible actuation difference in LCE has been observed by change of input laser polarization. Before each experiment, the LCE strips were alternately immersed into water and ethanol, to remove surface charge potentially generated upon removing the strips from the glass cells, or upon interacting with objects such as PDMS. The force generation upon photoactuation was measured by mounting a $5\times 1\times 0.02\text{ mm}^3$ LCE strip onto a three-dimensional translation stage, and illuminating with 488 nm laser at 45° angle of incidence, as shown in the inset of Fig. 4a. Upon illumination the sample bent over 90° and being in contact with a force sensor, the light-induced force vs. light intensity was recorded.

Data availability. The data that support the findings of this study are available from the corresponding author upon request.

References

- Wegst, U. G. K., Bai, H., Saiz, E., Tomsia, A. P. & Ritchie, R. O. Bioinspired structural materials. *Nat. Mater.* **14**, 23–36 (2014).
- Zhao, Y. *et al.* Progressive macromolecular self-assembly: from biomimetic chemistry to bio-inspired materials. *Adv. Mater.* **25**, 5215–5256 (2013).
- Morris, E., Chavez, M. & Tan, C. Dynamic biomaterials: toward engineering autonomous feedback. *Curr. Opin. Biotechnol.* **39**, 97–104 (2016).
- Cully, A., Clune, J., Tarapore, D. & Mouret, J. B. Robots that can adapt like animals. *Nature* **521**, 503–507 (2015).
- Pfeifer, R., Lungarella, M. & Iida, F. Self-organization, embodiment, and biologically inspired robotics. *Science* **318**, 1088–1093 (2007).
- Ma, K. Y., Chirarattananon, P., Fuller, S. B. & Wood, R. J. Controlled flight of a biologically inspired, insect-scale robot. *Science* **340**, 603–607 (2013).
- Qiu, T. *et al.* Swimming by reciprocal motion at low Reynolds number. *Nat. Commun.* **5**, 5119 (2014).
- Floyd, S. & Sitti, M. Design and development of the lifting and propulsion mechanism for a biologically inspired water runner robot. *IEEE Trans. Robot.* **24**, 698–709 (2008).
- Morin, S. A. *et al.* Camouflage and display for soft machines. *Science* **337**, 828–832 (2012).
- Tottori, S. *et al.* Magnetic helical micromachines: fabrication, controlled swimming, and cargo transport. *Adv. Mater.* **24**, 811–816 (2012).
- Gershman, S. J., Horvitz, E. J. & Tenenbaum, J. B. Computational rationality: a converging paradigm for intelligence in brains, minds, and machines. *Science* **349**, 273–278 (2015).
- Shepherd, R. F. *et al.* Multitask soft robot. *Proc. Natl Acad. Sci. USA* **108**, 20400–20403 (2011).
- Park, S. J. *et al.* Phototactic guidance of a tissue-engineered soft-robotic ray. *Science* **353**, 158–162 (2016).
- Rus, D. & Tolley, M. T. Design, fabrication and control of soft robots. *Nature* **521**, 467–475 (2015).
- Rogoz, M., Zeng, H., Xuan, C., Wiersma, D. S. & Wasylczyk, P. Light-driven soft robot mimics caterpillar locomotion in natural scale. *Adv. Opt. Mater.* **4**, 1689–1694 (2016).
- Wehner, M. *et al.* An integrated design and fabrication strategy for entirely soft, autonomous robots. *Nature* **536**, 451–455 (2016).
- Kumar, K. *et al.* A chaotic self-oscillating sunlight-driven polymer actuator. *Nat. Commun.* **7**, 11975 (2016).
- White, T. J. *et al.* A high frequency photodrive polymer oscillator. *Soft Matter* **4**, 1796–1798 (2008).
- Maeda, S., Hara, Y., Sakai, T., Yoshida, R. & Hashimoto, S. Self-walking gel. *Adv. Mater.* **19**, 3480–3484 (2007).
- Jenkins, A. Self-oscillation. *Phys. Rep.* **525**, 167–222 (2013).
- Forterre, Y., Skotheim, J. M., Dumais, J. & Mahadevan, L. How the Venus flytrap snaps. *Nature* **433**, 421–425 (2005).
- Dumais, J. & Forterre, Y. 'Vegetable Dynamics': the role of water in plant movements. *Annu. Rev. Fluid Mech.* **44**, 453–478 (2012).
- White, T. J. & Broer, D. J. Programmable and adaptive mechanics with liquid crystal polymer networks and elastomers. *Nat. Mater.* **14**, 1087–1098 (2015).
- Li, M. H., Keller, P., Li, B., Wang, X. & Brunet, M. Light-driven side-on nematic elastomer actuators. *Adv. Mater.* **15**, 569–572 (2003).
- Küper, J. & Finkelmann, H. Nematic liquid single crystal elastomers. *Die Makromol. Chemie, Rapid Commun.* **12**, 717–726 (1991).
- Courty, S., Mine, J., Tajbakhsh, A. R. & Terentjev, E. M. Nematic elastomers with aligned carbon nanotubes: new electromechanical actuators. *Europhys. Lett.* **64**, 654–660 (2003).
- Huang, C. *et al.* Miniaturized swimming soft robot with complex movement actuated and controlled by remote light signals. *Sci. Rep.* **5**, 17414 (2015).
- Zeng, H. *et al.* Light-fueled microscopic walkers. *Adv. Mater.* **27**, 3883–3887 (2015).
- Palagi, S. *et al.* Structured light enables biomimetic swimming and versatile locomotion of photoresponsive soft microrobots. *Nat. Mater.* **15**, 647–653 (2016).
- Yamada, M. *et al.* Photomobile polymer materials: towards light-driven plastic motors. *Angew. Chem. Int. Ed. Engl.* **47**, 4986–4988 (2008).
- Dawson, N. J., Kuzyk, M. G., Neal, J., Luchette, P. & Palfy-Muhoray, P. Experimental studies of the mechanisms of photomechanical effects in a nematic liquid crystal elastomer. *J. Opt. Soc. Am. B* **28**, 1916–1921 (2011).
- Dawson, N. J., Kuzyk, M. G., Neal, J., Luchette, P. & Palfy-Muhoray, P. Cascading of liquid crystal elastomer photomechanical optical devices. *Opt. Commun.* **284**, 991–993 (2011).
- Finkelmann, H., Kim, S. T., Munoz, A., Palfy-Muhoray, P. & Taheri, B. Tunable mirrorless lasing in cholesteric liquid crystalline elastomers. *Adv. Mater.* **13**, 1069–1072 (2001).
- Ikeda, T., Mamiya, J. I. & Yu, Y. Photomechanics of liquid-crystalline elastomers and other polymers. *Angew. Chem. Int. Ed. Engl.* **46**, 506–528 (2007).
- Mol, G. N., Harris, K. D., Bastiaansen, C. W. M. & Broer, D. J. Thermo-mechanical responses of liquid-crystal networks with a splayed molecular organization. *Adv. Funct. Mater.* **15**, 1155–1159 (2005).
- Zhao, Q. *et al.* A bioinspired reversible snapping hydrogel assembly. *Mater. Horiz.* **3**, 422–428 (2016).
- Kim, S.-W. *et al.* Flytrap-inspired robot using structurally integrated actuation based on bistability and a developable surface. *Bioinspir. Biomim.* **9**, 036004 (2014).
- Camacho-Lopez, M., Finkelmann, H., Palfy-Muhoray, P. & Shelley, M. Fast liquid-crystal elastomer swims into the dark. *Nat. Mater.* **3**, 307–310 (2004).
- van Oosten, C. L., Bastiaansen, C. W. M. & Broer, D. J. Printed artificial cilia from liquid-crystal network actuators modularly driven by light. *Nat. Mater.* **8**, 677–682 (2009).
- Liu, D., Bastiaansen, C. W. M., den Toonder, J. M. J. & Broer, D. J. Photo-switchable surface topologies in a chiral-nematic polymer. *Angew. Chem. Int. Ed. Engl.* **51**, 892–896 (2012).
- Zeng, H. *et al.* High-resolution 3D direct laser writing for liquidcrystalline elastomer microstructures. *Adv. Mater.* **26**, 2319–2322 (2014).
- Ware, T. H., McConney, M. E., Wie, J. J., Tondiglia, V. P. & White, T. J. Voxelated liquid crystal elastomers. *Science* **347**, 982–984 (2015).
- Zeng, H. *et al.* Alignment engineering in liquid crystalline elastomers: free-form microstructures with multiple functionalities. *Appl. Phys. Lett.* **106**, 111902 (2015).
- Ohm, C., Brehmer, M. & Zentel, R. Liquid crystalline elastomers as actuators and sensors. *Adv. Mater.* **22**, 3366–3387 (2010).

Acknowledgements

A.P. gratefully acknowledges the financial support of the European Research Council (Starting Grant project PHOTOTUNE; Agreement No. 679646). O.M.W. is thankful to the graduate school of Tampere University of Technology (TUT), and H.Z. to the TUT postdoctoral fellowship program, for supporting this work. We are indebted to Dr V. Manninen and Dr M. Virkki for assistance with silver deposition and spectral measurements. Dr P. Wasylczyk (Warsaw University), and Prof. Olli Ikkala (Aalto University) are acknowledged for inspiring discussions and insightful comments.

Author contributions

H.Z. and A.P. conceived the project; O.M.W. and H.Z. performed experiments. All authors contributed in writing the manuscript.

Additional information

Supplementary Information accompanies this paper at <http://www.nature.com/naturecommunications>

Competing interests: The authors declare no competing financial interests.

Reprints and permission information is available online at <http://npg.nature.com/reprintsandpermissions/>

How to cite this article: Wani, O. M. *et al.* A light-driven artificial flytrap. *Nat. Commun.* **8**, 15546 doi: 10.1038/ncomms15546 (2017).

Publisher's note: Springer Nature remains neutral with regard to jurisdictional claims in published maps and institutional affiliations.



This work is licensed under a Creative Commons Attribution 4.0 International License. The images or other third party material in this article are included in the article's Creative Commons license, unless indicated otherwise in the credit line; if the material is not included under the Creative Commons license, users will need to obtain permission from the license holder to reproduce the material. To view a copy of this license, visit <http://creativecommons.org/licenses/by/4.0/>

© The Author(s) 2017

PUBLICATION IV

An artificial nocturnal flower via humidity-gated photoactuation in liquid crystal networks

Owies M. Wani, Rob Verpaalen, Hao Zeng, Arri Priimagi and Albert P. H. J. Schenning

Advanced Materials, vol. 31, no. 2, p. 1805985, 2018. Available: [10.1002/adma.201805985](https://doi.org/10.1002/adma.201805985)

Publication reprinted with the permission of the copyright holders.

An Artificial Nocturnal Flower via Humidity-Gated Photoactuation in Liquid Crystal Networks

Owies M. Wani, Rob Verpaalen, Hao Zeng, Arri Priimagi,* and Albert P. H. J. Schenning*

Beyond their colorful appearances and versatile geometries, flowers can self-shape-morph by adapting to environmental changes. Such responses are often regulated by a delicate interplay between different stimuli such as temperature, light, and humidity, giving rise to the beauty and complexity of the plant kingdom. Nature inspires scientists to realize artificial systems that mimic their natural counterparts in function, flexibility, and adaptation. Yet, many of the artificial systems demonstrated to date fail to mimic the adaptive functions, due to the lack of multi-responsivity and sophisticated control over deformation directionality. Herein, a new class of liquid-crystal-network (LCN) photoactuators whose response is controlled by delicate interplay between light and humidity is presented. Using a novel deformation mechanism in LCNs, humidity-gated photoactuation, an artificial nocturnal flower is devised that is closed under daylight conditions when the humidity level is low and/or the light level is high, while it opens in the dark when the humidity level is high. The humidity-gated photoactuators can be fueled with lower light intensities than conventional photothermal LCN actuators. This, combined with facile control over the speed, geometry, and directionality of movements, renders the “nocturnal actuator” promising for smart and adaptive bioinspired microrobotics.

The past decades have shown that technological advances often go hand in hand with the development of new materials. For seeking inspiration, material scientists and engineers put great effort into learning from nature's sophisticated design principles.^[1–4] For example, stimuli-responsive “smart” materials that reversibly change their shape in response to external triggers, pave way for soft robotics^[5–7] and self-regulating devices,^[8–10] and bioinspired hierarchical surfaces are pertinent in application in wettability control and adhesion.^[11–13]

flower opening/closing is correlated with the time of day and temperature, and light and humidity play an important role in regulating the process. Flowers which bloom in the morning are mainly regulated by temperature and/or light, while in nocturnal flowers, relative humidity (RH) plays an additional role, and their opening correlates with both decrease in light intensity and increase in the RH.^[22] Being based on an interplay between different stimuli, the opening and closing of flowers highlights the versatile and adaptive behavior of plant species and more generally, the complexity of plant kingdom. This depicts that for realization of manmade devices capable of mimicking the complex functionalities of natural species, the use of multi-responsive materials is one of the key design principles.

Despite the significant research effort dedicated to stimuli-responsive materials and structures,^[14,15] multi-responsive materials that can be triggered by light, temperature, and humidity (or an interplay between them) have been rarely studied. Agarose-based hybrid materials containing acidochromic fluorophores or azobenzene derivatives have been demonstrated to undergo humidity- and light-induced deformations.^[23,24] Carbon-nitride-based polymers that are sensitive to small fluctuations in humidity and that can quickly lose the absorbed water through heating or UV light irradiation, have also been fabricated.^[25] Finally, bilayer materials containing carbon nanotubes or reduced graphene

O. M. Wani, Dr. H. Zeng, Prof. A. Priimagi
Laboratory of Chemistry and Bioengineering
Tampere University of Technology
P.O. Box 541, FI-33101 Tampere, Finland
E-mail: arri.priimagi@tut.fi

R. Verpaalen, Prof. A. P. H. J. Schenning
Laboratory of Stimuli-Responsive Functional Materials and Devices
Department of Chemical Engineering and Chemistry
Eindhoven University of Technology
P.O. Box 513, 5600 MB Eindhoven, The Netherlands
E-mail: a.p.h.j.schenning@tue.nl

 The ORCID identification number(s) for the author(s) of this article can be found under <https://doi.org/10.1002/adma.201805985>.

DOI: 10.1002/adma.201805985

oxide can also exhibit light- and humidity-induced bending movements by controlling water absorption/desorption via photothermal effect.^[26,27] However, these materials are either based on laminated bilayers, which restricts their practical utility, or they lack sophisticated control over the directionality of the movements, which is an important factor for developing biomimetic actuators. By using liquid crystal networks (LCNs), both of these deficiencies can be addressed. LCNs combine the anisotropic properties of liquid crystals with the mechanical rigidity of polymer networks, thereby providing stimuli-responsive anisotropic deformation of the network with movement direction governed by the alignment of the constituent LC molecules.^[28,29] As the molecular alignment can be controlled and even patterned during the fabrication process, LCN actuators can have many degrees of freedom in their deformation.^[30,31] The programmable, reversible shape changes render LCNs attractive from the perspective of soft actuators/robotics.^[32] By proper materials design, actuation in LCNs can be triggered by humidity changes, resulting in efficient bending with well-controlled directionality, in a monolithic structure.^[33–35] Up to date, the only example of LCN actuator driven by both light and humidity is given by Liu et al.,^[36] where they have demonstrated a dual-mode bending of LCN film either toward light source along the director axis, or away from humidity source perpendicular to the director axis. However, the multi-responsive LCN presented in ref. [36] was only actuated by either light or humidity, i.e., the two stimuli were orthogonal and not interconnected. Furthermore, the molecular alignment of that LCN was uniform throughout the sample, hence it responded to humidity gradient rather than to change in ambient humidity per se. For the creation of logical gates from multi-responsive actuators and evermore sophisticated bioinspired structures, it is pertinent to first understand the intricate interplay that may exist between the different stimuli, and then co-use them to introduce functionalities not met by the different stimuli alone. To the best of our knowledge, such interplay between light and humidity in LCN actuators has not been previously studied.

In the present work, we take inspiration from the nocturnal flower and devise a monolithic LCN actuator whose movements are controlled by a delicate interdependence between light and humidity, a process that we coin as humidity-gated photoactuation. Alike its natural counterpart, the nocturnal actuator opens under dark and humid conditions, and closes when the humidity decreases and light level increases (Figure 1a). Such unconventional actuation is based on selective absorption of water on one surface of the “flower petal,” which closes upon photothermally-induced water desorption and resultant deswelling of the petals. We show that the deformation mechanism underlying the humidity-gated photoactuation, which has not been studied in LCN actuators before, greatly increases the sensitivity of the deformation, allowing the use of low light levels to trigger fast and efficient photoactuation.

To combine the humidity sensitivity and light response into one LCN actuator, we incorporated a “photothermal moiety,” an azobenzene derivative Disperse Red 1 acrylate, into an LC mixture consisting of hydrogen-bonded, acrylate-based carboxylic acid monomers of varying chain lengths.^[37] The composition of the mixture is given in Figure 1b (see the “Materials and characterization” section in the Supporting Information). Polymerization (365 nm, 20 mW cm⁻², 5 min) was performed

in a 20 μ m LC cell at a temperature of 80 °C. The relatively high polymerization temperature was used in order to obtain high initial curvature for the LCN actuator at ambient conditions, and to avoid the formation of cybotactic clusters at lower temperatures (Figure S1, Supporting Information).^[38] The high initial curvature results from anisotropic thermal expansion of the film polymerized above room temperature: the more the difference between the polymerization temperature and room temperature, the larger the curvature (defined as the inverse radius).^[10,39] In terms of alignment, splayed molecular orientation was chosen because splay-aligned LCN actuators bend smoothly and to high degrees,^[40] and their bending axis can be manipulated by changing the angle between the long axis of the strip and the director on the planar side.^[31] The combination of suitable polymerization temperature and splay alignment render LCN strips capable of mimicking the geometry of a flower, together with the curvature change during flower blooming. After polymerization, the sample was soaked in a basic solution (0.1 M aq. solution of KOH) to make it humidity sensitive. The base treatment breaks the hydrogen bonds between the carboxylic acid dimers and converts them into hygroscopic carboxylic salt.^[34] The treatment was selectively executed on the homeotropic side of the sample, to form a hygroscopic surface (Figure 1c). This was confirmed by ATR–FTIR spectra that showed the loss of hydrogen bonding peak and appearance of a peak corresponding to carboxylates on the homeotropic side of the sample, while no spectral change was observed on the planar surface (Figure S2, Supporting Information). In addition to making the material hygroscopic, the base treatment also causes further shrinkage of the LCN,^[34] thereby leading to increase in the curvature of the strip. The treated LCN strip is now sensitive to both light and humidity and its initial shape depends on the RH and the angle between the director on planar side and the long axis of the strip.

Comparison of the photomechanical properties of the LCN actuator before and after the base treatment is shown in Figure 2. As expected, the untreated sample is indifferent to humidity change, but responds to light. Upon exposure to 450 nm (100 mW cm⁻²), the strip opens (curvature decreases) due to photothermal expansion of the homeotropic surface caused by decrease in order in the LCN network (Figure 2a). After the base treatment, the curvature of the strip increases with humidity, due to absorption of water toward the homeotropic side of the strip. This humidity-induced shape-change is fully reversible upon variation in the RH. Under simultaneous stimuli of humidity and light irradiation, such dual-responsive LCN behaves in an interesting manner. At low RH, the base-treated strip slightly opens up and the curvature decreases, due to light-induced expansion of the homeotropic surface (Figure 2b). This is the normal photoactuation mechanism in splay-aligned LCNs.^[30] We note here that we observe a decrease in molecular order in the splay films after the base treatment, as evident from the polarized UV–vis absorption spectra shown in Figure S3 in the Supporting Information. This explains the fact that the photoactuation is less efficient in the base-treated films as compared to non-treated films when the humidity is low. At high RH, the light response of the base-treated film becomes totally opposite. As illustrated in Figure 2b, the curvature of the strip increases (the strip closes), even upon low-intensity

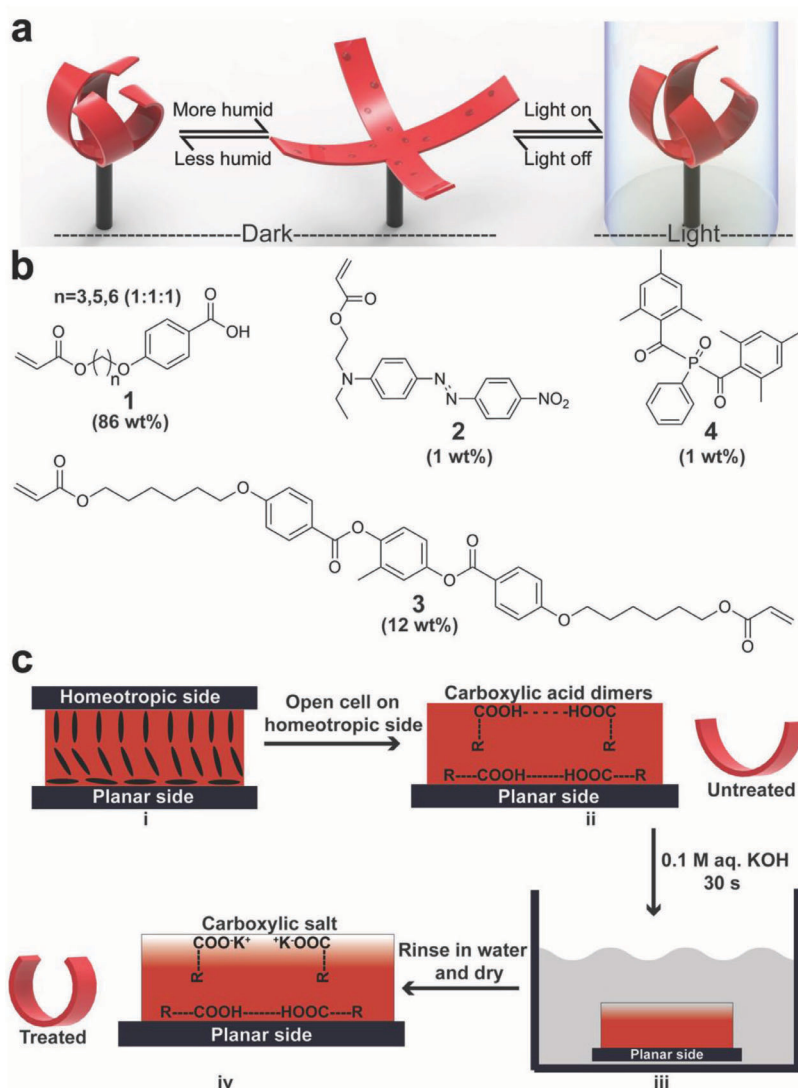


Figure 1. Realization of artificial nocturnal flower. a) Schematic representation of the nocturnal actuator: the flower opens at high humidity level in absence of light and closes in the presence of light or when the humidity is low. b) Composition of the LC mixture used in fabrication of the nocturnal actuator. c) The fabrication process: i) the mixture is polymerized in splay molecular alignment inside an LC cell, ii,iii) the cell is opened from the homeotropic side and dipped in 0.1 M KOH solution for 30 s, to perform base treatment selectively on the homeotropic side, and iv) the sample is rinsed with water and then dried in air. The insets in (c-ii) and (c-iv) show the schematic representation of the LCN strips, cut along the director on the planar side, at corresponding stage of fabrication under ambient conditions.

irradiation (450 nm , 30 mW cm^{-2}). In other words, given proper humidity level, the light-induced bending in the splay-aligned LCN takes place toward the homeotropic side of the film. Such unconventional photoactuation, gated by humidity, forms the basis for mimicking the behavior of nocturnal flower. As we will show, the mechanism behind the humidity-gated photoactuation is completely different than in conventional photoactuators.

We next studied the effect of RH on the curvature of the multi-responsive LCN strip and its shape-change upon light exposure in more detail. The curvature of the strip decreased linearly with increasing RH (Figure 3a).^[34] When the strip is exposed to light under 80% RH, the curvature increases with increasing light intensity and saturates at $50\text{--}60\text{ mW cm}^{-2}$ (Figure 3b,c). We attribute the efficient photoactuation in

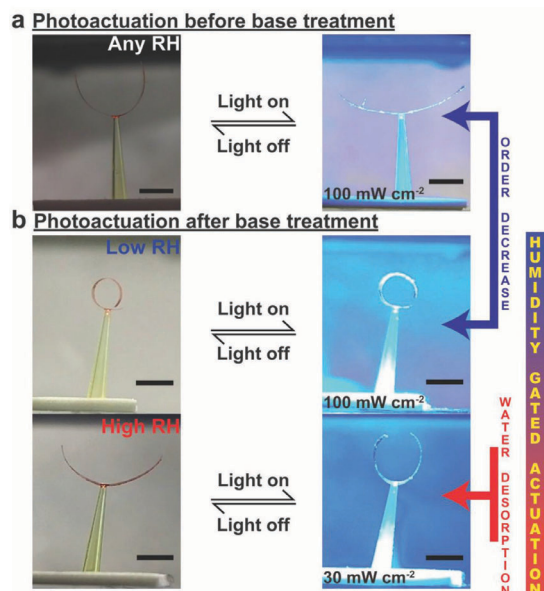


Figure 2. Humidity-gated photoactuation. a) Before base treatment, the LCN strip is insensitive to humidity and photoactuation results in expansion of homeotropic surface owing to decrease in molecular order. b) After base treatment, photoactuation is gated by humidity. At low RH, the curvature decreases due to similar mechanism as mentioned in (a). However, at high RH, the curvature increases owing to entirely different mechanism, i.e., light induced water desorption. All scale bars correspond to 5 mm. Strip dimension: 20 mm × 3 mm × 20 μ m. Light source: 450 nm.

base-treated films to water desorption from the hygroscopic (homeotropic) surface, which results in selective shrinkage and bending toward the homeotropic surface. Such process is highly light-sensitive, much more so than conventional photothermal actuation (Figure 2b,c). Thus, the coupling between light and humidity leads to a thermodynamically favored actuation mode driven by photothermally-induced water loss. The rate of water desorption is affected by the light intensity. Therefore, the irradiation power dictates the speed of actuation. This is demonstrated in Figure S4 in the Supporting Information, which reveals an enhanced actuation speed upon increasing intensity: the response time drops from 9 to 1.8 s when changing the intensity from 60 to 160 mW cm^{-2} . The higher sensitivity of the base-treated samples to low-intensity irradiation may also be somewhat affected by decrease in storage modulus of material after base treatment (Figure S5, Supporting Information).

To confirm the mechanism of light-induced closing of the humidity-sensitive LCN strip, we used infrared spectroscopy to probe the loss of water inside the sample. The sample was kept under high humidity inside the spectrometer and the NIR absorption spectra were recorded at different temperatures (Figure S6, Supporting Information). The intensity of water absorption peak at around 1900 nm was used to probe the water content, alike in previous studies.^[41,42] The water content absorbed by the LCN decreased with increasing temperature within initial 10 $^{\circ}\text{C}$ temperature change (from 20 to

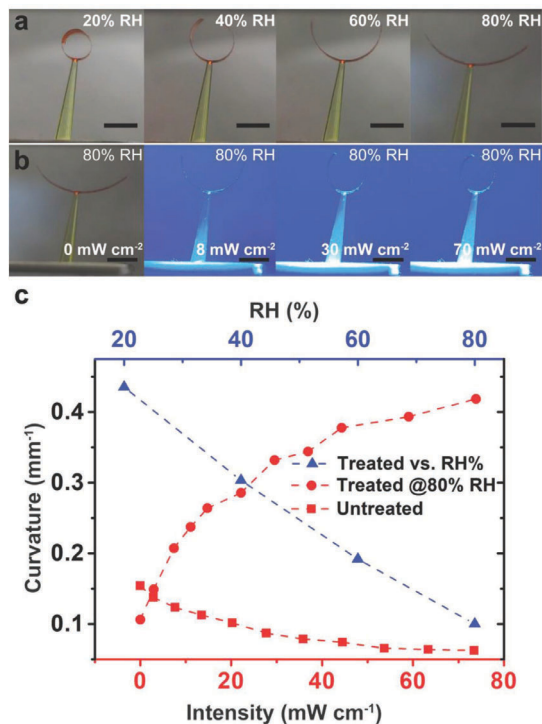


Figure 3. Curvature changes with variation in RH and light intensity. a) Change in curvature of treated LCN strip with increasing RH, under dark conditions. b) Effect of light intensity on curvature of LCN strip held at 80% RH (room temperature). c) Curvature changes of LCN strips in response to increasing RH in the dark (blue triangles), and the photo-induced curvature change of treated (red circles), and untreated (red squares) LCN strips held at 80% RH in response to increasing light intensity. All scale bars correspond to 5 mm.

30 $^{\circ}\text{C}$), after which the water content saturated. Photothermal temperature rise in LCN strip, as measured by IR thermal camera, together with the curvature change upon increasing light intensity, is plotted in Figure 4a. Water loss upon increase in temperature, as estimated by NIR absorption, is plotted in Figure 4b. In addition to the fact that most of the water is evaporated within 10 $^{\circ}\text{C}$ temperature increase, the data shows that major change in curvature occurs with light intensity below 50–60 mW cm^{-2} . Infrared camera measurements reveal that 50–60 mW cm^{-2} irradiation causes the temperature of LCN strip to rise by 7–10 $^{\circ}\text{C}$, which, based on probing the water loss, is enough for efficient reduction of water content and thereby, saturation of the photo-induced change in curvature.

To use the interplay between light-sensitivity and humidity-sensitivity, and to demonstrate the nocturnal flower, we fabricated a monolithic piece of LCN having predesigned molecular alignment. The artificial flower consists of four petals, each bending toward the same central point. The alignment control was done using a substrate coated with polyimide alignment layer rubbed in two directions, using a steel-foil mask, to obtain the molecular orientation depicted in Figure 4c. Alike

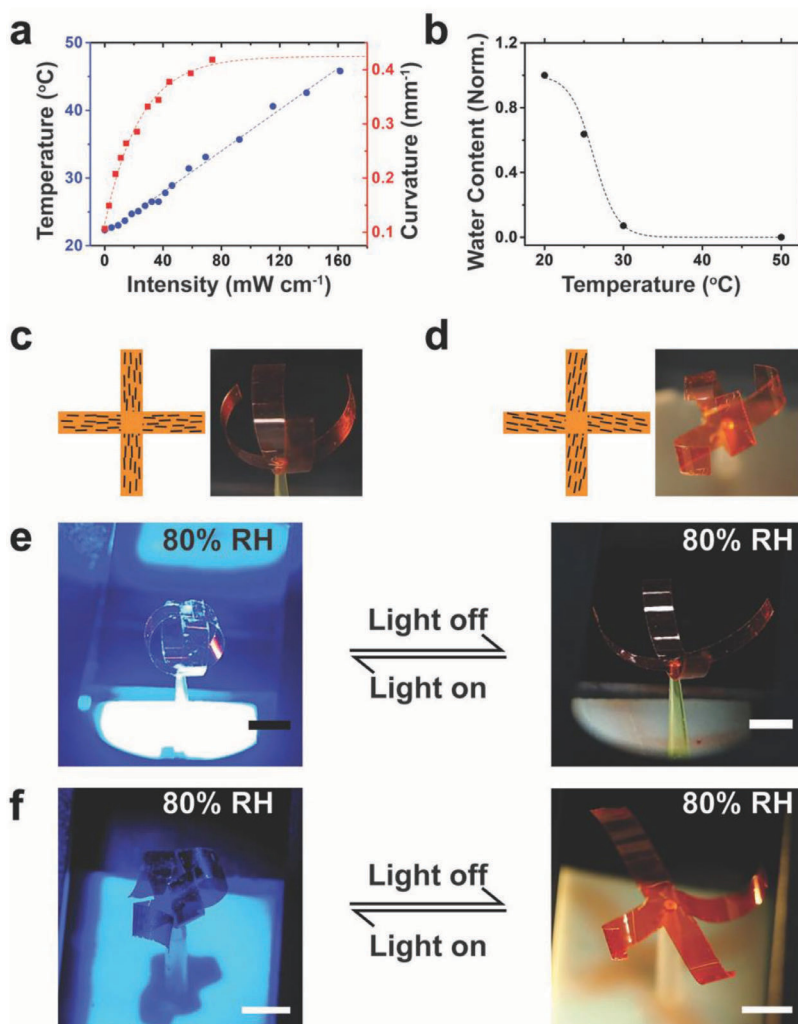


Figure 4. Demonstration of artificial nocturnal flower. a) Change in temperature and curvature of LCN strip upon illumination with increased light intensity. b) Plot of water loss upon increased temperature, as estimated from infrared spectroscopy. c,d) Representation of molecular alignment in four petals of monolithic LCN flowers and their corresponding initial shape under ambient conditions. In (c), the director on the planar side is parallel to the long axis of the petal, while in (d), the director has an offset of 10° with respect to the long axis. e,f) Closure of LCN flower, in straight (e) and twisted (f) ways, respectively, upon illumination with light, as dictated by their molecular alignment. All scale bars correspond to 5 mm.

the night flowers, the nocturnal actuator remains closed at low RH or upon high light level, and only opens at high RH in the darkness (Figure 4e; Video S1, Supporting Information). To demonstrate the versatility of LCN materials compared to other stimuli-responsive materials in terms of controlling the directionality of deformation, a task very difficult to achieve in conventional hygroscopic materials,^[43] we made another nocturnal actuator having an offset angle of 10° between director and the long axis of the flower petal (Figure 4d). Like some nocturnal flowers such as moon plant,^[44] this artificial “flower” opens and closes in a twisted manner (Figure 4f;

Video S2, Supporting Information). By varying the offset angle, the pitch of the twisting can be easily controlled, highlighting the strength of LCN actuators in devising biomimetic structures. Due to this advantage of LCN materials, even complex plant movements can be mimicked, providing a route for advanced and adaptive shape morphing.

In conclusion, we have demonstrated an artificial “nocturnal actuator” made of a monolithic multi-responsive liquid crystal network, which can mimic the opening and closing of night flowers. Similar to their natural counterparts, the movements of this LCN actuator are dictated by delicate interplay between

light and RH. The demonstrated flower-like device closes when it is exposed to light or when the humidity level is low. It opens only in the dark, assisted by high humidity level in the environment. The method that drives the shape morphing, humidity-gated photoactuation, is based on photothermally-induced water desorption from the LCN films. We foresee that the proposed bioinspired humidity- and light-responsive actuator, due to its fast response time and control over directionality, is promising for the realization of smart biomimetic systems and soft robots that can be manipulated remotely by low levels of light.

Supporting Information

Supporting Information is available from the Wiley Online Library or from the author.

Acknowledgements

A.P. gratefully acknowledges the financial support of the European Research Council (Starting Grant project PHOTOTUNE; Agreement No. 679646). O.W. thanks the Graduate School of Tampere University of Technology (TUT), as well as the International HR Services of TUT for funding a 6-month research internship to Technical University of Eindhoven, under the scheme "TUT on World Tour-2018." H.Z. thanks the Academy of Finland for a Postdoctoral Fellowship (decision number 316416). The authors thank Prof. Dirk Broer for inspiring discussions.

Conflict of Interest

The authors declare no conflict of interest.

Keywords

actuator, azobenzene, bioinspired, humidity, light, liquid crystal, multi-responsive

Received: September 14, 2018

Revised: October 17, 2018

Published online: November 12, 2018

- [1] U. G. K. Wegst, H. Bai, E. Saiz, A. P. Tomsia, R. O. Ritchie, *Nat. Mater.* **2015**, 14, 23.
- [2] F. Xia, L. Jiang, *Adv. Mater.* **2008**, 20, 2842.
- [3] M. Liu, Y. Zheng, J. Zhai, L. Jiang, *Acc. Chem. Res.* **2010**, 43, 368.
- [4] Y. Zhao, F. Sakai, L. Su, Y. Liu, K. Wei, G. Chen, M. Jiang, *Adv. Mater.* **2013**, 25, 5215.
- [5] S. Kim, C. Laschi, B. Trimmer, *Trends Biotechnol.* **2013**, 31, 287.
- [6] S. I. Rich, R. J. Wood, C. Majidi, *Nat. Electron.* **2018**, 1, 102.
- [7] L. Hines, K. Petersen, G. Z. Lum, M. Sitti, *Adv. Mater.* **2017**, 29, 1603483.
- [8] S. Maeda, Y. Hara, T. Sakai, R. Yoshida, S. Hashimoto, *Adv. Mater.* **2007**, 19, 3480.
- [9] X. He, M. Aizenberg, O. Kuksenok, L. D. Zarzar, A. Shastri, A. C. Balazs, J. Aizenberg, *Nature* **2012**, 487, 214.
- [10] H. Zeng, O. M. Wani, P. Wasylczyk, R. Kaczmarek, A. Priimagi, *Adv. Mater.* **2017**, 29, 1701814.
- [11] K. Liu, X. Yao, L. Jiang, *Chem. Soc. Rev.* **2010**, 39, 3240.
- [12] L. F. Boesel, C. Greiner, E. Arzt, A. del Campo, *Adv. Mater.* **2010**, 22, 2125.
- [13] T.-S. Wong, S. H. Kang, S. K. Y. Tang, E. J. Smythe, B. D. Hatton, A. Grinthal, J. Aizenberg, *Nature* **2011**, 477, 443.
- [14] D. Roy, J. N. Cambre, B. S. Sumerlin, *Prog. Polym. Sci.* **2010**, 35, 278.
- [15] M. A. C. Stuart, W. T. S. Huck, J. Genzer, M. Müller, C. Ober, M. Stamm, G. B. Sukhorukov, I. Szleifer, V. V. Tsukruk, M. Urban, F. Winnik, S. Zauscher, I. Luzinov, S. Minko, *Nat. Mater.* **2010**, 9, 101.
- [16] I. Burgert, P. Fratzl, *Philos. Trans. R. Soc., A* **2009**, 367, 1541.
- [17] B. Mazzolai, L. Beccai, V. Mattoli, *Front. Bioeng. Biotechnol.* **2014**, 2, 2.
- [18] S. Iamsaard, S. J. Aßhoff, B. Matt, T. Kudernac, J. J. L. M. Cornelissen, S. P. Fletcher, N. Katsonis, *Nat. Chem.* **2014**, 6, 229.
- [19] O. M. Wani, H. Zeng, A. Priimagi, *Nat. Commun.* **2017**, 8, 15546.
- [20] Y. Forterre, J. M. Skotheim, J. Dumais, L. Mahadevan, *Nature* **2005**, 433, 421.
- [21] B. S. Hill, G. P. Findlay, *Q. Rev. Biophys.* **1981**, 14, 173.
- [22] W. G. Van Doorn, U. Van Meeteren, *J. Exp. Bot.* **2003**, 54, 1801.
- [23] L. Zhang, H. Liang, J. Jacob, P. Naumov, *Nat. Commun.* **2015**, 6, 7429.
- [24] L. Zhang, P. Naumov, *Angew. Chem., Int. Ed.* **2015**, 54, 8642.
- [25] H. Arazoe, D. Miyajima, K. Akaike, F. Araoka, E. Sato, T. Hikima, M. Kawamoto, T. Aida, *Nat. Mater.* **2016**, 15, 1084.
- [26] a) M. Ji, N. Jiang, J. Chang, J. Sun, *Adv. Funct. Mater.* **2014**, 24, 5412. b) J. Mu, C. Hou, B. Zhu, H. Wang, Y. Li, Q. Zhang, *Sci. Rep.* **2015**, 5, 9503.
- [27] P. Zhou, L. Chen, L. Yao, M. Weng, W. Zhang, *Nanoscale* **2018**, 10, 8422.
- [28] T. J. White, D. J. Broer, *Nat. Mater.* **2015**, 14, 1087.
- [29] C. Ohm, M. Brehmer, R. Zentel, *Adv. Mater.* **2010**, 22, 3366.
- [30] L. T. De Haan, A. P. H. J. Schenning, D. J. Broer, *Polymer* **2014**, 55, 5885.
- [31] O. M. Wani, H. Zeng, P. Wasylczyk, A. Priimagi, *Adv. Opt. Mater.* **2018**, 6, 1700949.
- [32] H. Zeng, P. Wasylczyk, D. S. Wiersma, A. Priimagi, *Adv. Mater.* **2018**, 30, 1703554.
- [33] K. D. Harris, C. W. M. Bastiaansen, J. Lub, D. J. Broer, *Nano Lett.* **2005**, 5, 1857.
- [34] L. T. De Haan, J. M. N. N. Verjans, D. J. Broer, C. W. M. M. Bastiaansen, A. P. H. J. H. J. Schenning, *J. Am. Chem. Soc.* **2014**, 136, 10585.
- [35] A. Ryabchun, F. Lancia, A.-D. D. Ngundjel, N. Katsonis, *Soft Matter* **2017**, 13, 8070.
- [36] Y. Liu, B. Xu, S. Sun, J. Wei, L. Wu, Y. Yu, *Adv. Mater.* **2017**, 29, 1604792.
- [37] K. D. Harris, C. W. M. Bastiaansen, D. J. Broer, *J. Microelectromech. Syst.* **2007**, 16, 480.
- [38] W. Nishiya, Y. Takanishi, J. Yamamoto, A. Yoshizawa, *J. Mater. Chem. C* **2014**, 2, 3677.
- [39] D. J. Broer, G. N. Mol, *Polym. Eng. Sci.* **1991**, 31, 625.
- [40] G. N. Mol, K. D. Harris, C. W. M. Bastiaansen, D. J. Broer, *Adv. Funct. Mater.* **2005**, 15, 1155.
- [41] *Near-Infrared Spectroscopy: Principles, Instruments, Applications*, (Eds: H. W. Siesler, Y. Ozaki, S. Kawata, H. M. Heise), Wiley-VCH, Weinheim, Germany **2002**.
- [42] F. Ridi, E. Fratini, S. Milani, P. Baglioni, *J. Phys. Chem. B* **2006**, 110, 16326.
- [43] L. Ionov, *Mater. Today* **2014**, 17, 494.
- [44] C. R. Gunn, *Brittonia* **1972**, 24, 150.

